8-30-2011

Strengthening reinforced concrete slabs using a combination of CFRP and UHPC

Andrew P. Garner

Recommended Citation

Garner, Andrew P.. "Strengthening reinforced concrete slabs using a combination of CFRP and UHPC." (2011). https://digitalrepository.unm.edu/ce_etds/54

Andrew P. Garner

Candidate

Civil Engineering

Department

This thesis is approved, and it is acceptable in quality
and form for publication:

Approved by the Thesis Committee:

Mahmoud Reda Taha , Chairperson

Arup Maji

Walter Gerstle

STRENGTHENING REINFORCED CONCRETE SLABS USING A COMBINATION OF CFRP AND UHPC

BY

ANDREW P. GARNER

B.S. CIVIL ENGINEERING, UNIVERSITY OF NEW MEXICO 2009

THESIS

Submitted in Partial Fulfillment of the
Requirements for the Degree of

Master of Science

Civil Engineering

The University of New Mexico
Albuquerque, New Mexico

June, 2011

DEDICATION

To my wonderful wife, Ashli, who has shown incredible love and support. I would also like to dedicate this work to my parents, who have provided me with everything that I’ve needed to succeed.

ACKNOWLEDGMENTS

I would like to extend the utmost gratitude to my Master's advisor and committee chair, Dr. Mahmoud Reda Taha. Without your motivation and support, this work would not have been possible. Your guidance, encouragement, and advice have had a deep impact on me, and I will carry what you have taught me for the rest of my life. It has truly been an honor to work with you. I would also like to thank my committee members, Dr. Walter Gerstle and Dr. Arup Maji, for their guidance throughout my entire education pursuit at the University of New Mexico.

I would further like to thank Dr. Ayman Mosallam from the University of California, Irvine for his early contributions to this strengthening system in continuous reinforced concrete slabs. Thank you for your guidance and advice.

In addition, I would like to extend a special thank you to my colleague, Eslam Soliman, for his direction and council throughout this project. I appreciate everything you've helped me with. I would also like to thank Jacob Hays and Rick Grahn for their assistance with the concrete batching and testing required for this project as well as Mohammad Jalalpour for his valuable insight and assistance. I would like to recognize Dr. Jung Kim for his practical advice for the strengthened slab and Stephen Neidigk for his instruction and assistance in strain gage installation. To everybody else in my group, thank you.

I would also like to acknowledge the Defense Threat Reduction Agency for funding my assistantship and research.

STRENGTHENING REINFORCED CONCRETE SLABS USING A COMBINATION OF CFRP AND UHPC

BY

ANDREW P. GARNER

B.S. CIVIL ENGINEERING, UNIVERSITY OF NEW MEXICO 2009

ABSTRACT OF THESIS

Submitted in Partial Fulfillment of the
Requirements for the Degree of

Master of Science

Civil Engineering

The University of New Mexico
Albuquerque, New Mexico

June, 2011

STRENGTHENING REINFORCED CONCRETE SLABS USING A COMBINATION OF CFRP AND UHPC

by

Andrew P. Garner

B.S. Civil Engineering, University of New Mexico, 2009

ABSTRACT

Reinforced concrete (RC) structures are widely used in construction. Due to aging infrastructure, increased loads, and inadequate maintenance, RC structures need to be retrofitted for prolonged lifespan and increased capacity. Traditional methods of strengthening involve the installation of fiber reinforced polymer (FRP) composites to the tension side of structures. This can be problematic in practice because of the difficulty in accessing the underside, the tension side, of the structural member. In addition, traditional strengthening techniques typically result in exposing the FRP to the external environment with possible degradation and other environmental effects.

This research investigates an innovative method to strengthen concrete structures using a combination of ultra high performance concrete (UHPC) and FRP. Using this combination, FRP can be applied to the top side, compression side, of the slab. The hypothesis is that the implementation of the UHPC overlay will push the neutral axis up to the UHPC overlay, allowing the FRP to act as a tension element at ultimate conditions.

Two full scale RC slabs were cast and tested to failure; the first as a control and the second using this new strengthening technique. On the strengthened slab, the FRP was installed on top of the slab, which is the compression side. A thin UHPC overlay was cast above the FRP, forming an effective composite where the UHPC resisted all of the compressive stresses and the FRP and reinforcing steel resisted the tensile stresses. The proposed strengthening system increased the ultimate load carrying capacity of the slab by 41%, the stiffness by 197%, and toughness by 167%. The relative ductility of the strengthened slab was 3.3 times greater than the control slab at service loading and 2.1 times greater than the control slab at failure.

In addition, finite element models of the control and strengthened slabs were developed. The finite element models are able to accurately simulate the behavior of both slabs. A parametric study on the effect of overlay strength was also performed. It is concluded that UHPC is the compressive material of choice for this technique.

The enhanced mechanical and durability characteristics of UHPC and FRP as well as the relative ease of installation makes this proposed alternative method attractive for strengthening RC structures.

Contents

LIST OF TABLES

LIST OF FIGURES

CHAPTER 1 INTRODUCTION

Every year, more concrete is used in construction than any other material. In 2010, concrete produced in United States has been estimated to be worth $35 billion [1]. The widespread use of concrete can be attributed to its attractive properties and accessibility. Because of its poor tensile strength, it is often paired with reinforcing steel, which is cast away from the neutral axis, to form an effective composite. This composite, reinforced concrete (RC), is designed such that the compression forces are resisted by the concrete while the tension forces are resisted by the steel. This configuration of reinforcement provides acceptable flexural strength.

RC is used in structures of all types, ranging from columns, beams, and slabs to storm drain pipe, floor systems, and foundations. Because of deterioration of the concrete due to aging, corrosion of the reinforcing steel, and increased loads that were previously unaccounted for, structural members may require strengthening after being constructed [2-5]. The issue of strengthening existing RC structures has become an important topic in structural engineering.

If strengthening existing infrastructure is feasible, it is much preferred over the demolition and construction of an entirely new system. This is due to the relatively low cost of strengthening compared to new construction in addition to the minimal impact that strengthening will have on the system. Two other major benefits include the short time of application and ability to maintain use of the structure during strengthening [4, 6].

1.1 TRADITIONAL METHOD FOR STRENGTHENING BEAMS

In order to increase the capacity of an existing RC beam, the amount of tensile capacity or compressive capacity must be increased. A relatively new method that has become accepted for strengthening existing structures is through the use of fiber reinforced polymer (FRP) composites. The high strength-to-weight ratio, resistance to corrosion, ease of application, the ability to install FRP without disrupting use of the structure, and relatively low maintenance of FRP make it an attractive composite to be used for strengthening.

Current methods of application recommend that the FRP be installed at the location of the extreme tensile fiber at the location of the maximum tension [2]. This application allows the normal concrete to act in compression while the reinforcing steel and FRP act in tension. The FRP is subjected to tensile forces during the entire loading. As the loading progresses, the neutral axis will move toward the compression side of the member and the member will fail, typically due to debonding of the strengthening system prior to crushing of the concrete.

1.2 PROPOSED METHOD FOR STRENGTHENING

This thesis addresses a new method for strengthening existing RC structures, specifically slabs. In addition to using FRP for RC strengthening, ultra high performance concrete (UHPC) is utilized. UHPC is a dense concrete with characteristic compressive strengths that range from 18,000 to 33,000 psi [7]. Instead of applying FRP to the extreme tensile fiber, the FRP is applied to the extreme compressive fiber of the structural member at location of the maximum compression. Afterwards, a thin layer of UHPC overlay is cast above the FRP creating, in effect, a second beam.

Initially, as the bending element is loaded, the tension forces will be resisted by the reinforcing steel and the concrete will act with the UHPC in compression. With further loading, and as the neutral axis approaches the top of the beam, the FRP will begin to act in tension and the UHPC will absorb all of the compressive stresses exerted on the member. A significant increase in bending strength will then be apparent in the member. In addition to the increase in strength, this system will address accessibility issues and exposure problems present in traditional strengthening techniques.

Three main contributors are responsible for the increased capacity of the strengthened RC system. These include the depth of the beam, the very high compressive strength of the UHPC, and the significant tensile capacity of the FRP. This configuration also eliminates peeling of the FRP from the underside of the slab, which can prove to be a challenge.

To validate this novel strengthening technique, two one-way slabs were cast. The first slab was an unstrengthened concrete slab which was used as a control. The second slab was cast to mimic the first but featured an overlay of FRP and UHPC. Both slabs were treated as simple beams with a region that contained a constant bending moment and theoretically no shear. This setup was imperative to provide accurate results that pertain to bending. Strain gauges were used at strategic locations at the mid span of the beams. In addition, linear variable differential transducers (LVDTs) were used to acquire displacement data at the mid span and the ends of the slabs. LVDTs are important for measuring displacement of the system without compliance effects.. A load cell was also used to constantly monitor and record the applied force used throughout the experiments on the two slabs.

A finite element (FE) model was also developed. The model for the control slab consisted of concrete and reinforcing steel and was calibrated using experimental data acquired from testing the control slab. A second FE model for the strengthened slab was also developed using the same material properties and parameters used in first model. In addition, FRP and UHPC were included in the second FE model. The FE model of the strengthened slab was then used to conduct a parametric study of the proposed strengthening system.

The hypothesis for this method of strengthening is that the FRP will act as typical reinforcement as the RC slab approaches the ultimate limit state. Perfect bond between the UHPC, FRP, and NVC substrate is assumed to hold. If debonding does occur, alternative bonding techniques and agents might be suggested.

1.3 OUTLINE OF THE THESIS

The thesis begins with background information and a literature review on FRP and UHPC. It also provides information about strengthening methods and the mechanics that allow RC strengthening to take place.

Chapter 3 provides information on the experimental methods and describes the test setup and the standards that were followed in performing the tests. This chapter also details the techniques used in mixing and curing of the concretes and the mechanics that the new technique is based on. This section includes information on both the control slab and the strengthened slab. Rationalization of the location of the strain gauges and (LVDTs) is also discussed.

Chapter 4 provides details on the FE procedures and the numerical methods used. Information about element types, model specifics, and analysis parameters are discussed.

The outcomes from both the experimental and numerical analyses are included in Chapter 5. This chapter details the data obtained for the strain gauges, LVDTs, load, and displacement for the control slab and the strengthened slab. A simple validation of the mechanics is presented. Moreover, the results from the numerical analysis are also presented. A confirmation that the FE modeling is applicable for predicting this new strengthening procedure is provided.

Finally, conclusions are drawn in Chapter 6. These conclusions are based on the experimental and numerical analyses. Recommendations about future work in this area are also presented.

CHAPTER 2 LITERATURE REVIEW

2.1 INTRODUCTION

This chapter provides a literature review detailing ultra high performance concrete (UHPC), fiber reinforced polymer (FRP), unstrengthened slab design, and current practices of FRP strengthening of reinforced concrete (RC) structures. This chapter begins by providing an overview of RC and the mechanics of normal RC design. It continues with the development of UHPC in addition to its general composition and typical properties. The attributes of FRP are then presented along with the relatively brief history of FRP and its various applications. The mechanics of RC strengthening is covered in detail. Finally, different practices for strengthening existing concrete structures are described.

2.2 ULTRA HIGH PERFORMANCE CONCRETE (UHPC)

Ultra high performance concrete (UHPC) is a relatively new material, being first produced and tested in the early 1980s [8]. For concrete to qualify as UHPC, it must possess a characteristic compressive strength between 18000 and 33000 psi (125 and 225 MPa) [7]. UHPC also features attractive tensile behavior and has greater durability than typical concrete [8]. UHPC also features low creep and shrinkage [9, 10].

UHPC has a very dense microstructure and a very low porosity which both contribute to its attractive physical properties. This dense microstructure is achieved through the use of small-grained and well-graded materials [11]. The transition zone in UHPC is much smaller than traditional concrete and high performance concrete [12]. Silica fume is an essential constituent in UHPC and serves two purposes in production: it is used as a filler and as a pozzolan [13]. As a pozzolan, silica fume increases concrete strength and as a filler, silica fume contributes to the high packing density of the concrete [12-15]. This dense packing of the UHPC microstructure reduces lateral tensile stresses which increases the concrete strength [15]. Typical sizes of aggregate used in UHPC do not exceed ¼” (5 mm) and are specifically chosen for their high strength and fracture energy [11, 12, 16]. The small aggregate size is chosen because of the relationship between aggregate size and compressive strength and to enable concrete flowability at relatively low water/cementitious ratios [17]. Some types of aggregate used in the production of UHPC include basalt, limestone, calcined bauxite, and silica sand [12, 18]. To aid the UHPC ductility, different types of fibers can be added to the mix. Steel fibers and carbon fibers have both been used in UHPC production [7, 8, 10-12, 16, 18, 19]. An important characteristic of UHPC is its very low water-to-binder ratio. To achieve high strengths in the concrete, the water/binder ratio is required to be below 0.25 and reports have shown that the water/binder ratio can drop to as low as 0.12 while maintaining workability [11, 12, 14]. To compensate for the low amount of water, high-range water-reducing admixtures (HRWRs), more commonly known as superplasticizers, are required. In some cases, the need to offset effect of the high amount of HRWRs, concrete curing accelerators have been used [11, 20].

The process of mixing UHPC is markedly different than the mixing process for normal concrete. There is no standard currently available that addresses the mixing times and addition rates for UHPC. The most noticeable difference in UHPC mixing is the time that it takes for the UHPC ingredients to homogenize. In fact, mixing times in excess of twelve minutes are common [21]. This extended mixing time is mainly due to the low water/binder ratio and high amount of admixtures. Studies have shown that the mixing time to homogenize UHPC is proportional to the amount energy supplied to the mix through the mixing speed and the power supplied to the concrete mixer [21]. Unlike normally vibrated concrete (NVC) and self consolidating concrete (SCC), mixing for extended periods of time does not adversely affect UHPC [21]. A sample mixing procedure provided in a report by the FHWA is as follows [11]:

- Weigh all constituent materials. Add half of HRWA to water.
- Place premix in mixer pan and mix for 2 minutes.
- Add water (with half of HRWA) to premix slowly over the course of 2 minutes.
- Wait 1 minute, then add remaining HRWA to premix over the course of 30 seconds.
- Wait 1 minute, then add accelerator over the span of 1 minute.
- Continue mixing as the UHPC changes from a dry powder to a thick paste. The time for this process will vary.
- Add fibers to the mix slowly over the course of 2 minutes.
- After the fibers have been added, continue running mixer for 1 minute to ensure that the fibers are well dispersed.

UHPC is typically vibrated into the molds in a short period of time. Markeset describes the UHPC after casting as "…very viscous, but still flowable." and "probably pumpable" [16]. Graybeal adds that, "the workability of this UHPFRC changes soon after casting such that, even though initial set has not occurred, further working of the concrete is not possible" [20].

Heat curing of UHPC has positive effects on its compressive strength [11, 12, 20]. Some steam treated specimens have shown compressive strength stabilization after only 48 hours [20]. In addition, it has been shown that delaying steam treatment by up to eight months can still increase the compressive strength of the concrete by up to 25% [11]. UHPC that does not receive steam treatment can continue to gain strength for 8 weeks after casting [20].

Because of its very dense microstructure and enhanced mechanical characteristics, typical relationships used by design codes for normal concrete are inaccurate. Graybeal has determined that the form of the relationship given by the American Concrete Institute (ACI) can be accurate when multiplied by a scalar [20]. The ACI equation takes the form [22]:

$$E = 4730\sqrt{f_c'} \quad \text{in MPa} \tag{2.1}$$

$$E = 57000\sqrt{f_c'} \quad \text{in psi} \tag{2.2}$$

The modified ACI equation for UHPC may take the form:

$$E = 3840\sqrt{f_c'} \quad \text{in MPa} \tag{2.3}$$

$$E = 46200\sqrt{f_c'} \quad \text{in psi} \tag{2.4}$$

where E is the modulus of elasticity and f_c' is the characteristic compressive strength at 28 days of age [20].

Because the stress-strain relationship of UHPC deviates from the typical relationships, an equation relating stress and strain has also been developed. Graybeal gives this relationship through two equations as [20]:

$$f_c = \varepsilon_c E(1 - \alpha) \tag{2.5}$$

$$\alpha = ae^{\frac{\varepsilon_c E}{bf_c'}} - a \tag{2.6}$$

where f'_c is the compressive strength at a given time, ε_c is the strain at a given time, E is the modulus of elasticity of UHPC, α is a reduction factor, and a and b are constants which vary depending on whether the UHPC is stream treated or not. These constants are given in Table 1 [20].

Table 1: Coefficients a and b as reported by Graybeal [20]

	a	b
Steam-treated	0.001	0.24
Untreated	0.011	0.44

Though UHPC has been in existence for over twenty years, its structural applications have been limited. Recently, UHPC has been used in the construction of a pedestrian bridge in South Korea, a highway bridge in Iowa, and a series of canopies in Calgary, Canada [23-25]. In addition, it has been suggested in specific applications, such as for security, blast, and penetration resistance [8, 16]. Because of its increased use in the past ten years, it is apparent that the use of UHPC will continue to grow.

2.3 FIBER REINFORCED POLYMER (FRP) COMPOSITES

Fiber reinforced polymer (FRP) composites have emerged as attractive materials in structural engineering. FRP is a composite consisting of a resin, typically an epoxy, vinyl ester, or polyester and a specific type of fiber. Because carbon fiber reinforced polymer (CFRP) has been used in the experimental work for this thesis, a short review of CFRP is provided. There are two other main types of fiber reinforced polymers in use today: aramid fiber reinforced polymers (AFRPs), and glass fiber reinforced polymers (GFRPs). All types of FRP exhibit high tensile strength, low density, and are noncorrosive [2, 26]. Typical mechanical properties of these types of unidirectional FRP composites for can be found in Table 2. CFRP displays the highest elastic modulus, has a wide range of ultimate tensile strengths, and has relatively low rupture strain. Of the three, CFRP has the highest tensile strength, is least vulnerable to creep-rupture, and is least susceptible to fatigue failure. CFRP also exhibits less tolerance to impact than both AFRP and GFRP [26].

Table 2: Typical tensile properties of fibers used in FRP systems from ACI 440 [26]

FRP-system description	Elastic modulus	Ultimate Tensile strength	Rupture strain at 0 degrees,
	ksi (GPa)	ksi (MPa)	%
CFRP	15000 to 21000 (100 to 140)	150 to 350 (1020 to 2080)	1.0 to 1.5
GFRP	3000 to 6000 (20 to 40)	75 to 200 (520 to 1400)	1.5 to 3.0
AFRP	7000 to 10000 (48 to 68)	100 to 250 (700 to 1720)	2.0 to 3.0

The use of FRP also has its disadvantages. FRP does not show plastic yielding, thus, failure can be abrupt. Environmental conditions also affect the mechanical properties of FRP. ACI Committee on FRP (ACI-440) lists alkalinity, salt water, chemicals, ultraviolet light, high temperatures, high humidity, and freezing and thawing cycles as conditions that can degrade FRP [26]. Because of its constituent materials, CFRP is conductive whereas AFRP and GFRP are both insulators. This conductivity can pose a problem if it comes into contact with steel, as it will lead to corrosion. All types of FRP feature low fire resistance. The limited strain at failure of FRP results in using special design methods to ensure structural ductility prior to failure

2.4 STRENGTHENING REINFORCED CONCRETE STRUCTURES

Because of steel corrosion, increased loading, poor maintenance, and the deterioration of concrete, reinforced concrete (RC) structures may require additional strength to remain serviceable [2]. Historically, external post-tensioning, externally bonded steel plates, and steel or concrete jackets have been used to address this problem [26]. The use of FRP sheets has emerged as an alternative to the traditional strengthening methods.

2.4.1 MECHANICS OF RC STRENGTHENING WITH FRP

The mechanics for strengthening existing concrete structures are similar to the mechanics of regular reinforced concrete. The following assumptions are made for the derivation of the capacity of strengthened structures:

- Plane sections remain plane
- There is no slip between the concrete surface and FRP (perfect bond)
- Shear deformation in the adhesive layer is neglected
- FRP exhibits a linear elastic stress-strain relationship up to failure
- The tensile strength of the concrete is neglected

ACI Committee on FRP (ACI-440) proposes the following design guidelines. To solve for the capacity of a rectangular section, the value of c must be iterated using Equation 2.7 to Equation 2.10. Failure of the section is either governed by compressive failure in the concrete or rupture or debonding in the FRP. This failure is checked using

$$\varepsilon_{fe} = \varepsilon_{cu}\left(\frac{h - c}{c}\right) - \varepsilon_{bi} \leq \kappa_m \varepsilon_{fu} \tag{2.7}$$

where ε_{fe} is the effective strain in the FRP, ε_{cu} is the ultimate compressive strain in the concrete, which is given as 0.003, ε_{bi} is the initial strain in the bonded substrate, κ_m is a bond dependent coefficient, and ε_{fu} is the ultimate strain the FRP. These and other notations used are shown in Figure 2.1. If the left side of Equation 2.7 governs, the beam will fail in compression. Conversely, if the right side of Equation 2.7 governs, the beam will fail in rupture or debonding of the FRP. The effective stress in the FRP is found using

$$f_{fe} = E_f \varepsilon_{fe} \tag{2.8}$$

and the strain in the steel can be found using

$$\varepsilon_s = (\varepsilon_{fe} + \varepsilon_{bi})\left(\frac{d\text{-}c}{h\text{-}c}\right) \tag{2.8}$$

The strain in the steel can be used to find the stress in the steel using

$$f_s = E_s\varepsilon_s \leq f_y \tag{2.9}$$

It is important to note that the steel in these design recommendations is not assumed to yield. This elastic-plastic behavior is atypical in non-strengthened RC design. The initial assumed value of c can be checked with

$$c = \frac{A_s f_s + A_f f_{fe}}{\alpha_1 f_c' \beta_1 b} \tag{2.10}$$

Once c is found, the nominal moment of the section can be found using

$$M_n = A_s f_s\left(d\text{-}\ \frac{\beta_1 c}{2}\right) + \psi_f A_f f_{fe}\left(h\ \text{-}\ \frac{\beta_1 c}{2}\right) \tag{2.11}$$

where ψ_f is a reduction factor recommended as 0.85.

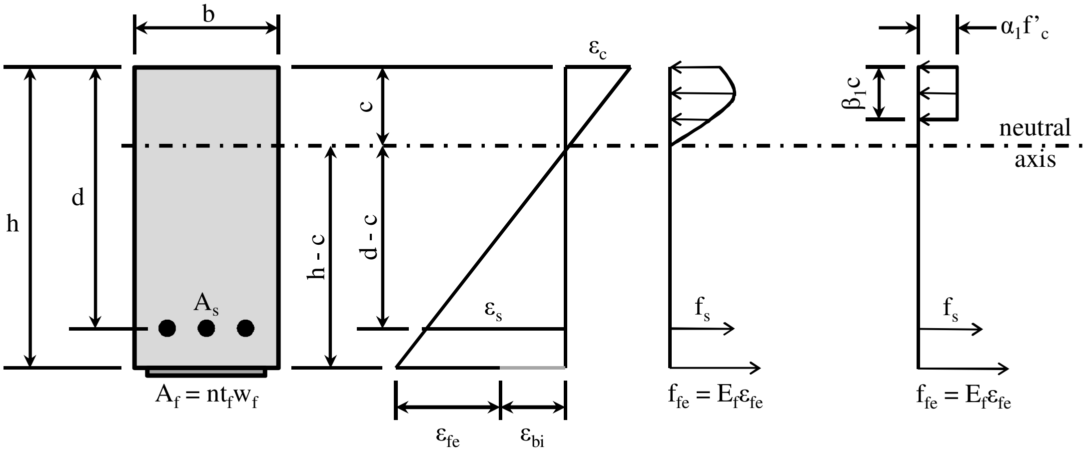

RC section **Strain distribution** **Stress distribution** (Nonlinear concrete stress distribution) **Stress distribution** (Equivalent fictitious concrete stress distribution)

Figure 2.1: Strain and stress distribution of a strengthened concrete beam in flexure [26]

2.4.2 NONLINEAR STRESS-STRAIN RELATIONSHIP FOR CONCRETE

To accurately describe the compressive forces developed in the concrete, the work by Rüsch was employed [27]. Hurbert Rüsch tested concrete specimens in compression at strain rates varying from 0.001/min to 0.001/70 days. This was done because strain is not constant across a flexural member. Using this strain data, Rüsch was able to create a new relationship for stress distribution across a flexural concrete member, as shown in Figure 2.2. Through his work, Rüsch determined that a relationship existed between the ultimate concrete strain, and stress block factors. The stress block factors here are defined as α_R, and β_R which refer to Rüsch.

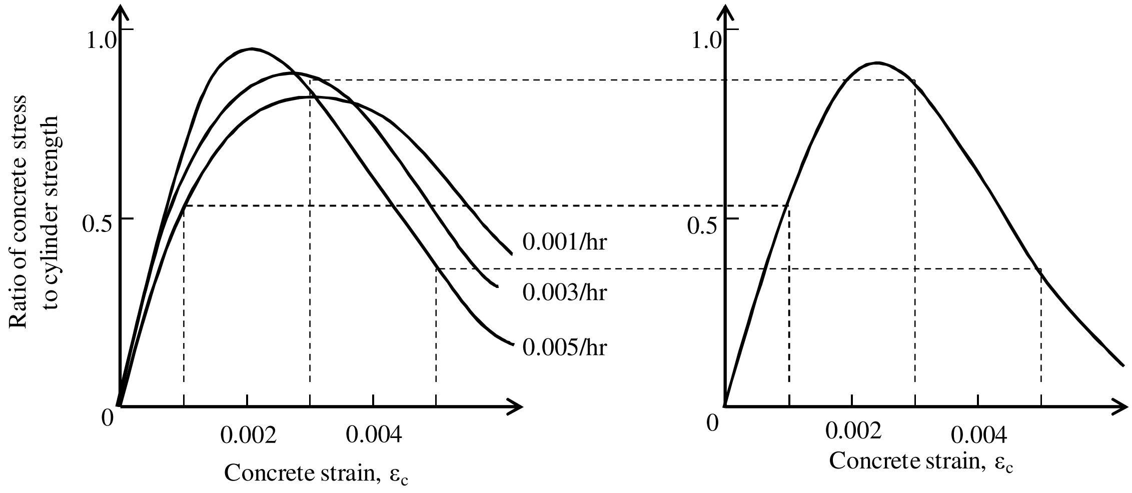

Figure 2.2: Experimental work to determine the stress strain relationship of concrete

The stress block factor is defined as

$$\alpha_R = \frac{f_{avg}}{f_c'} \tag{2.12}$$

and β_R as depicted in Figure 2.3.

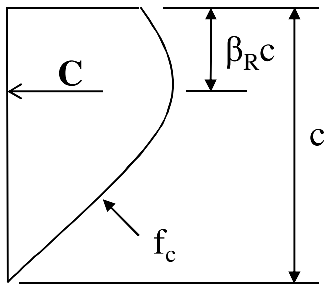

Figure 2.3: Compressive zone in concrete defined by Rüsch [27]

where **C** is the compressive force in concrete, f_c is the stress in the concrete, and c is the depth to the neutral axis. For rectangular cross sections, α_R may be solved using

$$\alpha_R = \frac{1}{f_c'}\int_0^1 f_c(y)dy \tag{2.13}$$

where $f_c(y)$ is a shape function used to describe the stress in concrete. β_R may be solved using

$$\beta_R = 1 - \frac{\int_0^1 y f_c(y)dy}{\int_0^1 f_c(y)dy} \tag{2.14}$$

These factors can be related to α_1 and β_1 described by ACI 318-08 and ACI 440-04 which are based on Whitney's stress block using Equation 2.10 and Equation 2.11. Whitney's stress block can be observed in Figure 2.1 as the equivalent fictitious concrete stress distribution.

$$\beta_R = \frac{\beta_1}{2} \tag{2.15}$$

and

$$\alpha_R = \alpha_1\beta_1 \tag{2.16}$$

2.4.3 CASE STUDIES OF CFRP STRENGTHENING

Strengthening with FRP composites is an attractive method for prolonging the life of a structure. This is due to the low weight of FRP composites compared to the significant mechanical properties which they exhibit. Because of the low weight of the composite, the application of FRP does not contribute significantly to the total loading of the structure [3].

Bridges have been an important area in the application of strengthening with FRP. In 1998, Breña and Steves strengthened a bridge superstructure in Texas to qualify it for widening. The bridge required a 53% increase in flexural capacity. Unidirectional CFRP laminates were affixed to the underside of pan-girders using a wet-layup procedure. The CFRP laminates were adequate in strengthening the bridge [3].

Parretti et. al applied FRP composites to a prestressed concrete bridge girder that was damaged from an accidental impact [6]. For the bridge to continue service, the original design capacity had to be restored. Through the use of CFRP applied using manual lay-up, the damaged prestressed girder was able to be restored to the original design capacity.

In Egypt, Mahfouz and Rizk have applied CFRP strengthening techniques to a hotel and an administrative buildings [28]. In the case of the hotel, CFRP was applied to columns in the hotel that required an increase in flexural capacity of 30%. In the office building, columns required a 25% increase in axial capacity, which was also achieved by the application of CFRP.

CHAPTER 3 EXPERIMENTAL METHODS

This thesis seeks to verify an innovative method for strengthening existing concrete structures. To isolate the positive moment region of a slab, a simply supported beam was created and tested in a four-point bending configuration. To accurately confirm the effectiveness of this new method, two slabs were cast. The first slab served as a control specimen and the second slab that utilized the carbon fiber reinforced polymer (CFRP) and ultra high performance concrete (UHPC) was used to validate the hypothesis. The configuration chosen for the experiment is a four point bending test as shown in Figure 3.1 and idealized in Figure 3.2.

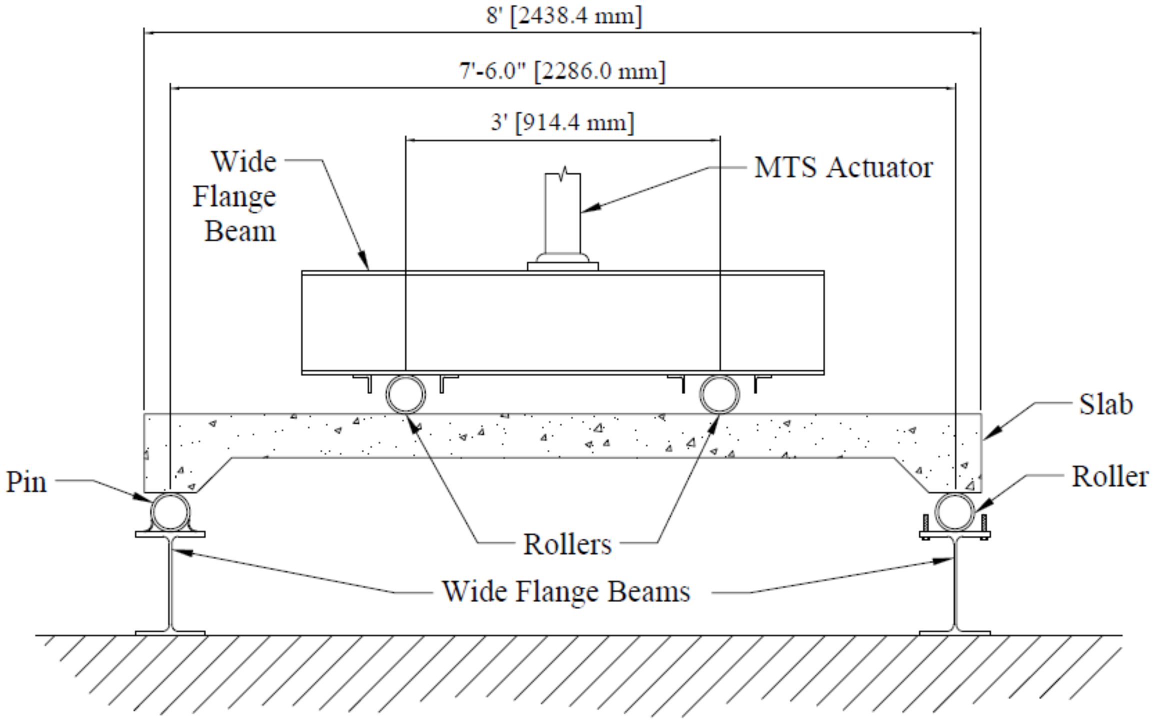

Figure 3.1: Experimental Test Setup

3.1 REINFORCED CONCRETE SLAB

A reinforced concrete slab was cast and tested as a control for the strengthening system.

3.1.1 SETUP

The shear in the slab has a maximum value of P/2 between the supports and the loading points. Two rollers were used as loading points. Between the rollers, there is zero shear force as shown in Figure 3.3. The moment, as shown in Figure 3.4, along the slab increases linearly from the support to the roller, where it achieves a maximum value of 13.5”·P (342.9 mm·P). The four point bending test was chosen because, at the mid-span of the slab, there is an absence of shear forces and a constant moment. This setup exhibits pure bending which makes it simple to analyze.

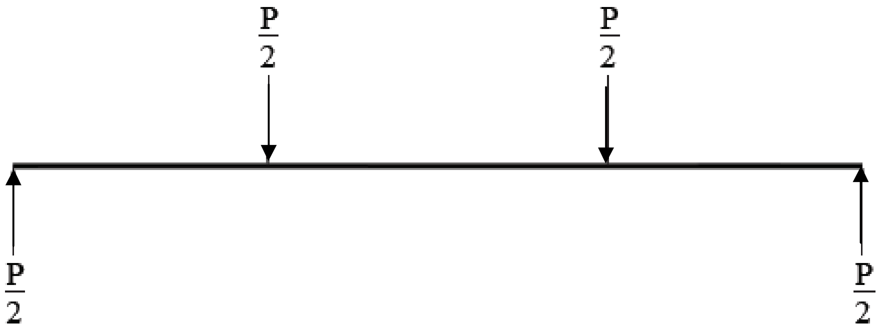

Figure 3.2: Idealized Experimental Setup

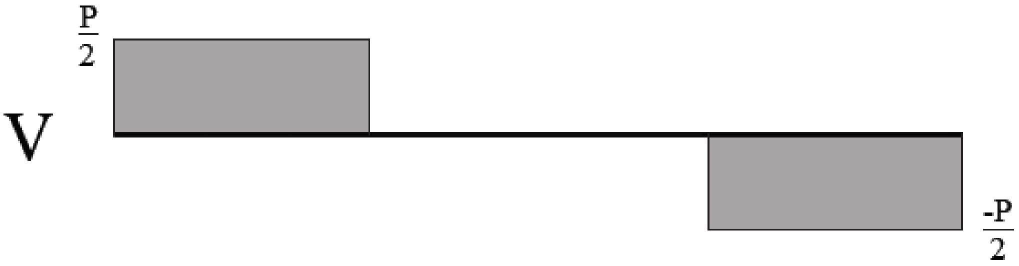

Figure 3.3: Shear Diagram of the Experimental Setup

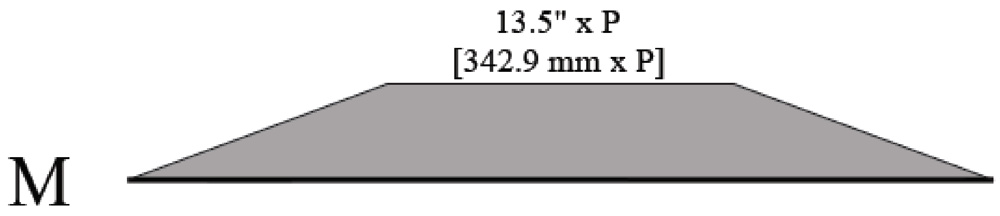

Figure 3.4: Moment Diagram of the Experimental Setup

The MTS actuator used was capable of applying a maximum force of 35 kips (156 kN). The actuator was operated with a hydraulic pump and was controlled by MTS station manager which also provided data acquisition. The wide-flange beams used are all W 12x40 and the pipes are designated as pipe 4 x-strong. These members were chosen because of their minimal deflection resulting from the maximum possible load applied by the actuator. The sections chosen would therefore minimize compliance in the system.

The MTS actuator was bolted to a wide flange beam and applied a load, P, to the system. The wide-flange beam then applied P/2 to each roller. To ensure that minimal horizontal forces were transferred to the RC slab, the only boundary restraint applied to these rollers was a fixed displacement in the vertical direction. The rollers each applied P/2 where they contacted the slab. The slab was supported by an additional pair of pipes that rested on the top of two additional wide flange beams. One pipe was restrained only in the vertical direction and was therefore considered to be a roller. The other support pipe was affixed to the wide flange beam using a series of very small pipes that were welded between the wide flange beam and the pipe. This fixation restrained the pipe from moving in the horizontal direction and effectively created a pinned (hinged) support. This setup is schematically shown in Figure 3.1 and the pin support is shown in Figure 3.5.

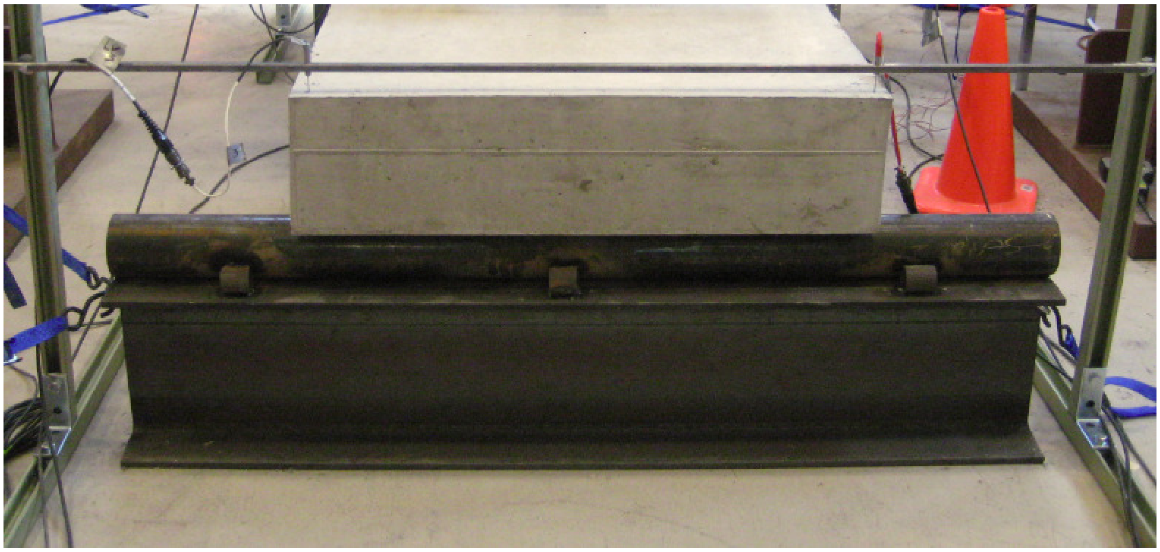

Figure 3.5: The Pinned Connection

To provide adequate safety, two pieces of 2” x 2” (50.8 mm x 50.8 mm) angle iron were used near each unconstrained roller above the slab. These members were solely included to stop the pipes in case of emergency and unexpected movement. This is shown in Figure 3.6. In addition, both wide flange beams beneath the supports were attached to the floor using a system of tie downs. This provided further stability for the structural test. Figure 3.7 shows this connection. The support roller featured six 3/8” (9.5 mm) bolts to restrict large movements in case of an emergency.

Figure 3.6: Angle iron used to restrict unexpected movement

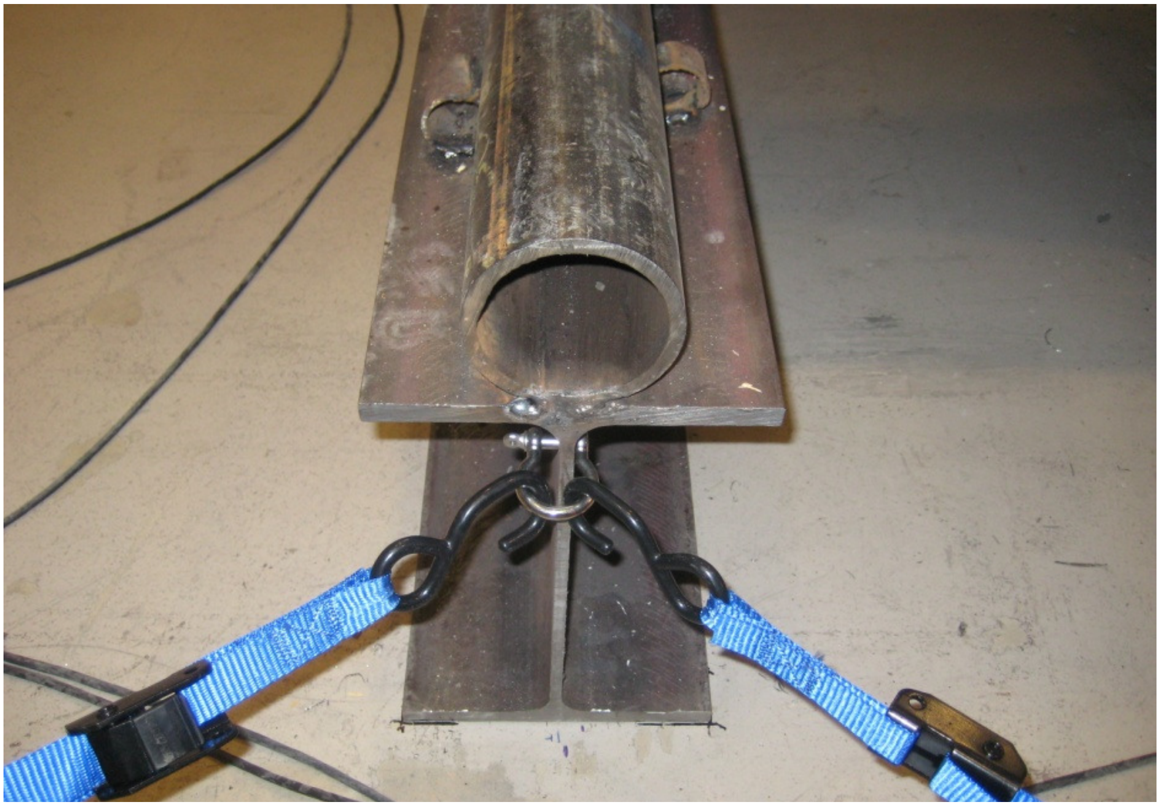

Figure 3.7: Tie Down Connection for Increased Stability

3.1.2 SLAB DESIGN

The slab was designed to fail such that the steel would be beyond its yield point and the final failure would be of the under-reinforced flexural type and would result in yielding of the reinforcing steel and crushing of the concrete. To achieve this, methods presented in ACI 318 were used [29]. Assumptions for the original slab design were the compressive strength, f_c', of the concrete of 6000 psi (41 MPa), steel behaving as elastic-perfectly plastic and having yield strength, f_y, of 60 ksi (414 MPa), the tension in concrete was neglected, a concrete crushing strain, ε_c, of 0.003 was used, and it was assumed that plane sections would remain plane. The typical flexural reinforcement bar chosen was a #4 (#13 SI) bar which had a cross sectional area of 0.196 in^2 (126.5 mm^2). Transverse reinforcement was required to control shrinkage cracks and consisted of #3 (#10 SI) bars with a cross sectional areas of 0.110 in^2 (71 mm^2).

The slab's size is 5" x 36" x 96" (127 mm x 914.4 mm x 2438.4 mm). Rebar chairs were used that provided 1.75" (44.5 mm) clear spacing. This results in d, as used in the following equations being equal to 3" (76.2 mm). The minimum amount of reinforcement was calculated using ACI 318-08:

Imperial:
$$A_{s,min} = \frac{3\sqrt{f_c'}}{f_y} b_w d < 200 \frac{b_w}{f_y} d \tag{3.1}$$

SI:
$$A_{s,min} = \frac{\sqrt{f_c'}}{4f_y} b_w d < 1.4 \frac{b_w}{f_y} d \tag{3.2}$$

which amounts to 0.418 in^2 (269.7 mm^2).

Five #4 (#13 SI) bars for flexural reinforcement were chosen for symmetry with $A_{s,total}$ = 0.98 in^2 (633.5 mm^2) which satisfies the minimum steel reinforcement requirement. The assumed cross section of the slab is shown in Figure 3.8. The spacing of the rebar was chosen to maintain symmetry while also allowing for near-equal sections through the slab. The stress and strain distribution in the slab is shown in Figure 3.9.

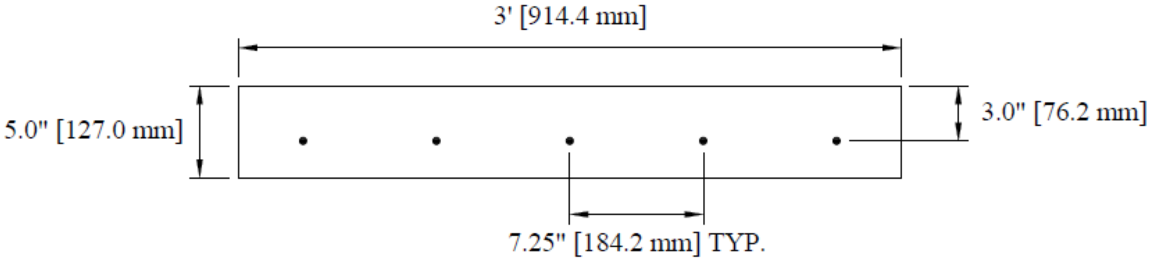

Figure 3.8: Cross Section of the Control Slab

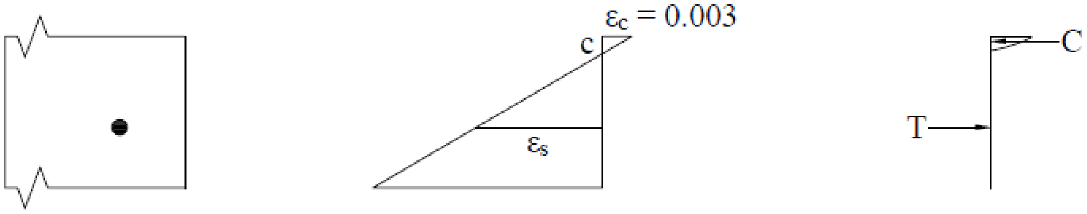

Figure 3.9: Stress and Strain Distribution of the Control Slab

To achieve static equilibrium, the compression in the concrete must equal the tension in the steel:

$$C = T \tag{3.3}$$

which can be rewritten as:

$$\alpha_1 f'_c \beta_1 c b = A_s f_y \tag{3.4}$$

where α_1 and β_1 are the values for the Whitney stress block, and c is the depth to the neutral axis measured from the top of the beam. Using the relationship described by Todeschini [30], as shown in Equation 3.5 to Equation 3.7, α_R is found to be 0.72 and β_R is found to be 0.43.

$$f_c = \frac{2f_c''(\varepsilon/\varepsilon_0)}{1+(\varepsilon/\varepsilon_0)^2} \tag{3.5}$$

where

$$f_c'' = 0.9f_c' \tag{3.6}$$

and ε_0 is the strain when f_c reaches f_c', given by Todeschini as

$$\varepsilon_0 = \frac{1.71f_c'}{E_c} \tag{3.7}$$

Substituting the assumed values into Equation 3.4 yields c as 0.881" (23.3 mm) and the compressive and tensile forces in the RC slab to be 58.91 kip (262 kN).

By summing a moments about the tensile force in the steel, as shown in Figure 3.9, the nominal moment capacity of the slab is shown to be:

$$M_n = \alpha_1 f_c' b \beta_1 c(d - \frac{\beta_1 c}{2}) \tag{3.8}$$

Solving Equation 3.8 results in a nominal moment of 12.87 kip·ft (17.5 kN·m). This corresponds to P = 11.44 kip (50.9 kN). To validate this capacity, it was verified that the assumption of the steel yielding was correct

$$\varepsilon_s \geq \varepsilon_y = 0.002 \tag{3.9}$$

The strain in the steel is calculated using

$$\varepsilon_s = \frac{(d\text{-}c)}{c}\varepsilon_c \tag{3.10}$$

Since the expected strain in the steel is greater than the yield strain, it was determined that the slab would not fail in a brittle manner and the assumption that the reinforcing steel would yield in the control slab was validated.

For practical purposes, two supports were designed at the longitudinal ends of the slab, as shown in Figure 3.1. This was done to ease transportation and setup of the slab for testing. These supports required additional structural steel to resist cracking. Five #4 (#13 SI) stirrups were included to guarantee that flexural or shear failures would not happen at the discontinuities at the supports.

The shear reinforcement was also designed in accordance with ACI 318-08. Using the shear definition from Figure 3.3, it can be inferred that the ultimate shear stress, V_u, resulting from the assumed conditions would be 5.72 kips (25.4 kN). Applying the shear strength reduction factor, $\varphi_v = 0.75$, gives the nominal shear stress, V_n, as 7.62 kips (33.9 kN). From ACI Section 11.5.5.1 [29], no stirrups are required for slabs if

$$V_n \leq V_c \tag{3.11}$$

where

Imperial: $$V_c = 2\sqrt{f'_c}\,b_w d \tag{3.12}$$

SI:
$$V_c = \frac{\sqrt{f'_c}}{6} b_w d \tag{3.13}$$

Substituting the values for the slab, the shear strength of the slab, $V_{c,}$ was found to be 16.7 kips (74.4 kN). This relates to an applied force of 33.5 kip (148.8 kN) using the relationship given in Figure 3.3. Since the shear strength of the concrete is greater than the nominal shear stress, there was no need for shear reinforcement in the slab.

Per ACI Section 7.12.2.2, shrinkage and temperature reinforcement spacing shall not exceed 18” (450 mm) or 5 times the thickness of the slab [29]. To ensure that shrinkage or temperature cracks did not occur, 12” (304.8 mm) has been used as the transverse rebar spacing. #3 (#10 SI) bars were chosen for this reinforcement. The final designed profile of the control slab is shown in Figure 3.10.

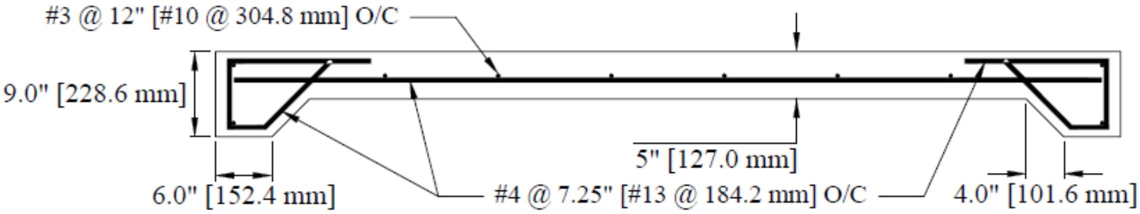

Figure 3.10: Rebar profile detail

3.1.3 FORMWORK AND REINFORCEMENT

The forms for the control slab were constructed out of wood. They were sealed to protect the wood from warping as the concrete set in addition to retaining moisture in the concrete as it cured. Silicon was placed in all of the joints of the form to further prevent water from escaping the curing concrete. The forms were assembled so that they were easy to disassemble. Figure 3.11 shows the formwork prior to casting.

Figure 3.11: Concrete formwork

The reinforcing bars were placed with the aid of plastic chairs which, as mentioned previously, provided 1¾” (44.5 mm) of clear cover. At each junction, the two intersecting bars were tied together using steel wire. 2” (50.8 mm) of cover was provided on all edges of the rebar except in the feet of the slab where ¾” (19.1 mm) was used. The steel cage prior to casting is shown in Figure 3.12. A pallet jack was used for easy transportation of the formwork.

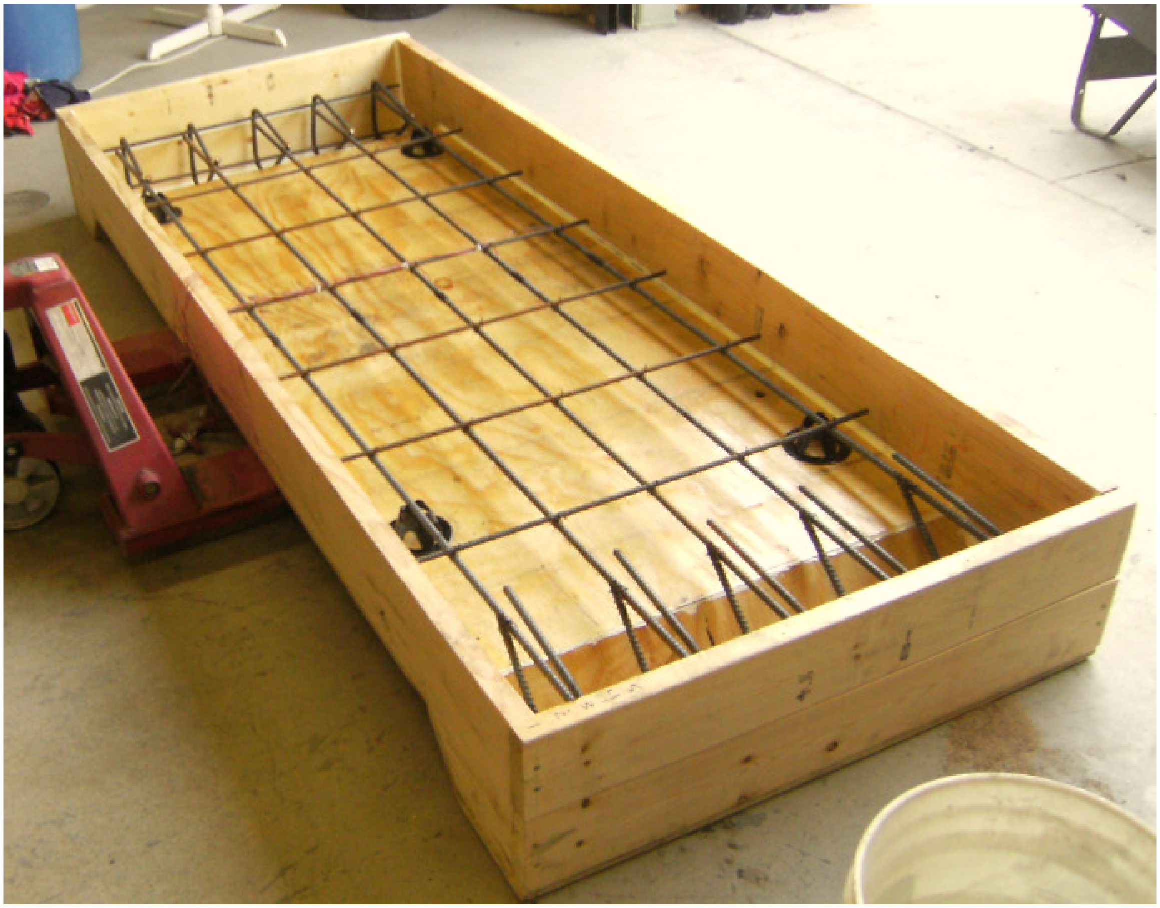

Figure 3.12: Reinforcement bar layout in the formwork

3.1.4 CONCRETE CASTING

The concrete used was a typical normal vibrated concrete (NVC). This concrete was chosen because of its relatively low strength and because of material availability. The concrete was expected to have a compressive strength near 6000 psi (41 MPa). The fine aggregate and coarse aggregate were obtained locally in Albuquerque, NM and the fly ash was obtained from Farmington, NM. The fly ash was used in the mix as it prevents an alkali silica reaction between the aggregate and cement which is common in New Mexico aggregate [31]. The superplasticizer used was BASF Glenium 3030NS.

In addition to casting the slab, cylinders were cast to provide compressive strength and splitting tension results at 7 and 28 days of age and at the day of the test. A large volume of fresh concrete was needed for measurement of entrained air and specific gravity as well as for slump cone tests. Thus, about 15.84 ft^3 (0.449 m^3) of concrete was cast to provide all of the concrete for the slab and testing specimens.

Due to size limitations for mixing capacity, three different batches were cast. The first batch provided the standard for workability for the second and third. The casting process is shown in Figure 3.13 and Figure 3.14. The unset finished slab is shown in Figure 3.15. The results from the slump cone tests for all three batches are given in Table 3. The close numbers for slump cone results demonstrate the consistency achieved between the three different batches. A concrete vibrator was used during the casting so that voids were minimized. The slab was finished using a hand float. The finished concrete slab is shown in Figure 3.15. A pallet jack was used to prevent bowing of the main piece of plywood at the bottom of the slab. Table 4 lists other properties measured during the casting of the NVC.

The control slab was allowed to set for one day and was then cured for 28 days. Curing the slab was achieved by soaking a canvas drop cloth and wrapping the control slab and canvas in a plastic tarp. Water was applied to the canvas every day. The cylinders were kept in a controlled environment with 97% relative humidity and a constant temperature of 68°F (20°C). The compressive and splitting tension strengths are shown in Table 5 along with their respective standard deviations. The compression test used followed ASTM C39 specifications and the splitting tension test followed ASTM

C496 [32, 33]. To ensure that the top and bottom of the cylinders were parallel, the cylinders were capped using sulfur.

Table 3: Slump cone test results for the control slab

Mix	Measured Slump, in (mm)
1	5.5 (140)
2	5.5 (140)
3	5.0 (127)

Table 4: Measured properties of the concrete for control slab

Unit Weight (lb/ft^3) (kN/m^3)	Air Entrained (%)
143.82 (22.59)	1.9

Table 5: Concrete strengths and standard deviations for the control slab

Specimen Age	Compressive Strength, psi (MPa)	Standard Deviation, psi (MPa)	Tensile Strength, psi (MPa)	Standard Deviation, psi (MPa)
7 Days	4211 (29)	165 (1.1)	390 (2.7)	26 (0.18)
28 Days	5423 (37)	307 (2.1)	431 (3.0)	26 (0.18)
91 Days (Experiment)	6749 (47)	376 (2.6)	471 (3.2)	27 (0.19)

Figure 3.13: Casting the control slab

Figure 3.14: Finishing the control slab

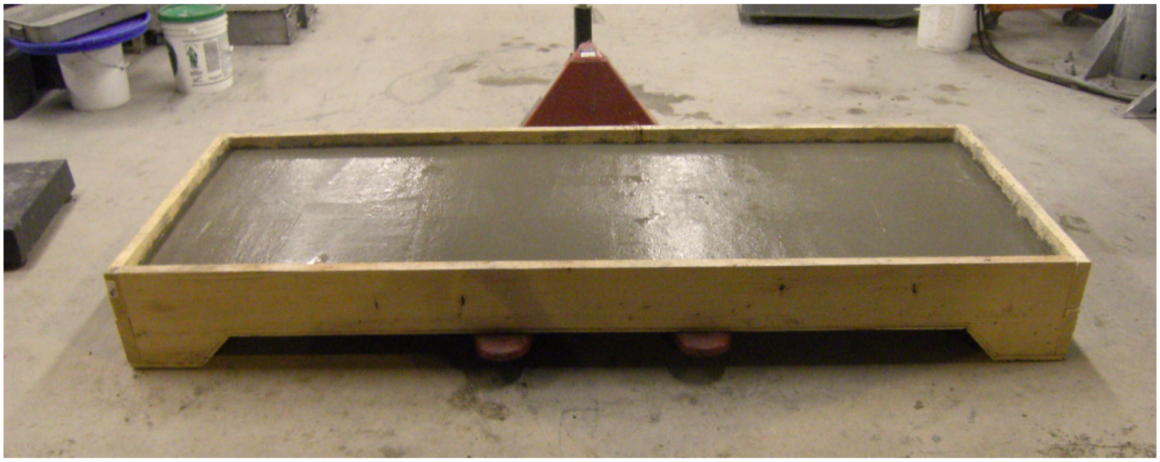

Figure 3.15: The finished control slab

3.1.5 STRAIN GAUGE LOCATIONS

As part of the data acquisition, nine strain gauges were installed on the control slab. The strain gages that were used in this work were purchased from Vishay. Product C2A-06-250LW-120 was used for the reinforcing steel and product N2A-06-20CBW-120/P was used on the exterior of the concrete. All surface preparation was completed according to Vishay Precision Group Instruction Bulletin B-129-8 [34].

One strain gauge was installed in the center of each longitudinal rebar. These strain gauges were installed on the bottom of the rebar, which provides direct analysis of the strain at depth d_t, the distance from the extreme compression fiber to the extreme tension steel. One of the installed strain gauges is shown in Figure 3.16. Because of the uncertainty of installing strain gauges inside of a concrete structure, the strain gauges were protected with rubber tape. This protection scheme is shown in Figure 3.17. All five gauges installed functioned, but only three were added to the system. The two edge reinforcement bar gauges and the center reinforcing bar gauge were used.

Four gauges were applied at center span on the exterior of the concrete. Strain gauges were applied on the top of the slab, on the bottom of the slab, and on the side of the slab. The first gauge installed on the side of the slab was located 1” (25.4 mm) from the top and the second gauge was located 2.5” (63.5 mm) from the top. Strain gauges were installed according to Vishay Precision Group Application Note TT-611 [35]. This process involved preparation of the concrete surface, application of an adhesive, surface preparation of the adhesive, and strain gauge installation.

A Vishay 2100 Signal Conditioning Amplifier System was used to regulate bridge excitation levels which were set per Vishay Technical Note 502 [36]. All strain gauges were excited to 2V DC. The signal conditioner was added to the MTS data acquisition system for measurement.

Figure 3.16: Strain gauge on a reinforcement bar

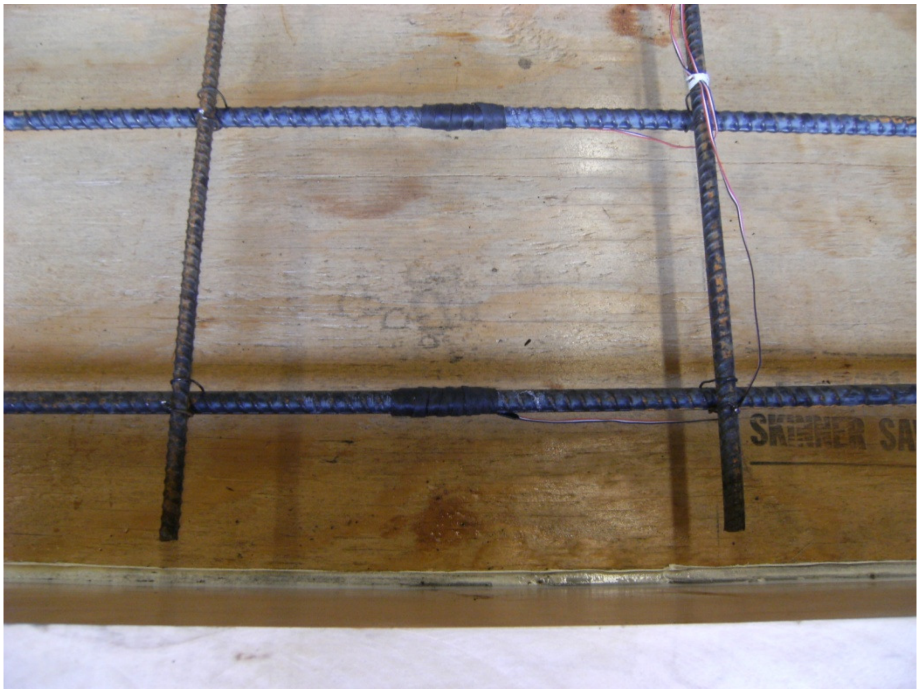

Figure 3.17: Embedded strain gauge protection

Figure 3.18: Strain gauges on the exterior of the control slab

3.1.6 LVDT LOCATIONS

Linear variable differential transducers (LVDTs) were used to measure linear displacement. Six LVDTs were used in the experiment. Two LVDTs were located at the center of the span and were essential to calculating the displacement of the test without the effects of frame compliance. One LVDT was located at each corner of the slab at 1" (25.4 mm) from the longitudinal end and 1" (25.4 mm) from the transverse end. These four LVDTs were installed to be used to calculate the curvature of the specimen as the test proceeded. A system of struts was constructed to securely position the LVDTs. The LVDTs were calibrated to 99.9% accuracy over their entire range prior to commencing the test.

3.2 STRENGTHENED REINFORCED CONCRETE SLAB

A second slab was cast to apply the new strengthening method. A replica of the control slab was cast that contained the same dimensions, mix design, and flexural steel reinforcement. The same boundary conditions and LVDT locations were applied during the testing of the slab. This section describes the differences between the strengthened and the control slab.

3.2.1 SLAB DESIGN

The strengthened slab contained two 0.045" x 12" x 72" (1.143 mm x 304.8 mm x 1828.8 mm) unidirectional carbon fiber reinforced polymer (CFRP) sheets attached to its top. Above the CFRP sheets was a 1.5" (38.1 mm) thick layer of UHPC with a required compressive strength, f_{UHPC}, greater than 20 ksi (138 MPa). Figure 3.19 shows the cross section of this configuration. The same assumptions of steel having elastic-perfectly plastic behavior with yield strength, f_y, of 60 ksi (414 MPa), and neglected tension in the concrete were maintained. The compressive strength of the UHPC was assumed to be 22.5 ksi (155 MPa) based on trial batch results and the UHPC crushing strain, ε_{UHPC}, was assumed to occur at 0.0039 based on the literature [20]. The CFRP was assumed to be linear elastic with a modulus of elasticity of 18000 ksi (124106 MPa) and a maximum tensile strength, f_t, of 390 ksi (2690 MPa) based on manufacturer data and the typical properties of CFRP presented in Table 2. The stress and strain distributions for this second slab are shown in Figure 3.20. In order for the CFRP to be in tension, the neutral axis must rise above its original location and reside in the UHPC. Because of the additional depth added to the slab by the UHPC, the depth to steel, d, is now 4.5” (114.3 mm).

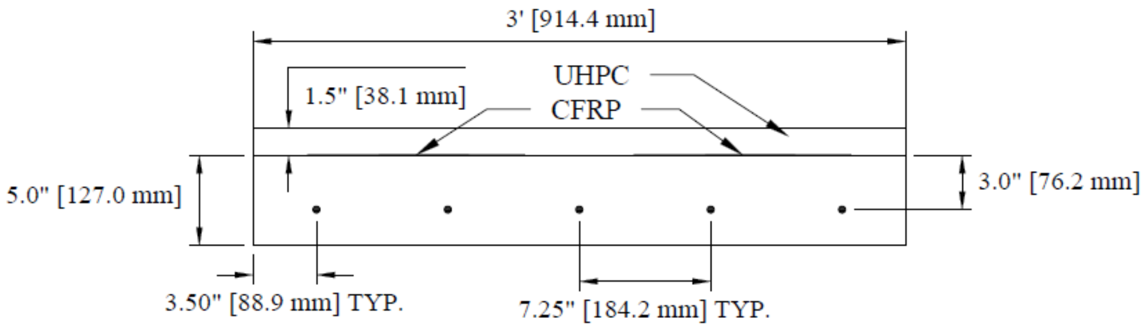

Figure 3.19: Cross section of the strengthened slab

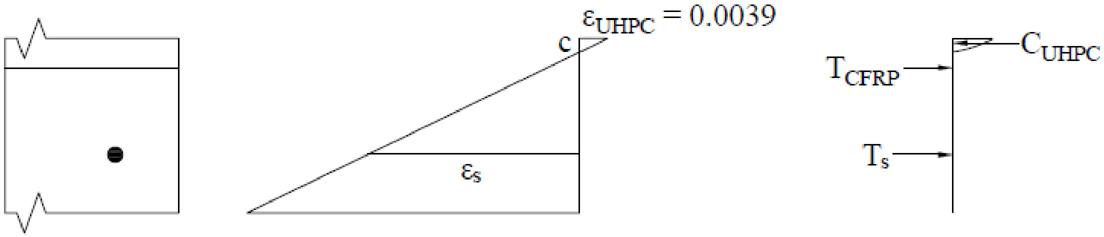

Figure 3.20: Stress and strain distribution of the strengthened slab

The mechanics of the strengthened concrete slab differed from the first. To satisfy equilibrium at failure

$$\sum C = \sum T \tag{3.14}$$

which can be rewritten as

$$C_{UHPC} = T_{CRFP} + T_s \tag{3.15}$$

or

$$\alpha_1 f'_{UHPC} b \beta_1 c = A_{FRP} f_{CFRP} + A_s f_s \tag{3.16}$$

where β_1 and α_1 are the coefficients of the Whitney stress block. The factors α_R and β_R were used in conjunction with the stress-strain relationship of the UHPC defined by Graybeal using the constants a and b for steam curing [20, 27]. Based on this relationship and the aforementioned assumptions, α is 0.61 and β is 0.36. One other relationship is used to find the depth to the neutral axis, c.

$$\varepsilon_{CFRP} = \frac{\varepsilon_{UHPC}(h_{UHPC} - c)}{c} \tag{3.17}$$

Using the strain in the CFRP, it is possible to find the corresponding force by using the elastic modulus. To solve for the depth to the neutral axis, c, one can iterate to satisfy Equation 3.16 and Equation 3.17. After converging on a value for c, the strain in the steel is checked to ensure yield using

$$\varepsilon_s = \frac{\varepsilon_{UHPC}(d_s - c)}{c} \tag{3.18}$$

Using the assumed values and iterating, it can be found that the depth to the neutral axis, c, is equal to 0.768” (19.5 mm). The nominal flexural capacity of the system, M_n, can be determined using the equilibrium diagram shown in Figure 3.20 and Equation 3.17.

$$M_n = C_{UHPC}(h_{UHPC} - \frac{\beta_1 c}{2}) + T_s(d - h_{UHPC}) \qquad (3.19)$$

The flexural capacity of the strengthened section was found to be 28.50 kip·ft (38.6 kN·m) which, using the relationship shown in Figure 3.4, corresponds to a load of 25.33 kip (112.7 kN). This theoretically results in approximately 121% more capacity when compared to the control slab.

Other design considerations taken into account focused on the bond between the slab, CFRP, and UHPC. The CFRP was glued to the concrete slab using a high strength epoxy. To bond the UHPC to the slab, shear-friction reinforcement was used.

Equation 11-25 from ACI 318-08 gives the nominal shear-friction, V_n, between two concrete layers as [22]

$$V_n = A_{vf} f_y \mu \qquad (3.20)$$

where A_{vf} is the area of the shear-friction reinforcement, f_y is the yield strength of the shear-friction reinforcement, and μ is the coefficient of friction. For concrete placed against hardened concrete not intentionally roughened, as specified in ACI 318-08 Section 11.7.9, $\mu = 0.6$ for normal weight concrete. #3 (#10 SI) bars were chosen to be used for all of the shear-friction reinforcement.

Using the relationship given in Figure 3.3 and the calculated load which was solved for previously, it can be shown that each side of the slab requires 0.36 in^2 (233 mm^2) of shear-friction reinforcement. To remain conservative and guarantee composite action of the UHPC, 3 u-shaped stirrups were used on each side of the slab which amounts to 0.66 in^2 (426 mm^2) of shear-friction reinforcement per side. To prevent debonding of the UHPC from the slab at center span due to potential buckling, four rebar dowels were chosen to bond the concrete slab with the UHPC. Figure 3.21 details the locations of the shear-friction reinforcement and CFRP sheets. The CFRP sheets were mechanically anchored to the NVC substrate using two shear-reinforcement bars. In construction, the bars may need to be isolated from the CFRP to prevent galvanic reaction by making the hole in the CFRP larger where the rebar bonds to the existing concrete substrate or by using a protective isolating sheath around the bar at the CFRP contact.

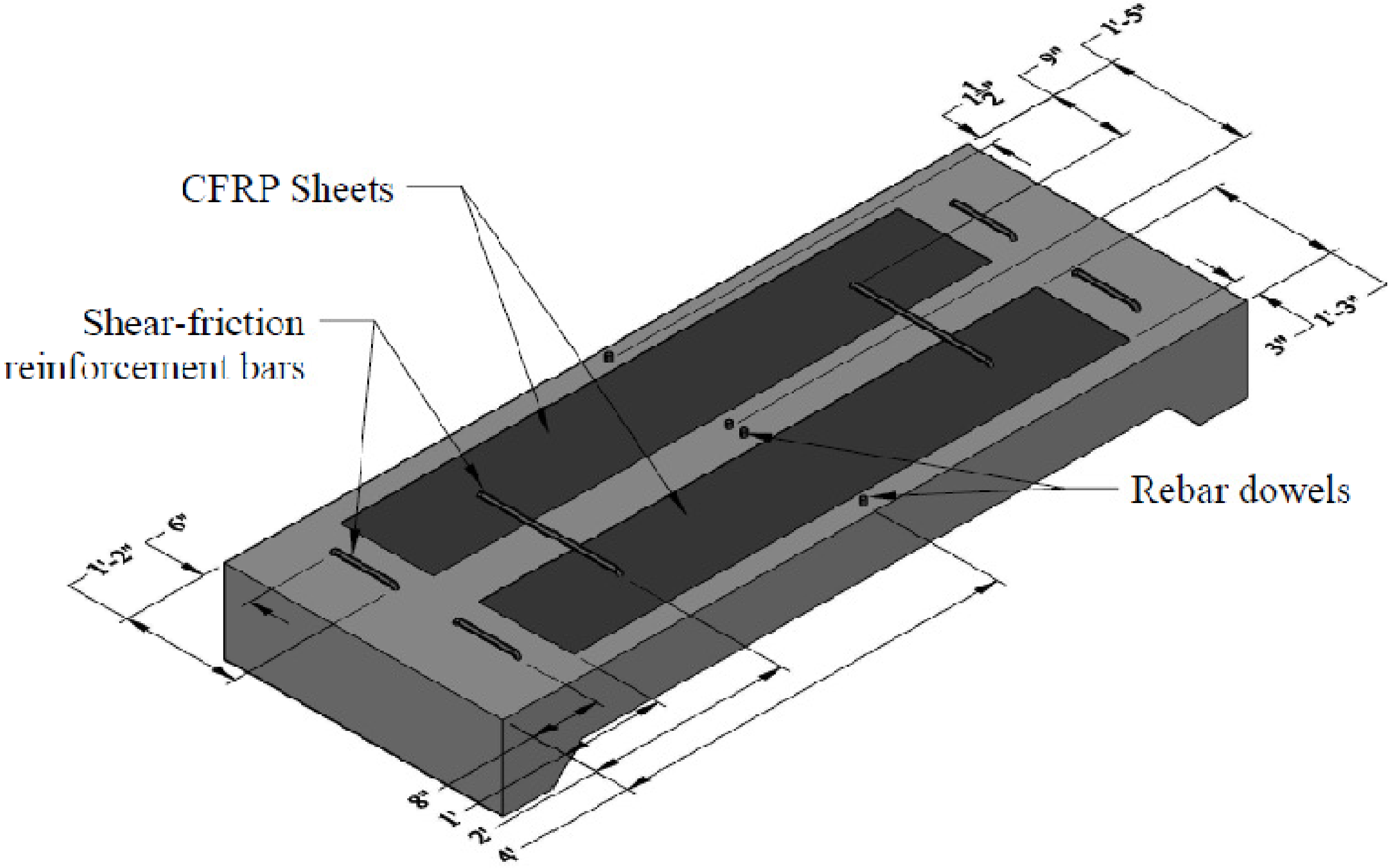

Figure 3.21: CFRP laminate and shear-friction reinforcement layout and dimensions

(1” = 25.4 mm)

3.2.2 CONCRETE AND REINFORCEMENT TESTING

The concrete for the NVC portion of the strengthened slab followed the same proportioning as the control slab and was also cast in three different batches. To verify that the fresh concrete was similar to the concrete used in the control slab, slump cone tests were performed. The results for the slump cone test are given in Table 6. The slump cone results are less than 1" (25.4 mm) different than the mixes for the control slab. This shows the consistency between all six mixes. The measured properties given in Table 7 and Table 8 are also similar to the results from the NVC used in the control slab given in Table 4 and Table 5.

Table 6: NVC slump cone results for the strengthened slab

Batch	**Measured Slump, in (mm)**
1	4.75 (120.7)
2	5.00 (127.0)
3	4.75 (120.7)

Table 7: Measured properties of the strengthened slab NVC

Unit Weight (lb/ft^3) kN/m^3	**Air Entrained (%)**
143.69 (22.57)	2.0

Table 8: NVC strengths and standard deviations for the strengthened slab

Specimen Age	**Compressive Strength, psi (MPa)**	**Standard Deviation, psi (MPa)**	**Tensile Strength, psi (MPa)**	**Standard Deviation, psi (MPa)**
7 Days	3924 (27)	185 (1.3)	341 (2.4)	12 (0.08)
28 Days	5558 (38)	242 (1.7)	462 (3.2)	30 (0.21)
41 Days (Experiment)	5591 (39)	307 (2.1)	467 (3.2)	20 (0.14)

The CFRP used was a pre-cured unidirectional CFRP laminate (strip) manufactured by Graphtek LLC that used a vinylester resin. The mechanical properties of the CFRP, as provided by the manufacturer, are shown in Table 9 below. The CFRP was assumed to behave in a linear-elastic fashion to failure. Reaching the ultimate tensile strength of the CFRP would result in a brittle failure.

Table 9: CFRP characteristics as reported by the FRP manufacturer

Property	Value	
Fiber Modulus of Elasticity	33,000 ksi	227.5 GPa
Tensile Strength	390 ksi	2690 MPa
Flexural Strength	272 ksi	1875 MPa
Density	0.054 lb/in^3	0.147 N/mm^3

The CFRP was bonded to the slab using a high strength epoxy manufactured by West System. To ensure that there were no voids between the slab and the CFRP sheets; epoxy was applied to both surfaces, as shown in Figure 3.22. The surface was prepared and the CFRP strips were attached. There were no visible cracks in the slab or uneven surfaces. Pressure was applied to the sheets using a system of angle iron and concrete blocks for 24 hours. After the epoxy had set, the weights were removed and the CFRP was checked for voids. If a void was present, a small hole was drilled through the CFRP and epoxy was injected to fill the void.

Figure 3.22: Application of the epoxy to the CFRP and slab

To maintain similarity with field application of this strengthening system, the concrete slab was cast without the shear-friction reinforcement. Instead, the holes for the reinforcement were drilled after the slab had been cured for 7 days using a hammer drill with a ½" (12.7 mm) masonry bit. The shear-friction reinforcement was bonded to the slab using Sika AnchorFix-2 anchoring adhesive. The CFRP and part of the shear-friction reinforcement can be seen in Figure 3.23.

Figure 3.23: CFRP and shear-friction reinforcement

The UHPC chosen was a modified version of a UHPC made by Reda Taha et al. [12]. Many trial batches were cast to guarantee optimal workability and performance. The UHPC was cast in a Sicoma planetary shear mixer in the UNM Concrete Laboratory. The mixer is shown in Figure 3.24. The water-to-cementitious-materials ratio was very low, at 0.18. This water-to-cementitious-ratio directly relates to the high strengths achieved by the UHPC.

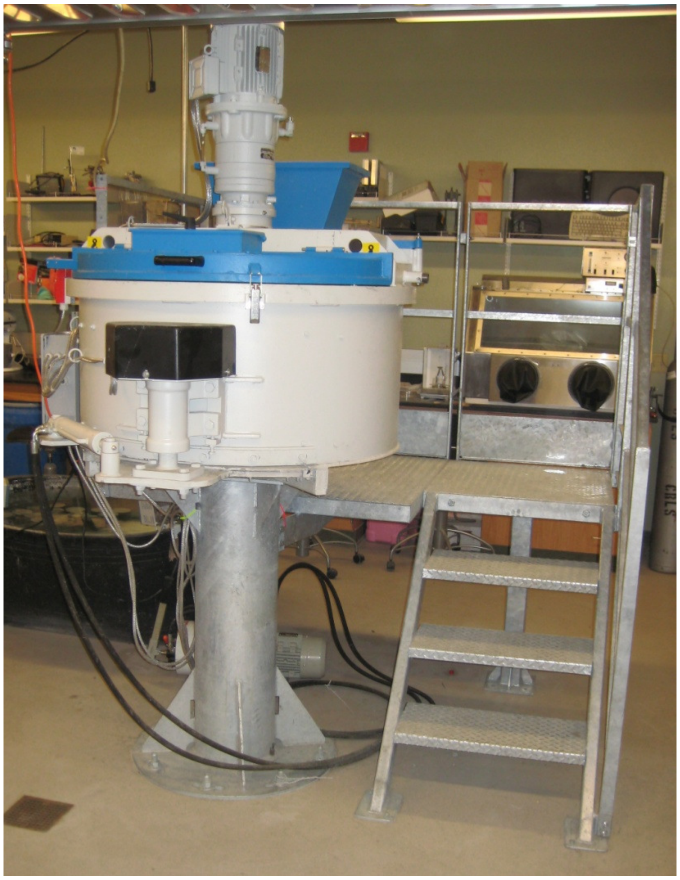

Figure 3.24: Sicoma planetary shear mixer used for producing UHPC

Calcined bauxite is a high alumina aggregate. It was chosen specifically for use in UHPC because of its high hardness and strength. The nominal maximum size of the bauxite chosen is 0.187 in (4.8 mm). The small aggregate size was chosen to further increase strength [17]. The UHPC was cast with the following schedule:

- Start mixing the aggregate and add the cement and silica fume each over 2 minutes
- Add 45% of the water over 30 seconds
- Add 45% of the superplasticizer over 30 seconds
- Mix for 5 minutes
- Add 45% of the water over 30 seconds

- Add 45% of the superplasticizer over 30 seconds
- Wait until the concrete begins to form into small spheres and begins to glisten. Once it does, add part of the remaining 10% of the water and 10% of the superplasticizer to achieve the desired workability
- Mix for an additional 2 minutes to verify workability

Due to mixer size constraints, the UHPC was cast in two batches. During the initial set of the UHPC, a canvas was placed above it and moistened to prevent cracking. This is shown in Figure 3.25. Figure 3.26 shows the first batch and Figure 3.27 shows the finishing of the second batch. Fourteen cylinders (4” x 8”, 101.6 mm x 203.2 mm) were also cast to evaluate the material properties of the UHPC.

Figure 3.25: Canvas to prevent cracking during the initial set of the UHPC overlay

Figure 3.26: Casting the first UHPC batch

Figure 3.27: Finishing the second UHPC batch

As discussed previously, UHPC requires heat curing to reach its high strengths. To address this, a 5’ x 10’ x 1¼’ (1524 mm x 3048 mm x 381 mm) hot bath was constructed out of wood. An impermeable rubber sheet was used to line the wood. Three tank heaters were used to maintain heat in the tank as well as to circulate the water. To further increase the temperature of the water, Styrofoam was cut and placed over the tank. The entire setup of the curing tank is shown in Figure 3.28. The tank was able to maintain a constant temperature of 150 °F (66 °C) for the duration of curing.

Figure 3.28: UHPC curing tank

The four different mechanical properties measured were compressive strength, splitting tensile strength, elastic modulus, and Poisson’s ratio following standards ASTM C39, ASTM C496, and ASTM C469 respectively [32, 33, 37]. The cylinders used for evaluation of the compressive test and elastic modulus were ground to ensure that the top and bottom of the cylinders were parallel. The cylinders were ground because the normal method of sulfur capping does not work for UHPC due to UHPC's very high strength. The mechanical properties for the UHPC testing are given in Table 10.

Table 10: Physical properties of UHPC

Specimen Age	Compressive Strength, psi (MPa)	Standard Deviation, psi (MPa)	Tensile Strength, psi (MPa)	Standard Deviation, psi (MPa)	Elastic Modulus, psi (MPa)	Poisson's Ratio
7 Days	20954 (144)	859 (5.9)	-	-	-	-
15 Days (Experiment)	22265 (154)	717 (4.9)	1128 (7.8)	18 (0.12)	6935023 (47815)	0.20

3.2.3 STRAIN GAUGE LOCATIONS

Eight strain gauges were used in testing the strengthened concrete slab. The same procedures for application as described in Section 3.1.5 were used. Strain gauges were applied to the same locations on the flexural reinforcement steel, along the side of the slab, and on the bottom of the NVC, just as with the control slab. Two additional strain gauges were applied on top of the CFRP sheets as shown in Figure 3.29. These strain gauges were very critical because they were used to monitor CFRP strain as it moved from compression to tension. Finally, one strain gauge was applied to the top of the UHPC overlay to measure the compression strain in the UHPC.

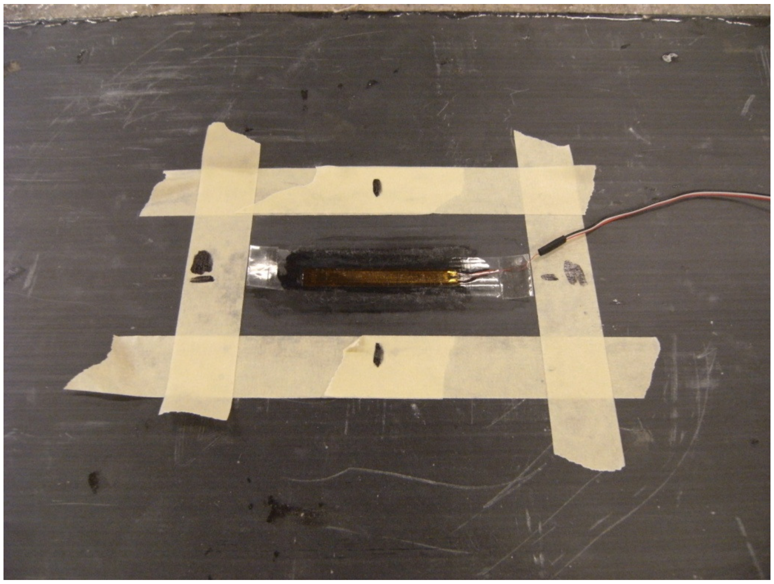

Figure 3.29: CFRP strain gauge application

3.3 REINFORCING STEEL PROPERTIES

The stress-strain curve of the reinforcing steel was determined experimentally. This is because of the strain hardening that occurs after yield. The steel reinforcing bar section was tested using ASTM E8 [38]. Yield of the steel reinforcement occurred at approximately 72 ksi (496 MPa) and strain hardening results in a maximum stress of approximately 108.7 ksi (750 MPa). Figure 3.30 shows the reinforcement bar after fracture in the universal testing machine. Necking of the rebar is clearly visible.

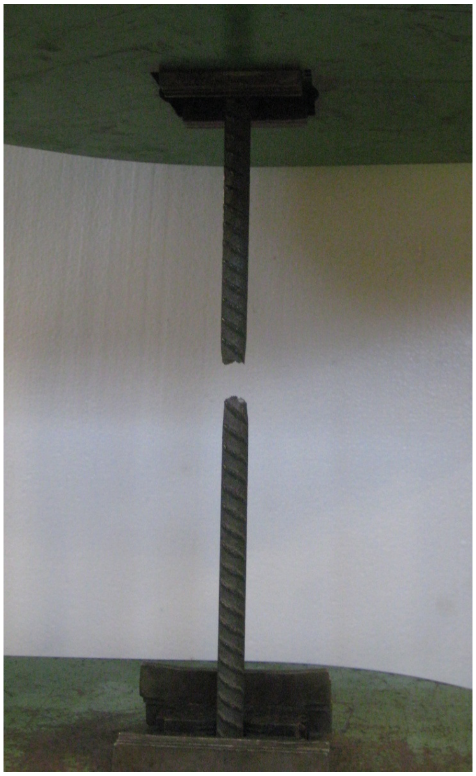

Figure 3.30: Direct tension test of the flexural steel

3.4 CFRP PROPERTIES

CFRP strips were tested using an MTS Bionix UTM in the University of New Mexico Structural Laboratory. An extensometer was used to measure longitudinal strain in the CFRP and a strain gage was used to measure the transverse strain in the CFRP. The test setup is shown in Figure 3.31. Mechanical grips were used to vertically restrain the CFRP. Because of slipping in the mechanical grips at increased loads, the CFRP was unable to fail. The elastic modulus and Poisson's ratio were calculated from the clip gage and strain gage data. The stress-strain relationship for the CFRP is shown in Figure 3.32 and the mechanical properties are presented in Table 11.

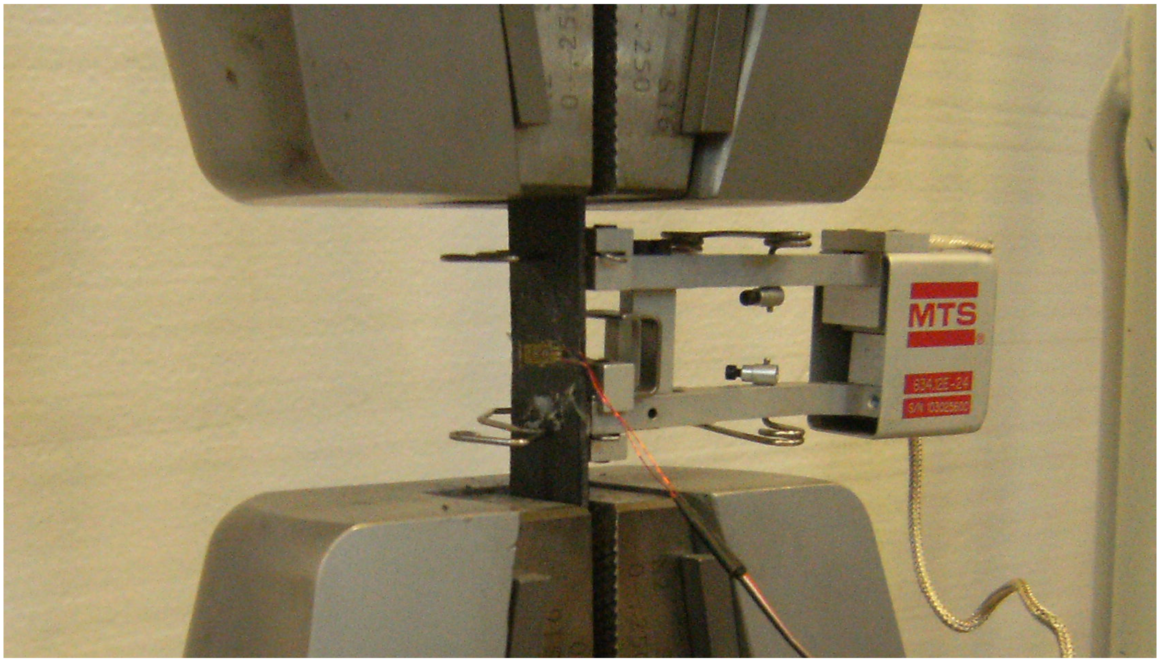

Figure 3.31: Tensile test of the CFRP

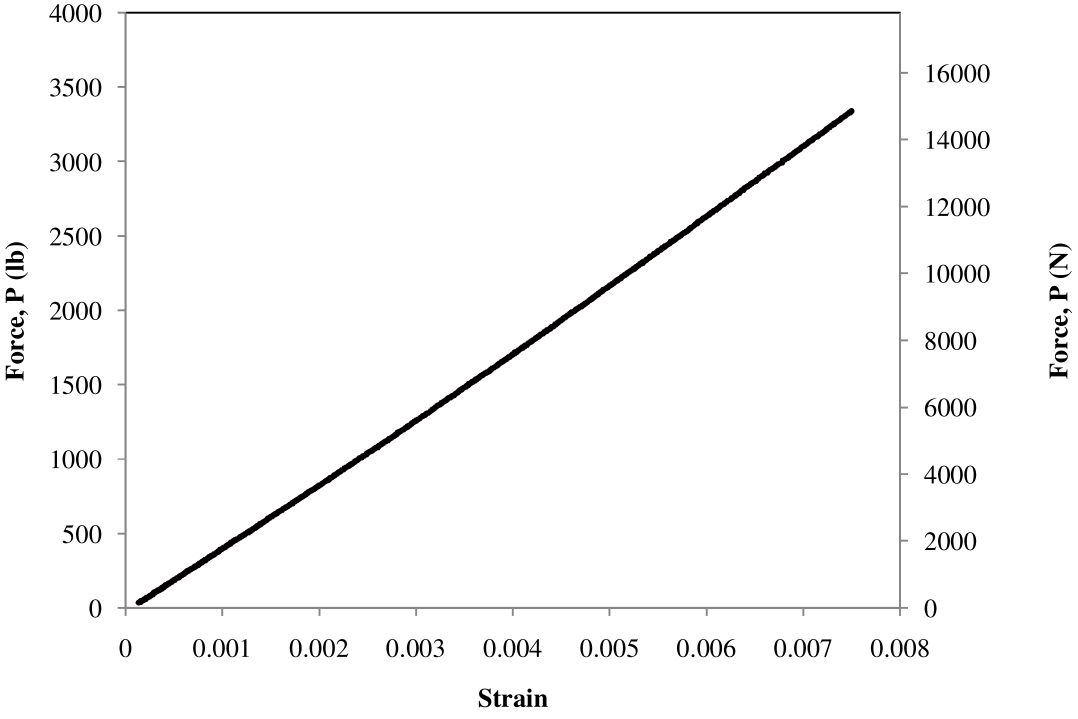

Figure 3.32: Stress-strain relationship of CFRP to P = 3339 lb (14584 N)

Table 11: Mechanical properties of CFRP

Specimen	Elastic modulus, ksi (MPa)	Standard deviation, psi (MPa)	Poisson's ratio
CFRP	14354 (98966)	396 (2733)	0.26

3.5 TEST PARAMETERS AND DATA ACQUISITION

The control slab was positioned using a combination of a pallet jack and the two cranes located in the University of New Mexico Structures Laboratory. The control slab setup can be observed in Figure 3.33. The LVDTs and the struts that support them can also be observed. In addition, the boundary conditions are shown to match the original design.

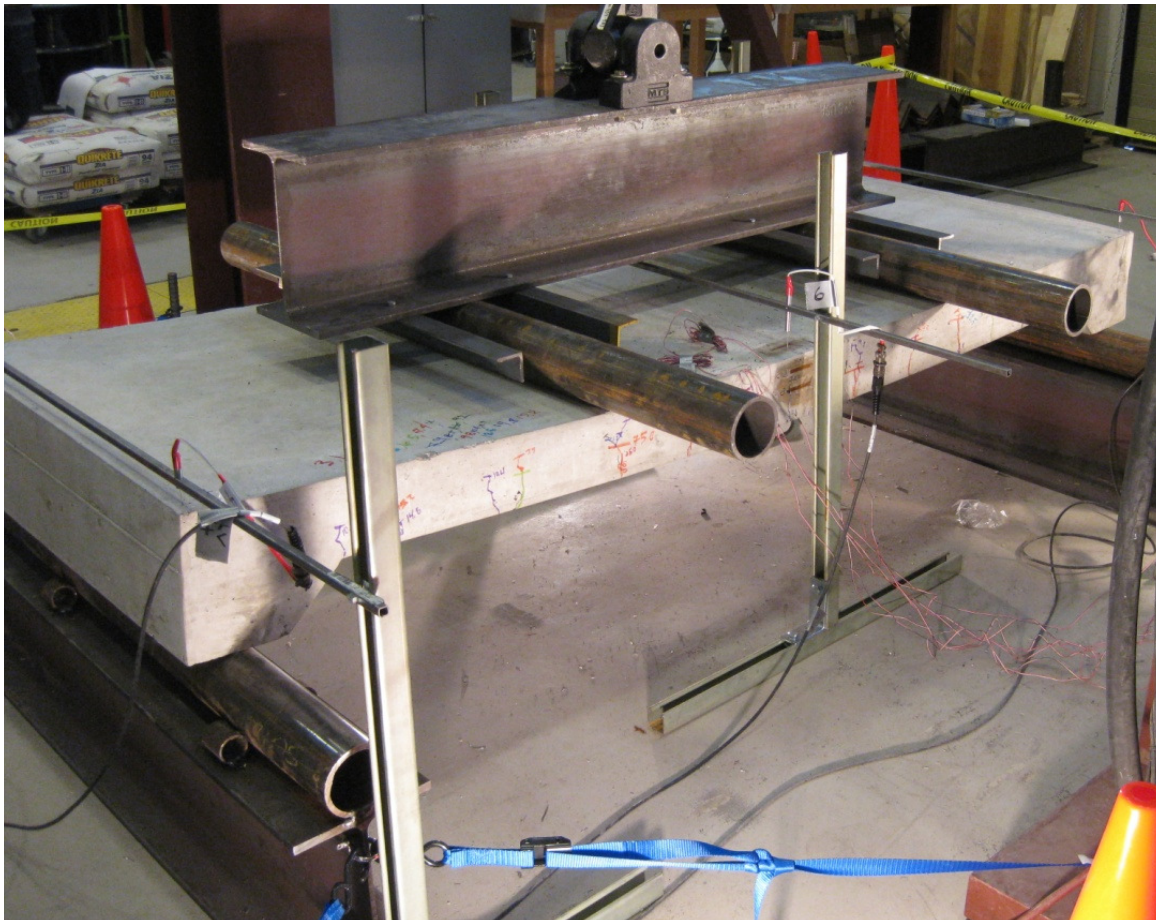

Figure 3.33: Control slab test setup

The strengthened slab was also moved into its place under the testing frame using a combination of the pallet jack and two cranes located in the University of New Mexico Structures Laboratory. As can be observed in Figure 3.34, the strengthened slab was setup in a similar manner as the control slab.

Figure 3.34: The strengthened slab prior to testing

MTS Station Manager was used to control the two tests. The tests were displacement-controlled at 1 mm/min for 19 mm. After each mm, the actuator would hold the current displacement for one minute. This time was allocated to mark cracks using permanent markers. After 19 mm of displacement, the displacement between holds was increased to 3 mm while maintaining the load rate of 1 mm/min. After 25 mm of displacement, the actuator displaced at 5 mm steps at the same load rate. The displacement between holds was increased to 10 mm after 70 mm of total displacement. After 90 mm of total displacement, the load rate was increased to 3 mm/min with 30 mm steps between holds. This rate was maintained until failure of the slabs. The data acquisition system recorded data from the seven strain gauges, six LVDTs, actuator load cell, and actuator displacement every ten seconds.

CHAPTER 4 NUMERICAL METHODS

4.1 CONTROL MODEL

The control slab was modeled using the finite element (FE) method. The FE model was developed using ANSYS 12.0 [39]. The concrete was modeled using the element type SOLID65. SOLID65 is an eight-noded element with three translation degrees of freedom (DOFs). This element was chosen because of its crushing and cracking features. This element type allows for modeling of concrete with or without reinforcing bars. The reinforcing bar was modeled using element type LINK8. This element type is a spar that is capable of developing uniaxial tension and compression. LINK8 has two nodes and each node has three translation DOFs. Figure 4.1 shows the two types of elements used in modeling the reinforced concrete slab.

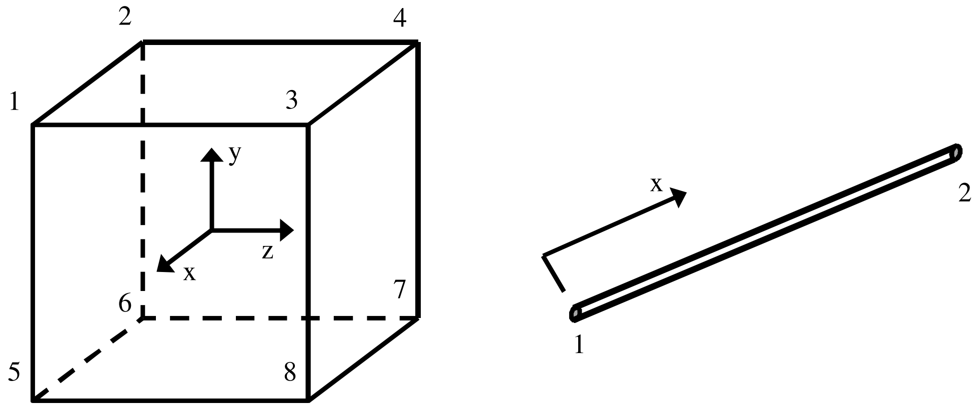

Figure 4.1: Element types SOLID65 and LINK8 [39]

SOLID65 requires the input of the shear coefficient for an open crack, shear transfer coefficient for a closed crack, uniaxial tensile cracking stress, and uniaxial crushing stress. The coefficients for shear can range between 0 for a smooth crack that exhibits no shear transfer and 1 for a rough crack which exhibits complete shear transfer.

Based on the literature, the shear coefficient for an open crack can range from 0.05 to 0.3 and the coefficient for an open crack range from 0.9 to 1 [40-45]. The open shear coefficient used in this FE model is 0.3 and the closed shear coefficient used is 0.9. Crushing of concrete was neglected due to convergence issues. Other studies have also found this to be the case [40, 44]. Other material properties needed to model the concrete elements are ultimate biaxial compressive strength (f_{cb}), ultimate compressive strength for a state of biaxial compression superimposed with hydrostatic stress state (f_1), and ultimate compressive strength for a state of uniaxial compression superimposed on a hydrostatic stress state (f_2). Since the data was unavailable, the model used relationships developed by William and Wanke to describe these properties [46]. These relationships are defined in Equation 4.1 to Equation 4.3.

$$f_{cb} = 1.2f_c^{'} \tag{4.1}$$

$$f_1 = 1.45f_c^{'} \tag{4.2}$$

$$f_2 = 1.725f_c^{'} \tag{4.3}$$

where $f_c^{'}$ is the characteristic compressive strength of the concrete.

The cracking model used in the FE model is described in Figure 4.2. T_c is a multiplier used to control the amount of tensile stress relaxation. By default, a value of $0.6 \cdot f_t$ is equal to the tensile strength of the concrete, ε_{ck} is the cracking strain calculated using the values input in the model, and R^t is the tension secant modulus which reduces to 0 as the solution converges. It is important to allow for concrete tension stress relaxation to enable model convergence.

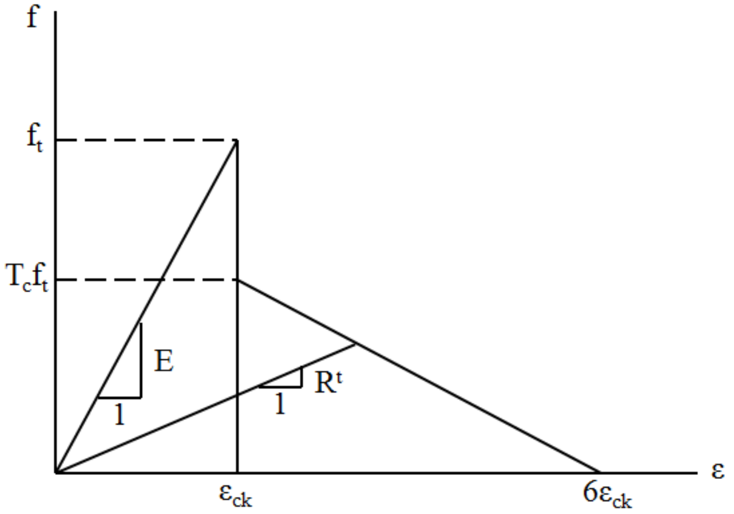

Figure 4.2: Concrete cracking definition used in the FE model

The concrete stress strain relationship was modeled using the relationship developed by Todeschini [30] as given in Equation 3.5 to Equation 3.7. The compressive strength for the NVC was used as reported in Table 5. The tensile strength of the NVC was modified from the value presented in Table 5 to $f_t = 0.5\ f_{splitting}$ to amount for the effect of restrained shrinkage that generates tension and detract from f_t [47]. The stress-strain relationship for the NVC is shown in Figure 4.3.

The reinforcing steel was modeled as multilinear elastic with an elastic modulus of 29000 ksi (200000 MPa) and a yield strength of 73.75 ksi (508.49 MPa). A cross sectional area of 0.196 in^2 (126.45 mm^2) was applied to LINK8 in the longitudinal direction and 0.11 in^2 (70.97 mm^2). The stress-strain relationship used for the reinforcing steel is shown in Figure 4.4. Including strain hardening, rather than using a linear elastic-perfectly plastic definition, is necessary for model stability and solution convergence.

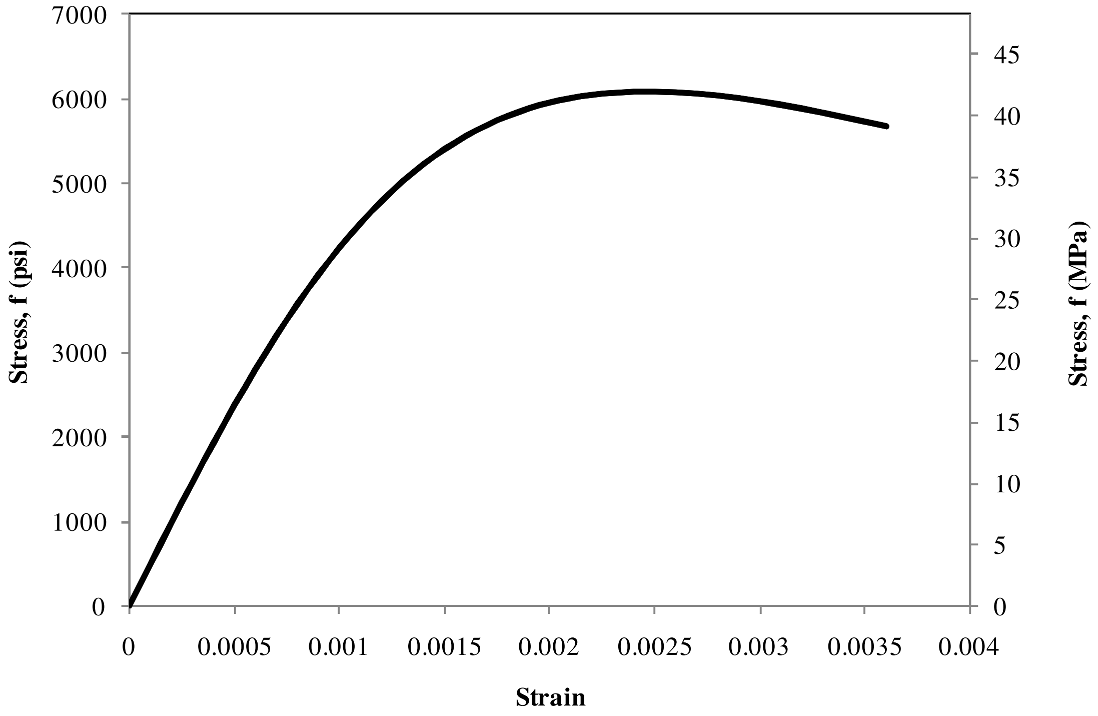

Figure 4.3: Stress-strain relationship for NVC used in the FE model

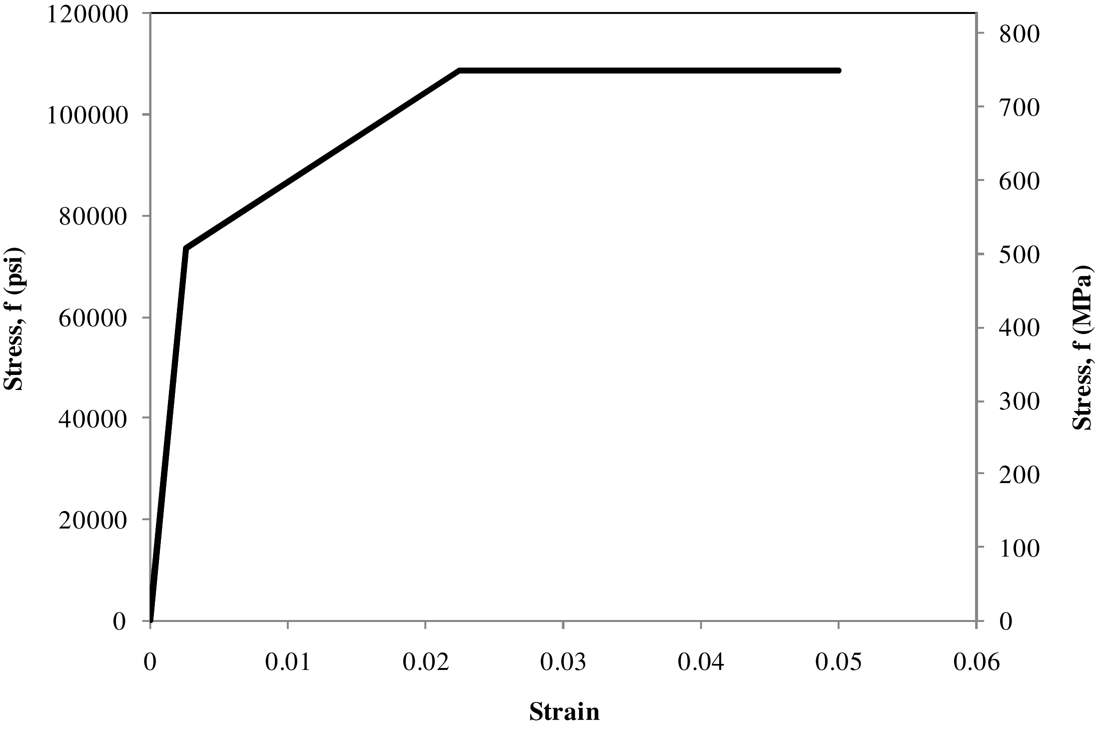

Figure 4.4: Stress-strain relationship for the reinforcing steel used in the FE model

For computational purposes, only a portion of the slab was modeled. Using proper symmetry and boundary conditions, only 1/10 of the slab was modeled. This section contains one of the bars used for flexural reinforcement and all of the transverse reinforcement. This results in a total model width of 7.2” (182.9 mm). The portion of the slab simulated in the FE model is shown in Figure 4.5. To prevent instability of the concrete at the restraints, steel blocks were modeled using SOLID65 with the same material properties as were used for the reinforcing steel without cracking or crushing capabilities. The dimensions of all of the concrete elements are 0.45” x 0.5” x 0.5” (11.43 mm x 12.7 mm x 12.7 mm). A total of 16896 elements were used in the model. The steel reinforcement, support, and simulated roller used in the model are shown in Figure 4.6.

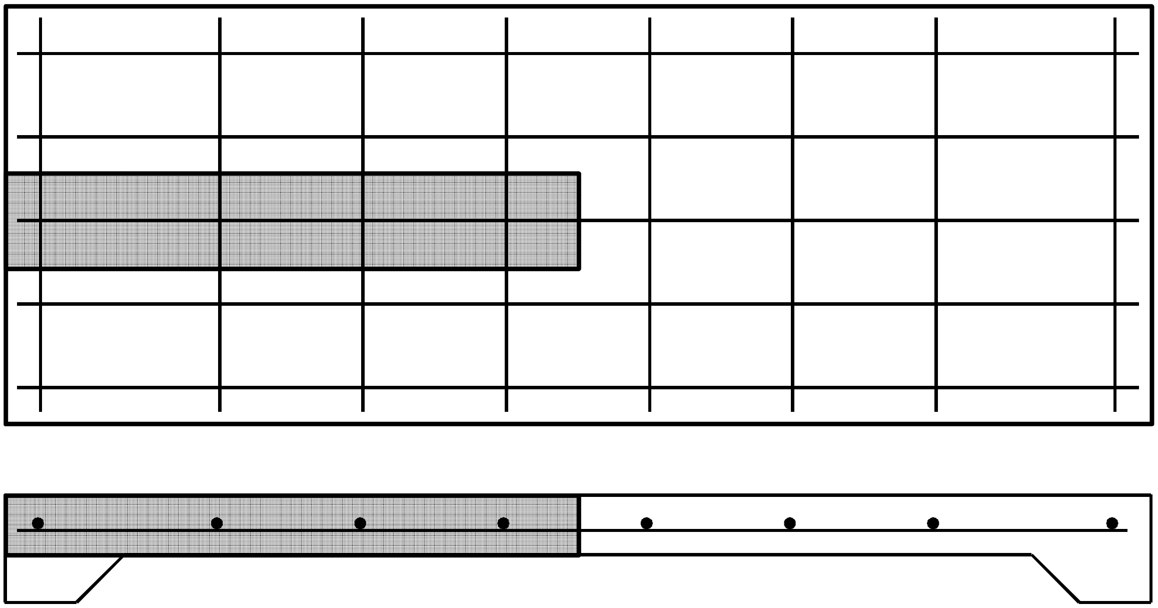

Figure 4.5: Portion of the control slab simulated in the FE model

The model was restrained at the center of the support from moving in the y-direction but was allowed to move longitudinally in the z direction. One pin was placed on the support to prevent out-of-plane movement. It can be observed in Figure 4.7 that only movement in the z-direction was allowed. Figure 4.7 also shows the geometry used in the FE analysis.

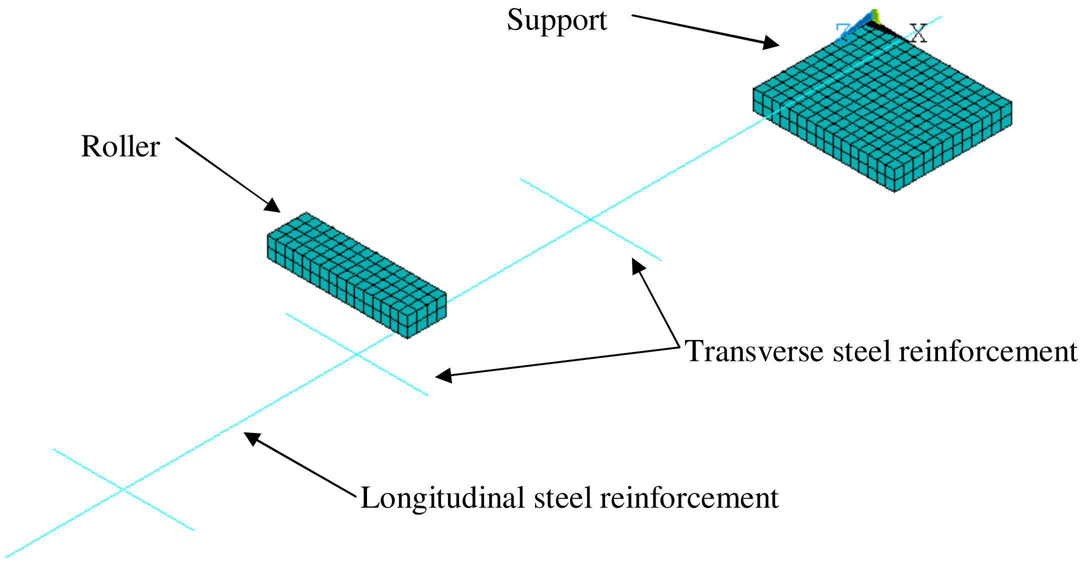

Figure 4.6: Steel detail for the control slab in the FE model

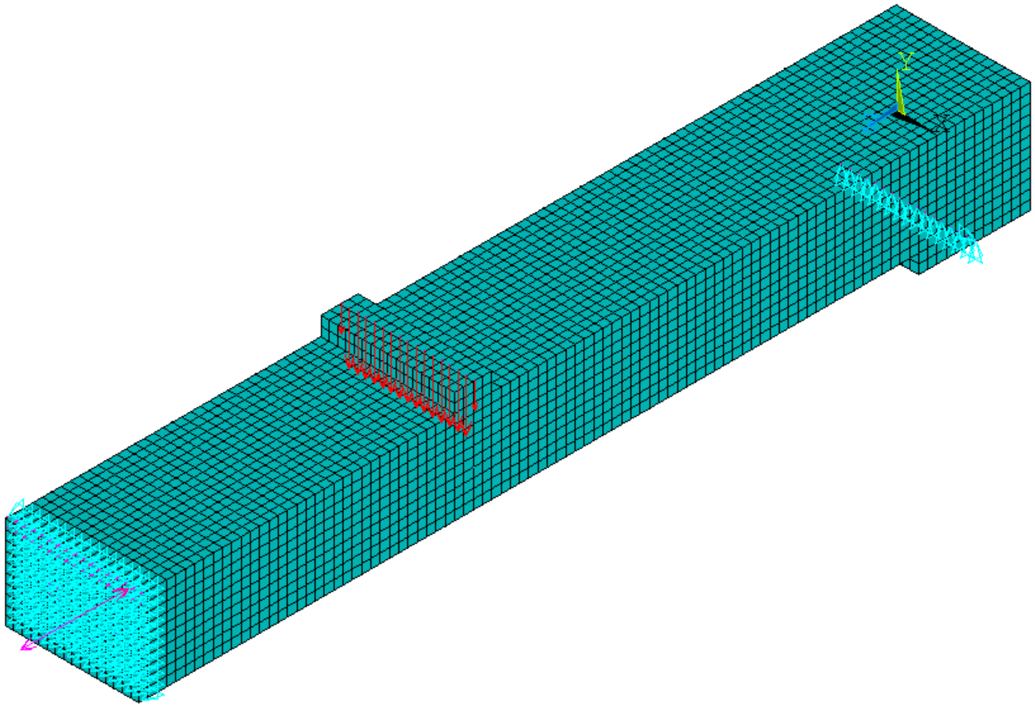

Figure 4.7: Geometry and boundary conditions for the control slab in the FE model

4.2 STRENGTHENED MODEL

The strengthened slab was modeled in a similar manner. The steel reinforcement and boundary conditions remained constant from the first model. The element type used for the CFRP was also SOLID65 with the material properties shown in Table 12. The cracking and crushing properties were not enabled for the CFRP. The UHPC was modeled using SOLID65, as with the NVC. Because of the smaller height of the UHPC, the elements were sized as 0.5" x 0.45" x 0.1" (12.7 mm x 11.43 mm x 2.54 mm). This allows for an accurate depiction of the compressive zone developed in the UHPC.

The CFRP was assumed to behave in a linear-elastic fashion using the material data defined in Table 9 and Table 11 which are based on manufacturer data and experimental testing. The stiffness of the CFRP used in the model, $E_{\text{CFRP model}}$, was modified based on work by Chen and Teng [48] using a coefficient β_w described by Equation 4.4. The stiffness is calculated as

$$E_{\text{CFRP model}} = \beta_w E \tag{4.4}$$

$$\beta_w = \sqrt{\frac{2\text{-}\, b_{frp}/b}{1+ b_{frp}/b}} \tag{4.5}$$

By using b_{frp} as 24" (609.6 mm) and b as 36" (914.4 mm), β_w was found to be 0.894. The UHPC was modeled to consider cracking but not crushing, as with the NVC. The shear transfer coefficients remained at 0.3 for open cracks and 0.9 for closed cracks. The stress-strain relationship was based on the model proposed by Graybeal as described in Section 2.2 and is shown in Figure 4.8. The constants a and b used corresponded to the values found for steam treating UHPC found in Table 1. The stress-strain relationship for the CFRP was based on experimental testing of CFRP strips as described in Section 3.4. Table 12 lists the material properties used in each of the models.

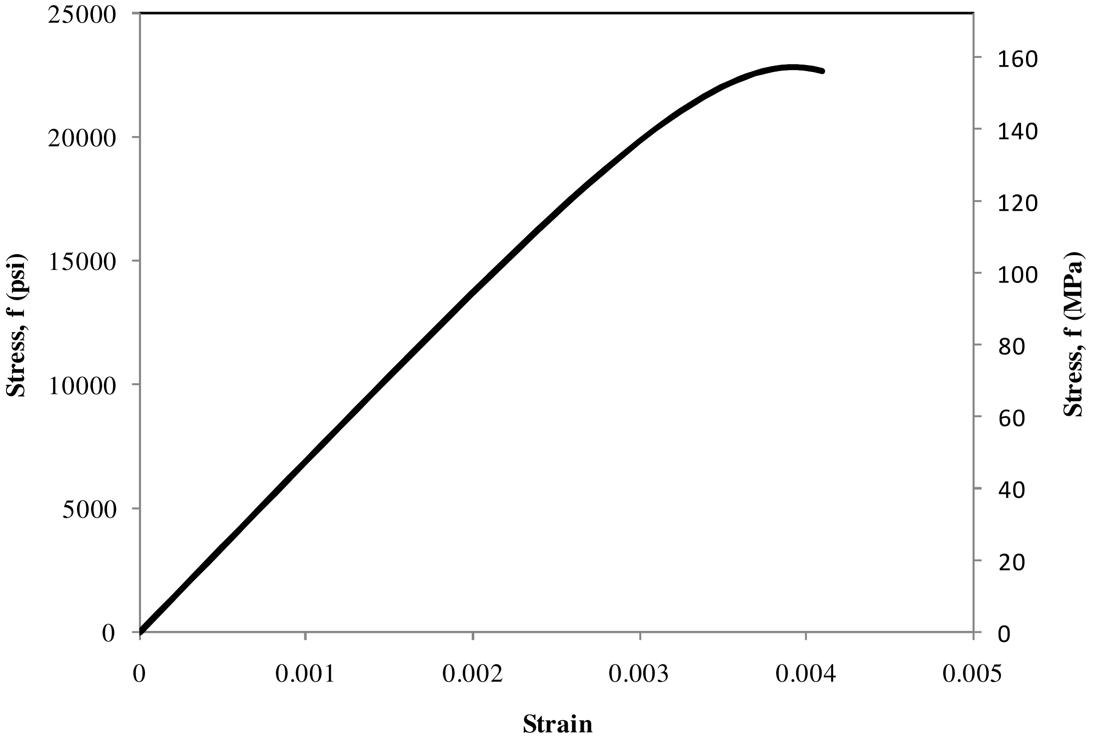

Figure 4.8: Stress-strain relationship used for modeling the UHPC

The geometry and boundary conditions for the strengthened slab are shown in Figure 4.9 and the profile of the FE model of the strengthened slab is shown in Figure 4.10. Different colors are used to differentiate the different materials used in the FE model. The CFRP was assumed to cover the entire area between the UHPC and NVC. The cross sectional area of the CFRP in relation to the total cross sectional area of the strengthened slab remained constant between the model and the actual strengthened slab. The CFRP elements measured 0.5” x 0.45” x 0.03” (12.7 mm x 11.43 mm x 0.762 mm). A total of 27648 elements were used in this model.

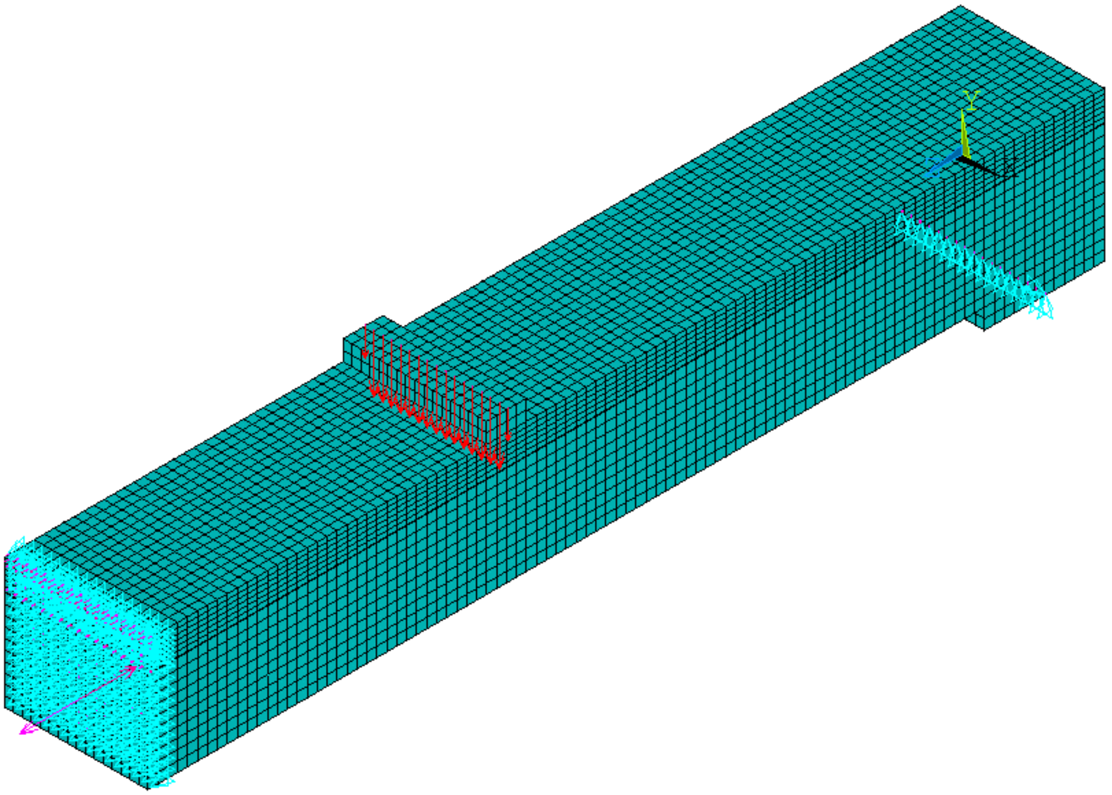

Figure 4.9: FE model of the strengthened slab

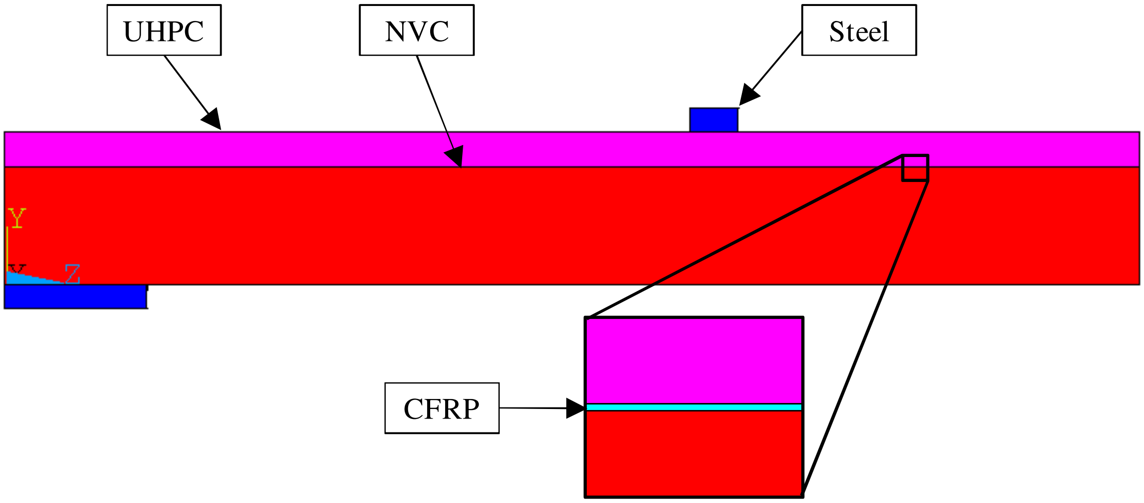

Figure 4.10: Profile for the strengthened slab geometry used in the FE model

Table 12: Material properties used to define FE modeling

Component	Steel	Concrete	CFRP	UHPC
Element type	LINK8/SOLID65	SOLID65	SOLID65	SOLID65
Open shear coefficient	-	0.25	-	0.25
Closed shear coefficient	-	0.9	-	0.9
Tensile strength, ksi (MPa)	108.5 (748)	0.225 (1.55)	390 (2689)	0.565 (3.90)
Compressive strength, ksi (MPa)	108.5 (748)	6.75 (46.5)	-	22.25 (153.4)
Elastic modulus, ksi (GPa)	29000 (200)	4803 (33.1)	12838 (88.5)	6935 (47.8)
Poisson's ratio	0.30	0.15	0.26	0.20
Ultimate failure strain	-	-0.0035	0.0304	-0.0041

4.3 ALTERNATIVE MODELS

In addition to the FE models of the strengthened slab and control slab, an FE model was created to compare the control slab to a similar model with 6.5" (165.1 mm) total depth. The remaining boundary conditions remained constant from the control slab model. The geometry used in this model is shown in Figure 4.11.

A parametric study was also performed to investigate the effect of overlay strength on the performance of the strengthening system. Instead of using UHPC as the compressive overlay, NVC was used. The two types NVC used were the typical NVC used for the concrete substrate and a high performance concrete (HPC) with a characteristic compressive strength of 14500 psi (100 MPa). These FE models used the same geometry and boundary conditions as shown in Figure 4.9.

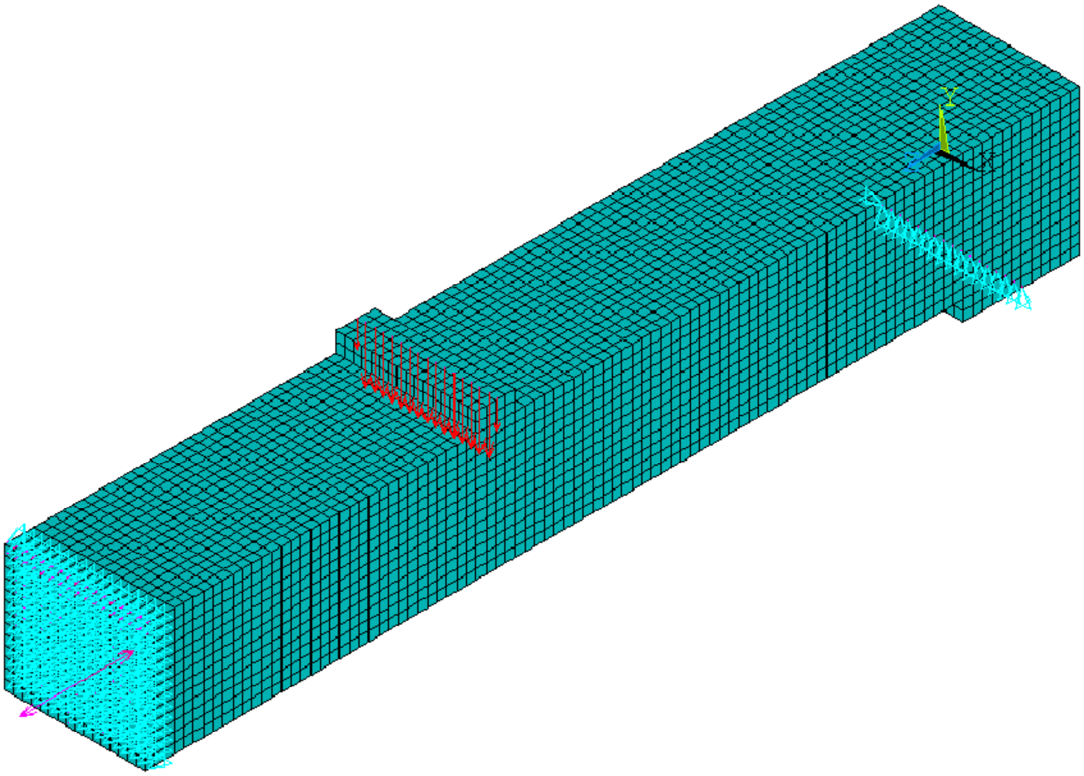

Figure 4.11: FE model of the modified control with 6.5” depth

4.4 SOLUTION PARAMETERS

The FE simulation of the control slab was performed and calibrated against the load deflection curve of the experimental results. This was achieved using a large displacement static analysis where the geometrical deformation was included for every substep in the calculation of the stresses and strains. Using automatic time stepping, the force applied ranged from 1 lb (4.45 N) to 928 lb (4128 N) at each solution step. These forces correspond to the forces that would be applied if the entire slab was modeled. A displacement convergence criterion was utilized using the Newton-Rhapson method. Using a force convergence criterion disallowed model convergence, as reported in the literature [40]. This displacement convergence criterion was kept to a minimum to produce accurate results. As increased load was applied, the tolerance value was also increased to allow for model convergence.

The strengthened slab used an increased applied force with each substep ranging from 1 lb (4.45 N) to 2400 lb (10676 N). These forces correspond to the total forces that would be applied over the entire strengthened slab. The strengthened slab FE model also made use of the displacement criterion for convergence. The reference value for the displacement criterion was taken from the experimental results and the tolerance of the value was kept as small as possible to accurately model the strengthened slab.

The alternative model with the increased depth used an increased applied load of 30400 lb (135226 N) to compensate for the increased capacity that resulted from the increased depth. The alternative models that were strengthened with NVC in place of UHPC followed the same solution parameters as the strengthened slab model.

CHAPTER 5 RESULTS AND DISCUSSION

This chapter analyzes the data extracted from the two full scale structural tests as well as the finite element analyses. Each is presented individually and then the findings are compared and discussed.

5.1 CONTROL SLAB

5.1.1 EXPERIMENTAL RESULTS

The full scale structural test was performed in a successful manner. The slab developed cracks as the loading increased between the two rollers. There were also cracks that developed between the rollers and supports, though they never developed into full-depth cracks. Some of these cracks can be seen in Figure 5.1 along with the marking of the corresponding load. Figure 5.1 shows slab cracking at approximately 7 kips (31.1 kN) of applied force.

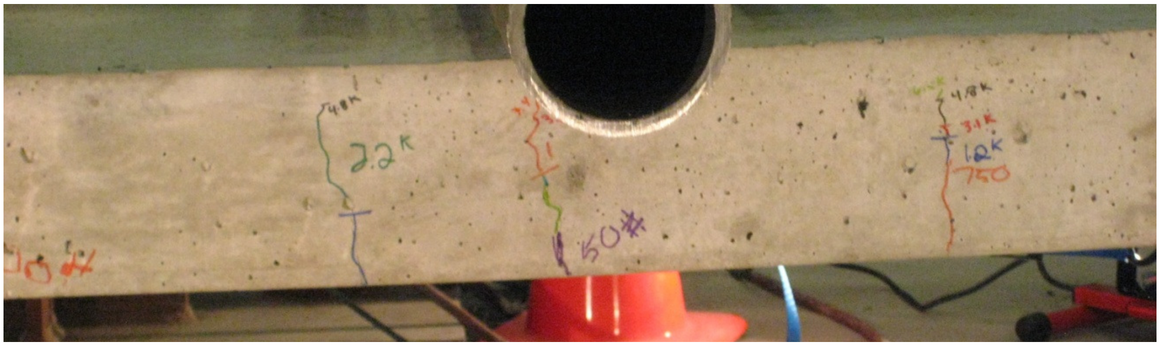

Figure 5.1: Cracks developing in the control slab

The control slab showed higher load and deflection than were originally calculated. The LVDTs had to be reset at different points during the test to continue to provide accurate readings. This major deflection is shown in Figure 5.2. The picture shown was taken prior to, but nearing, failure.

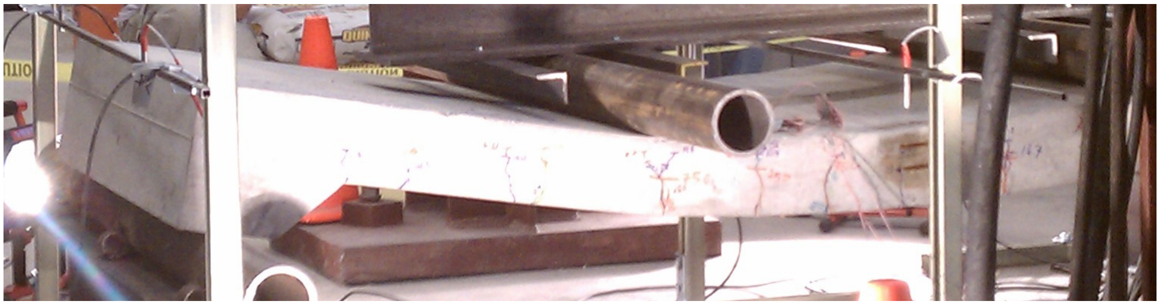

Figure 5.2: Deflection of the control slab near failure

The maximum load and corresponding displacement at failure for the control slab are presented in Table 13. The displacement from the actuator was used in all calculations for consistency between the control slab and the strengthened slab.

Table 13: Maximum load and displacement properties of the control slab

Specimen	Maximum load, lb (N)	Displacement at maximum load, in (mm)
Control Slab	18625 (82848)	3.65 (92.71)

The final failure for the control slab resulted from concrete crushing of the NVC beneath one of the loading points in the constant moment region. This crushing can be observed in Figure 5.3.

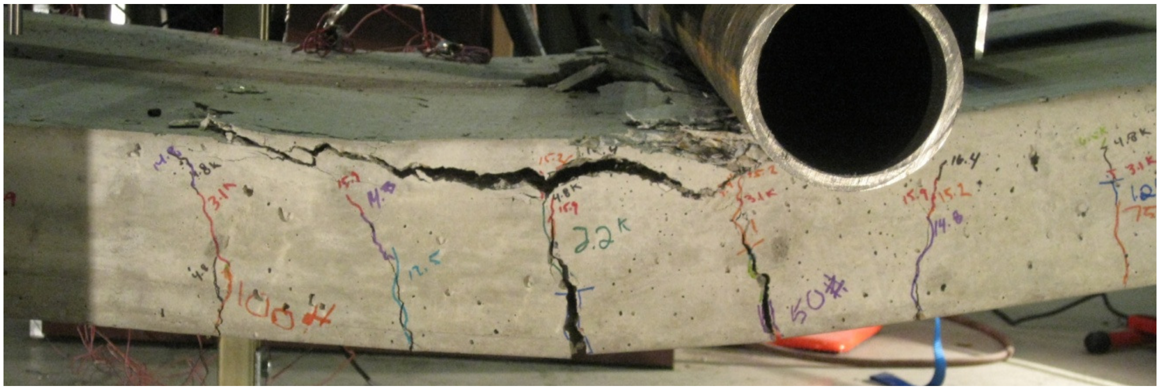

Figure 5.3: Failure due to concrete crushing in the control slab

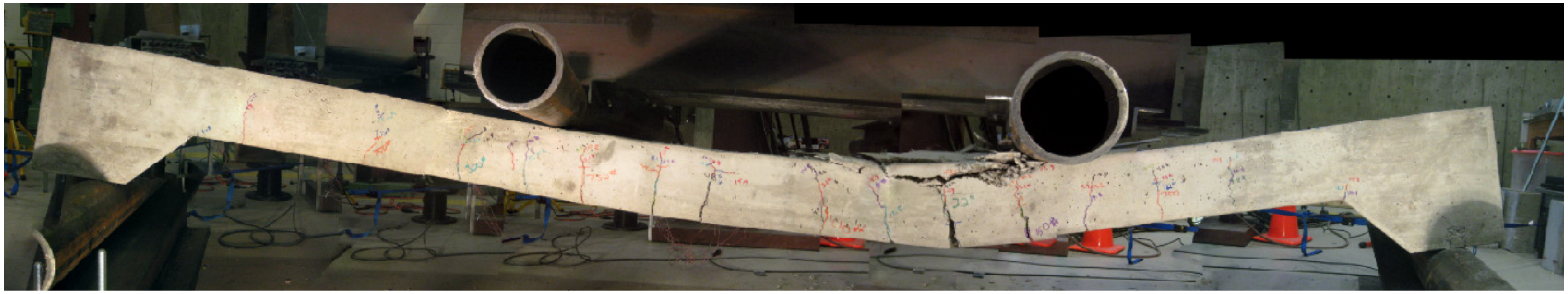

Figure 5.4: Control slab after failure

5.1.2 ANALYSIS OF THE P-Δ CURVE FOR THE CONTROL SLAB

The P-Δ curve of the control slab is shown in Figure 5.5. It can be observed that the structure behaved in a linear-elastic fashion until 0.904" (23 mm) of displacement. The corresponding force at this displacement is 14331 lb (63747 N). Up until this point, the steel was behaving elastically as can be observed in Figure 5.6. The strain gauge debonded from the rebar shortly after yield. The maximum load applied to the control slab is 62% higher than the predicted value calculated in Section 3.1.2. It is important to note that this prediction is based on the assumption of linear elastic-perfectly plastic behavior of the steel and a concrete compressive strength of 6000 psi (41 MPa). Testing of the reinforcing steel showed a higher strength in the slab due to strain hardening and compressive strength of 6749 psi (47 MPa).

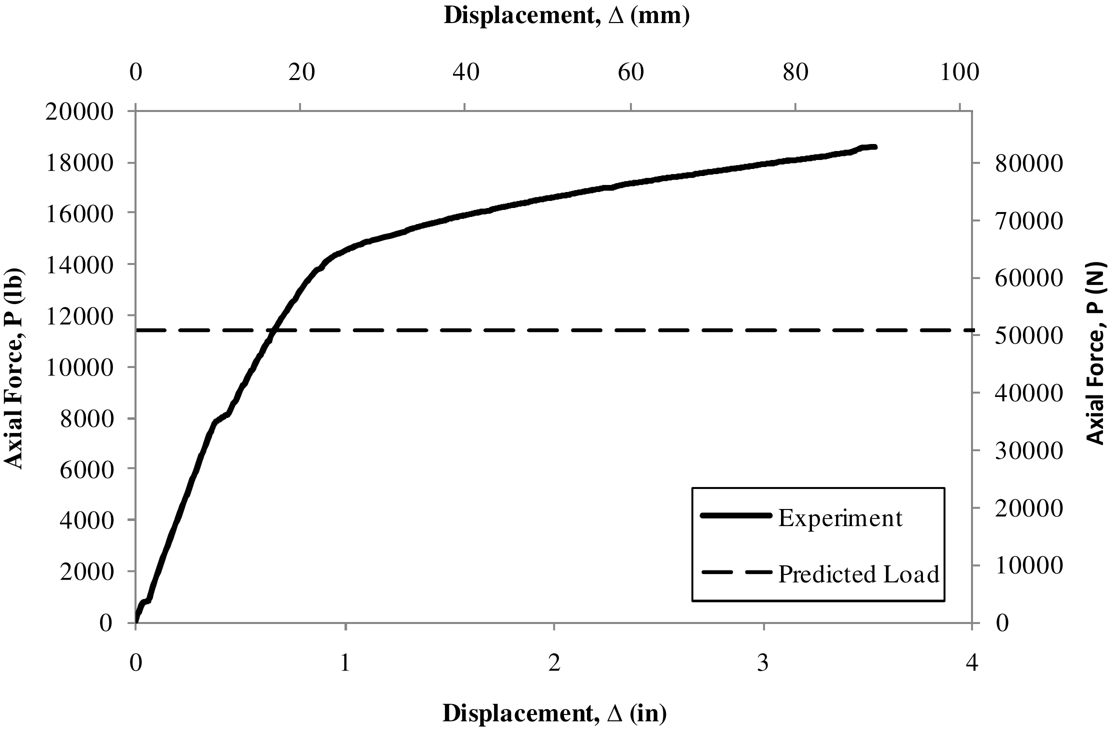

Figure 5.5: P-Δ curve for the control slab

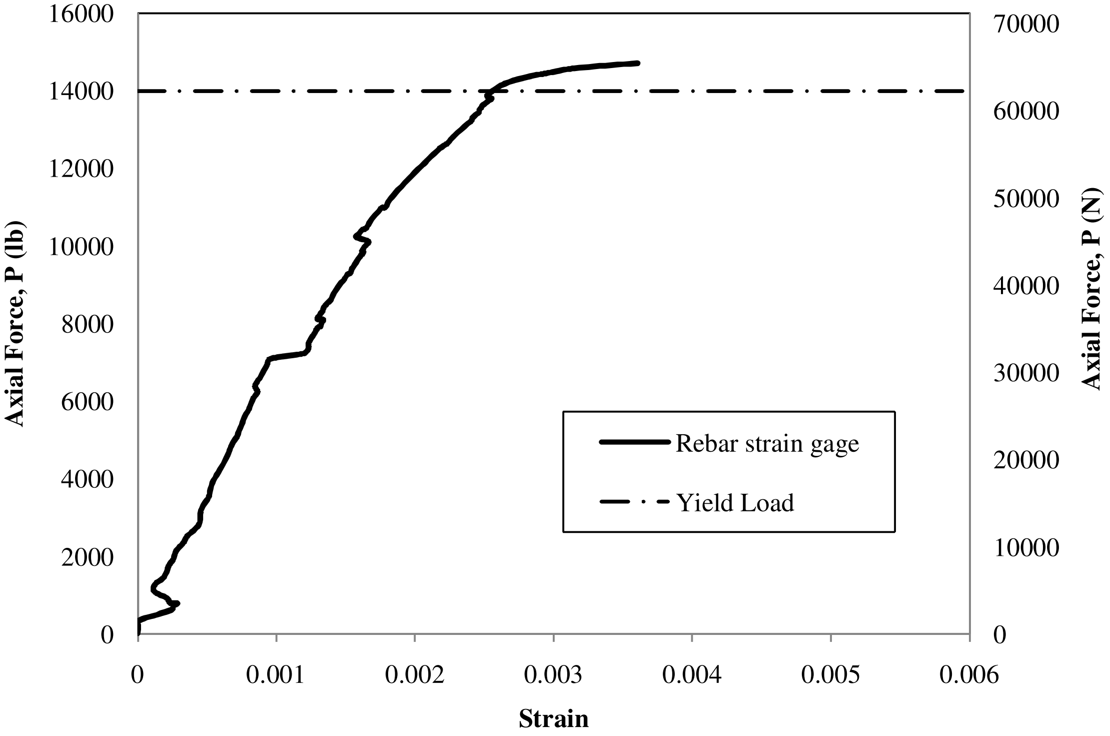

Figure 5.6: Reinforcement strain gauge data for the control slab

The stiffness of the structure, k, can be computed by using the relationship

$$P = k\Delta \tag{5.1}$$

Rearranging Equation 5.2 gives

$$k= \frac{P}{\Delta} \text{ or } k = \frac{\partial P}{\partial \Delta} \tag{5.2}$$

which is the slope of the linear-elastic region of the P-Δ curve. The slope of the P-Δ curve represents the stiffness of the control slab. This information is presented in Figure 5.7. The stiffness of the control slab is found to be 21839 lb/in (3825 N/mm) within its elastic limits.

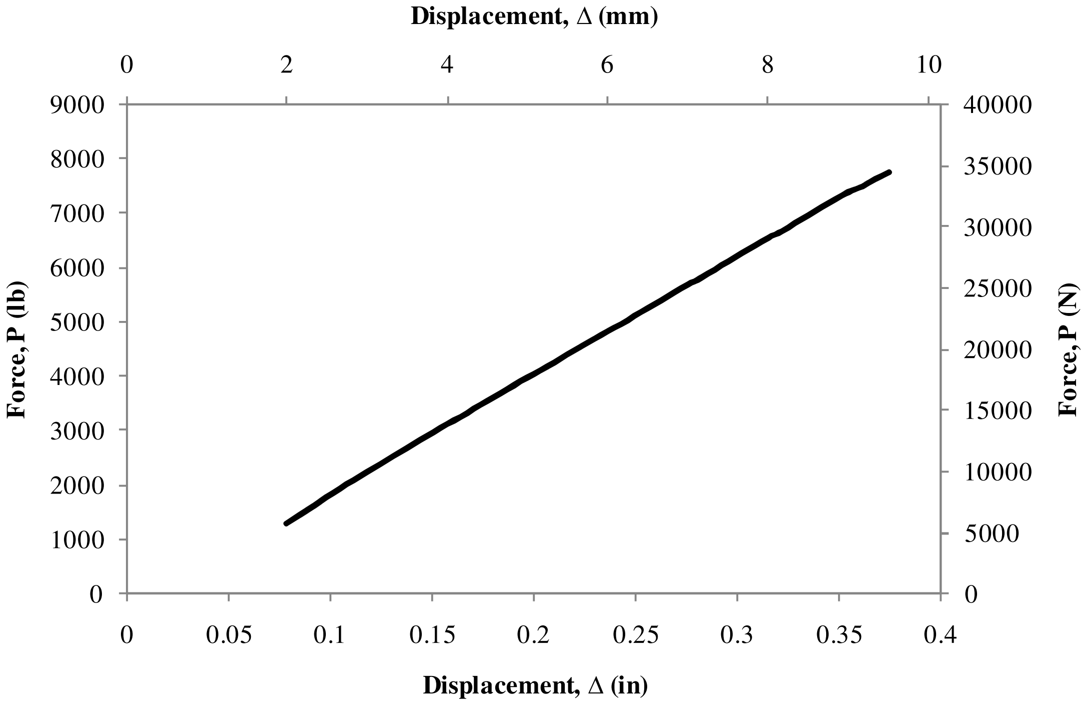

Figure 5.7: P-Δ curve to calculate the stiffness of the control slab

The toughness of the system is calculated using

$$T = \int_0^{\Delta_{P_{max}}} P(\Delta) d\Delta \qquad (5.3)$$

To evaluate this function, trapezoidal numerical integration was performed. The resulting toughness of the control slab is 51.41 kip·in (5808 kN·mm).

5.1.3 STRAIN DISTRIBUTIONS OF THE CONTROL SLAB

The strain distribution can be plotted for different critical points along the P-Δ curve. This is possible by using the strain gauge data acquired during the test. The strain distribution was analyzed every 2000 lb (8896 N) while the slab was behaving elastically and every 1000 lb (4448 N) up to failure. The points and selected strain distributions are shown in Figure 5.8. All of the analyzed strain distributions are shown in Figure 5.9 and Figure 5.10.

Observing the strain distributions, it is apparent that the neutral axis stays fairly constant around 1” (25.4 mm) until the steel started to yield. The first slight deviation from this neutral axis location can be seen at P = 14858. After cracking, the neutral axis moved up. This is due to the smaller cross section present. The neutral axis continued to move towards the top of the slab until failure. From the strain gauge data, it is found that the neutral axis at failure was 0.71” (18 mm) from the top of the slab.

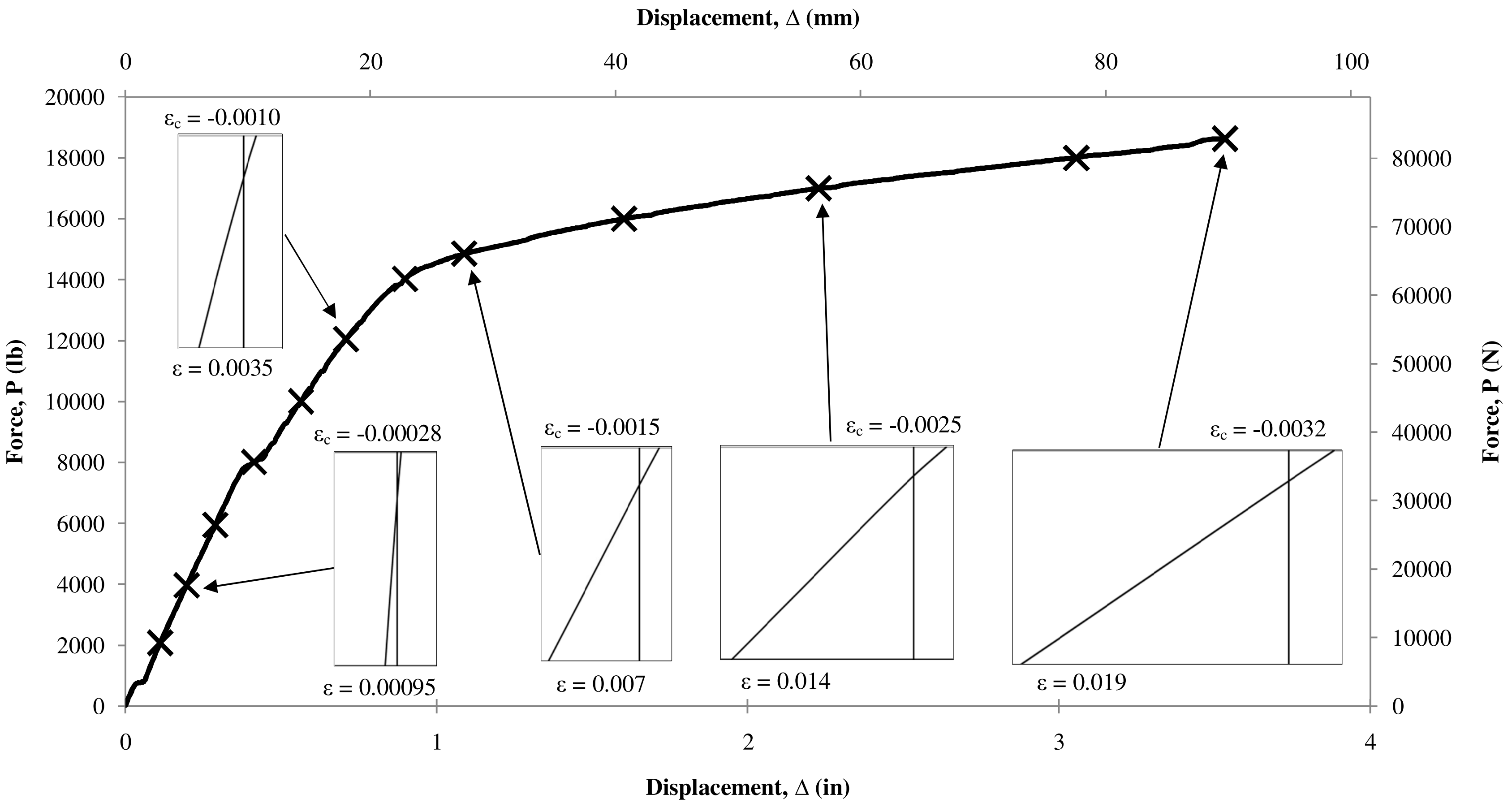

Figure 5.8: P-Δ chart for the control slab with strain distributions

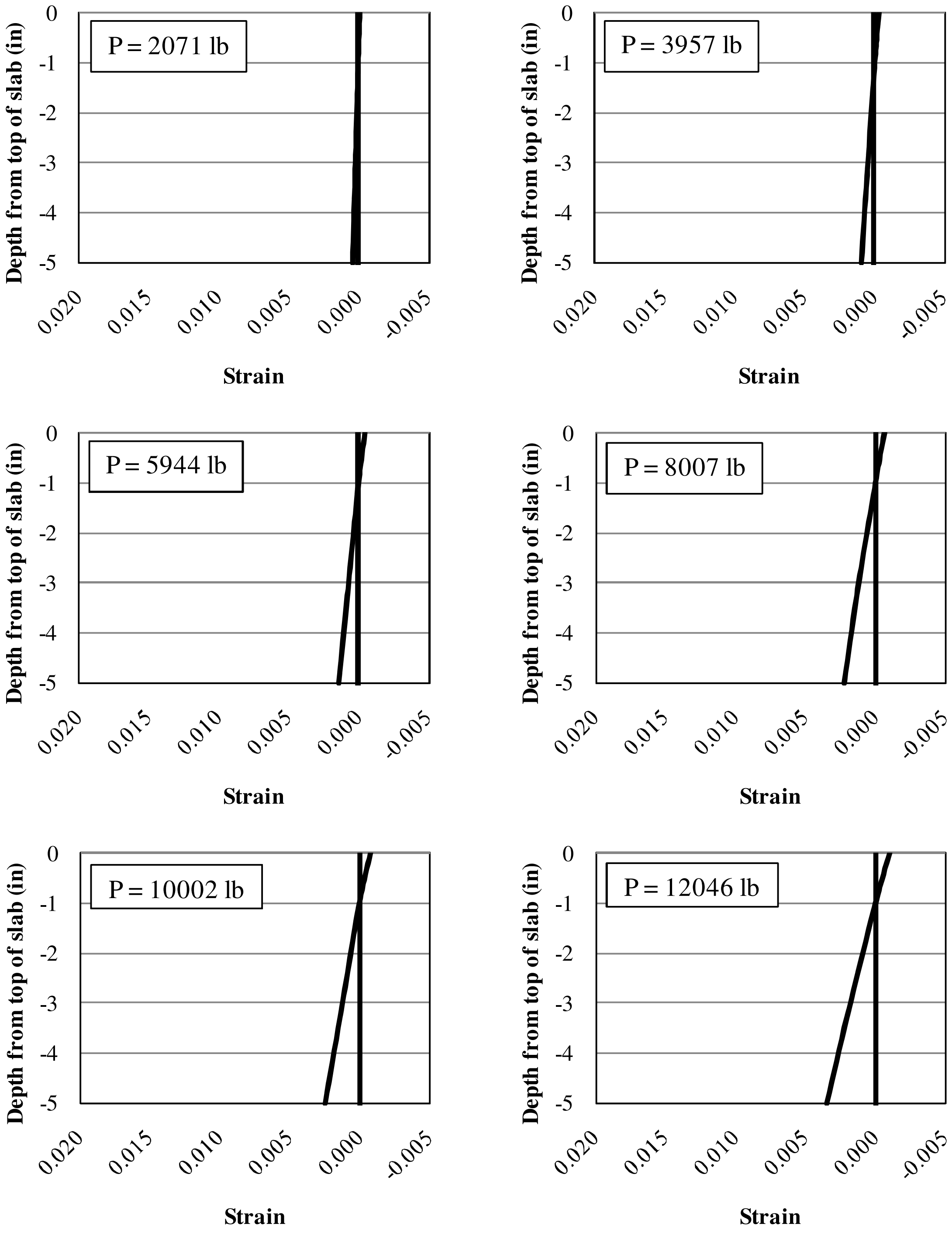

Figure 5.9: Strain distributions for the control slab (1 of 2)

(1” = 25.4 mm, 1 lb = 4.44822 N)

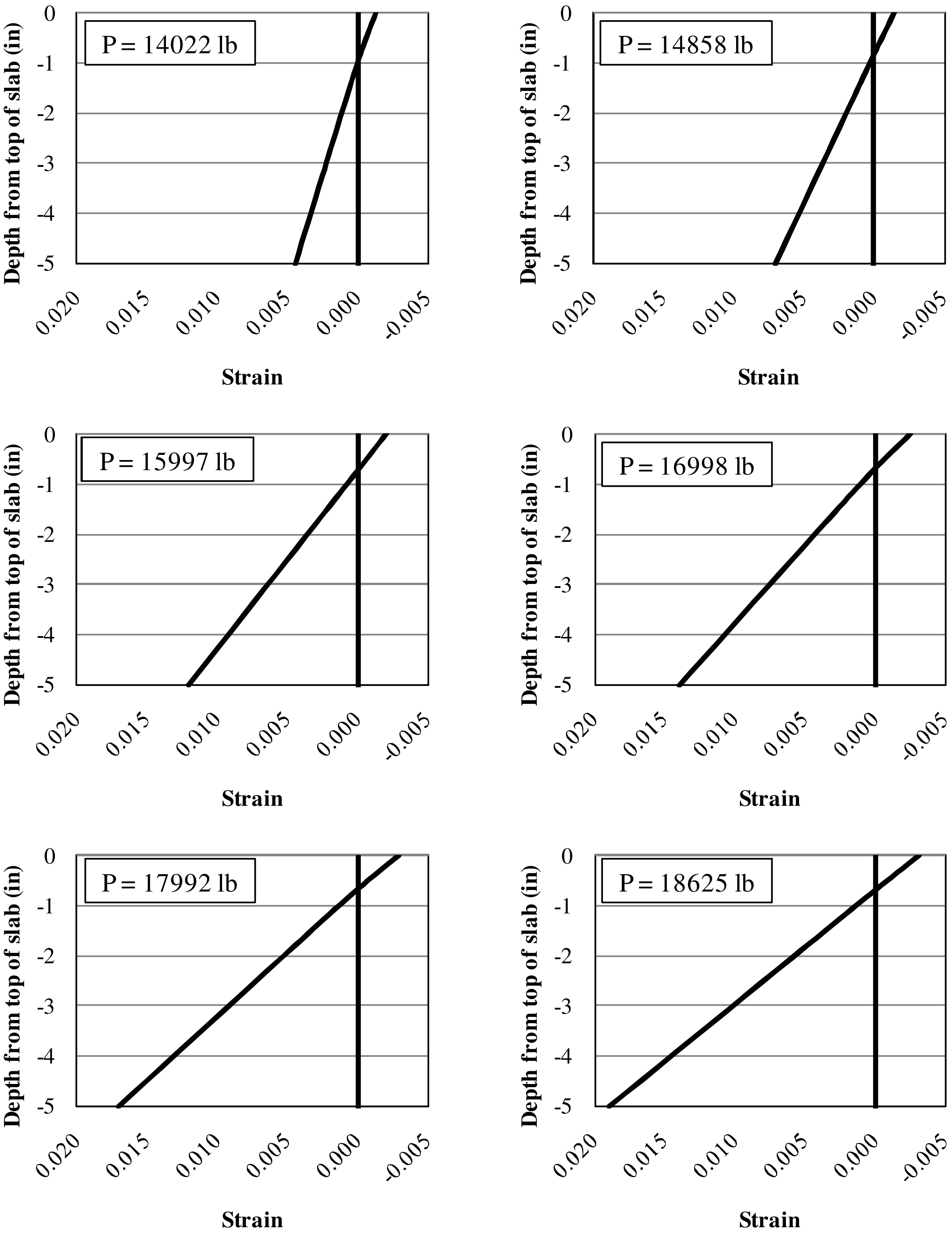

Figure 5.10: Strain distributions for the control slab (2 of 2)

(1” = 25.4 mm, 1 lb = 4.44822 N)

5.1.4 MOMENT CURVATURE OF THE CONTROL SLAB

Having a moment-curvature relationship for a structure is helpful because it allows for indirect calculation of deflection and allows for extracting the flexural rigidity of the structure. The moment-curvature relationship can be calculated using the strain diagrams developed in Section 5.1.2. Figure 5.11 shows the relationship and how the curvature can be extracted.

By using the trigonometric definition of tangent, the curvature can be solved as

$$\psi = \frac{\varepsilon_c}{c} \tag{5.4}$$

The resulting relationship is plotted in Figure 5.11.

The cracking moment, M_{cr}, is also plotted on the diagram. M_{cr} is defined as

$$M_{cr} = \frac{f_t I_g}{y_t} \tag{5.5}$$

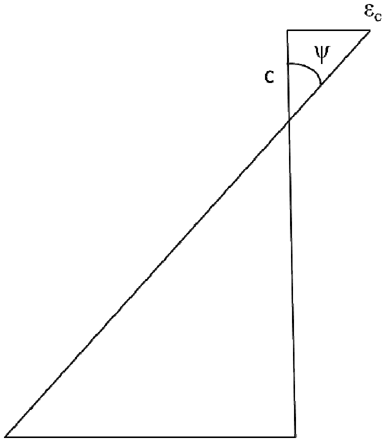

Figure 5.11: Definition of curvature based off of a strain diagram

where f_t is the tensile strength defined in Section 3.1.4, y_t is the distance between the centroid and the tension surface, and I_g is the gross moment of inertia which is calculated as

$$I_g = \frac{bh^3}{12} \tag{5.6}$$

For the control slab y_t is equal to 2.5” (63.5 mm) and, I_g is calculated to be 375 in^4 (156086784.6 mm^4). This results in a cracking moment of 70656 lb·in (7983 kN·mm).

A check of ductility of the slab is suggested by Jaeger and adopted by the Canadian Highway Bridge Design Code [49] to describe the significance of FRP on the ductility of strengthened RC structures

$$J = \frac{M_u \psi_u}{M_s \psi_s} > 4 \tag{5.7}$$

where M_u and ψ_u are the bending moment and curvature, respectively, at the ultimate load applied to the slab and M_s and ψ_s are the moment and curvature, respectively, at a service load where $\varepsilon_c = 0.001$. Obtaining values from Figure 5.12, the ductility of the control slab is found to be 7.24. Since this value is greater than 4, the control slab is considered ductile.

The flexural rigidity, EI, can be taken as the slope of the moment-curvature diagram. If the structure’s modulus of elasticity is taken as constant, the structure’s instantaneous moment of inertia can be solved for.

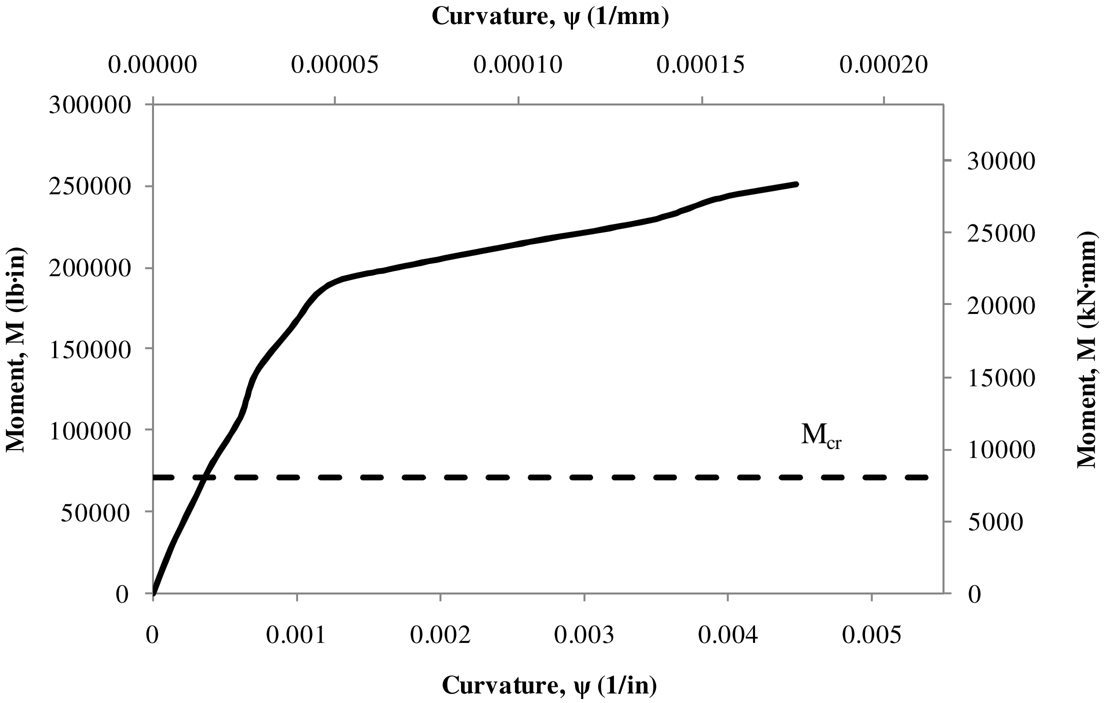

Figure 5.12: Moment-curvature of the control slab

5.2 STRENGTHENED SLAB

5.2.1 EXPERIMENTAL RESULTS

Initial observations during the test showed that the strengthened slab was more stiff than the control slab. Major yielding of the strengthened slab did not begin until above the maximum load of the control slab, which was 18625 lb (82848 N) as reported in Table 13. Far fewer cracks were present at initial loadings when compared to the control slab. Figure 5.13 shows the cracking of the control slab at approximately 10 kips (44.5 kN).

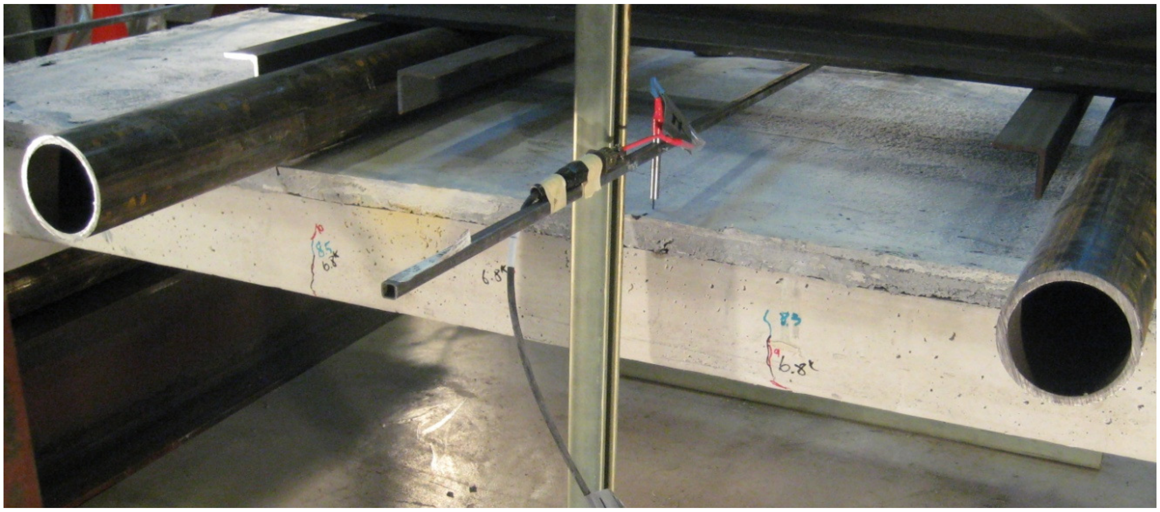

Figure 5.13: Cracking in the strengthened slab at 10 kips (44.5 kN)

As the test progressed, the slab showed consequential major loading points. One major point occurred at approximately 23250 lb (103421 N) where the CFRP began to debond from the NVC substrate outside of the rollers.

Furthermore, the UHPC began to debond from the slab between the rollers. This difference can be seen when comparing Figure 5.14 and Figure 5.15. This was not a sudden debonding, rather, the UHPC slowly lifted away from the NVC substrate.

Figure 5.14: Strengthened slab prior to UHPC debonding

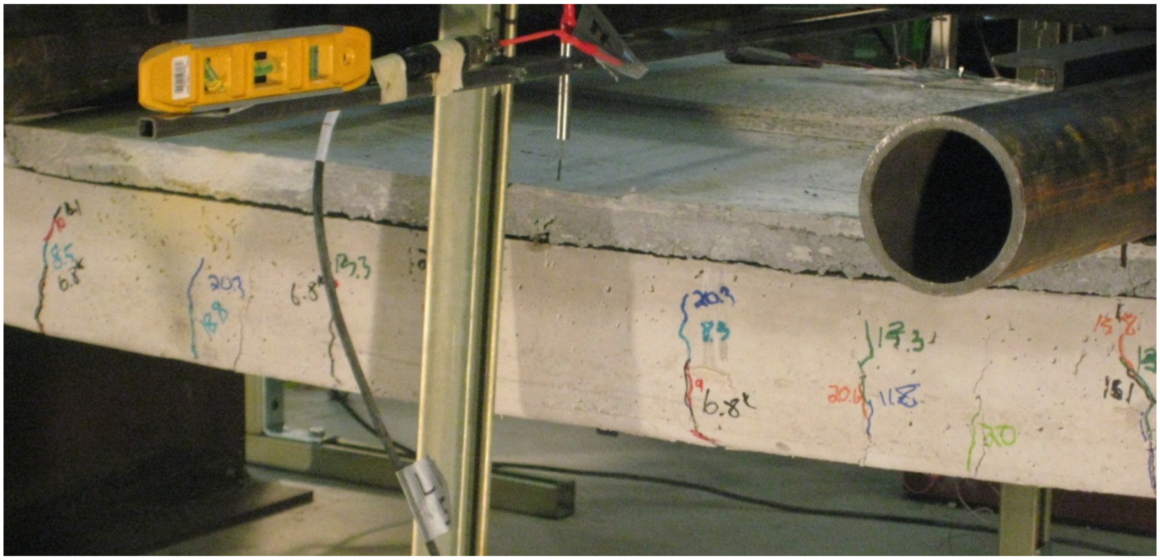

Figure 5.15: Strengthened slab after UHPC debonding

Flexural cracks were evident in the slab, as is observed in Figure 5.16. These flexural cracks did not continue to the top of the NVC slab. This is because the strains at the top of the slab never reached the tensile strain at which the concrete would crack.

This indicates that, between the rollers, a bond existed between the NVC slab and the CFRP.

Figure 5.16: Flexural cracking of the strengthened concrete slab

Horizontal shear failure of the UHPC overlay occurred at the outside of the outmost shear-friction reinforcement. This failure occurred at 26145 lb (116299 N) on one side and at 26263 lb (116824 N) on the other side. Figure 5.17 and Figure 5.18 show this UHPC overlay debonding. Because this debonding occurred at the support locations, it did not affect the slab's flexural capacity and the strengthened slab continued carrying load.

The test was stopped because the edge of the I-beam which was applying downward force to the rollers began touching the UHPC. The slab still appeared capable of taking additional load beyond its measured deflection of 4.4" (112.3 mm). After the testing commenced, it was found that the CFRP debonded from the NVC substrate as shown in Figure 5.19. The profile of the strengthened slab after failure is shown in

Figure 5.21. The UHPC and the underlying NVC appeared to remain bonded to the NVC substrate because of the shear-friction reinforcement located 24" (609.6 mm) from the longitudinal ends of the slab. It can be concluded that, to this distance, the CFRP, UHPC, NVC, and reinforcing steel acted as a composite. Figure 5.17 shows that the area between this intermediate shear-friction reinforcement remained as a single component prior to the shear failure.

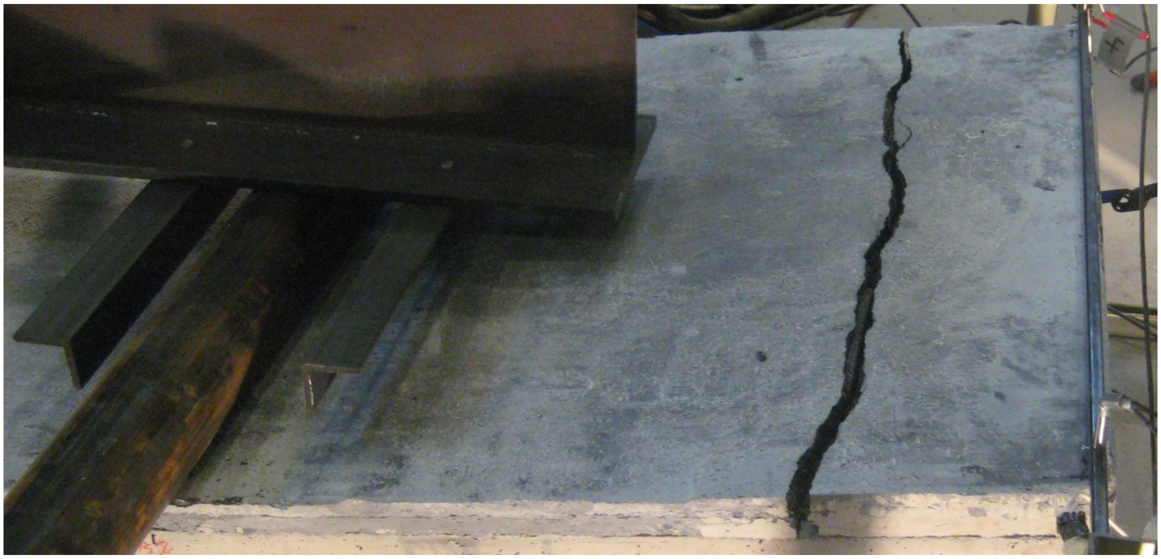

Figure 5.17: Horizontal shear failure of the UHPC overlay outside of the shear-friction reinforcement (plan)

Figure 5.18: Horizontal shear failure of the UHPC outside of the shear- friction reinforcement (profile)

Figure 5.19: Debonding of the CFRP from the NVC substrate

The maximum load and corresponding maximum displacement for the strengthened slab are given in Table 14. The maximum load and the corresponding displacement experienced by the strengthened slab are both greater than the respective quantities experienced by the control slab.

Table 14: Maximum load and displacement properties of the strengthened slab

Specimen	Maximum load, lb (N)	Displacement at maximum load, in (mm)
Strengthened Slab	26263 (116824)	4.4 (112.3)

Figure 5.20: Profile of the strengthened slab at failure

5.2.2 ANALYSIS OF THE P-Δ CURVE FOR THE STRENGTHENED SLAB

The P-Δ curve for the strengthened slab is shown in Figure 5.21. The maximum load in the experiment was 3.7% higher than the predicted load calculated in Section 3.2.1.

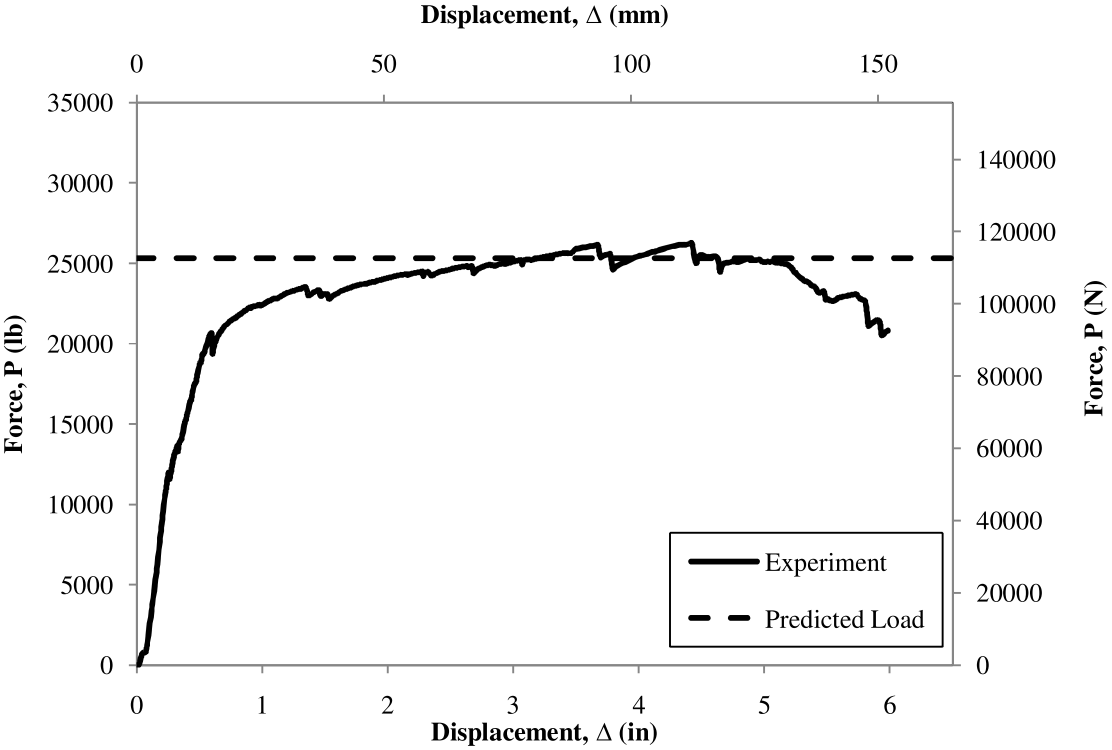

Figure 5.21: P-Δ curve for the strengthened slab

At 20658 lb (91891 N), the steel reinforcement began to yield and the slab experienced flexural cracking. The slab lost capacity due to cracking and the load dropped to 19388 lb (86242 N). Furthermore, the slab continued carrying higher load until it reached a load of 23440 lb (104266 N) when the NVC underneath one of the rollers experienced a flexural failure and cracked. The slab experienced a decrease in capacity and dropped to 22997 lb (102296 N). Shortly afterwards, the capacity increased to 23325 lb (103755 N) and the UHPC began to separate from the NVC slab as observed in Figure 5.15. This caused the load to drop to 22984 lb (102237 N). The strengthened slab continued to carry further load and cracking in the UHPC was first noticed at 24374 lb (108421 N). This cracking dropped the capacity to 24277 lb (107989 N). The strengthened slab continued to assume further load, although with slight flexural cracks, until it reached 26145 lb (116299 N) the first horizontal shear separation of the UHPC occurred, as observed in Figure 5.17. This drop changed the capacity to 25393 lb (112954 N). Soon after this horizontal shear separation, the UHPC buckled down to the NVC slab. Comparison of the UHPC buckling can be found in Figure 5.23 and Figure 5.22. This caused a further capacity decrease to 24683 lb (109795 N). The slab remained stable and increased in capacity until an applied load of 26263 lb (116824 N) caused the UHPC to fail in shear on the opposite side of the slab, as shown in Figure 5.18. Displacement continued to increase at a near constant load carrying capacity until 5.2" (130.8 mm) of actuator displacement was reached. At this point, the load began to decrease from 25000 lb (111206 N) to 23170 lb (103065 N). This decrease may be explainable due to the lateral movement of the shear-friction reinforcement due to the failure of the Sika AnchorFix-2 adhesive. The capacity of the slab began to increase to 23276 lb (103537 N) when shear failure occurred in the NVC as shown in Figure 5.24. This caused the capacity to drop to 21118 lb (93938 N) and soon after to 20533 lb (91335 N). Capacity increased marginally to 20825 lb (92634 N) before the test was stopped. The total P-Δ curve is shown in Figure 5.26 with annotations of the different failures experienced.

The actuator force that would have caused shear failure of the NVC slab was calculated in Section 3.1.2 is plotted against the P-Δ curve of the strengthened slab in Figure 5.26.

Figure 5.22: UHPC and NVC slab prior to buckling

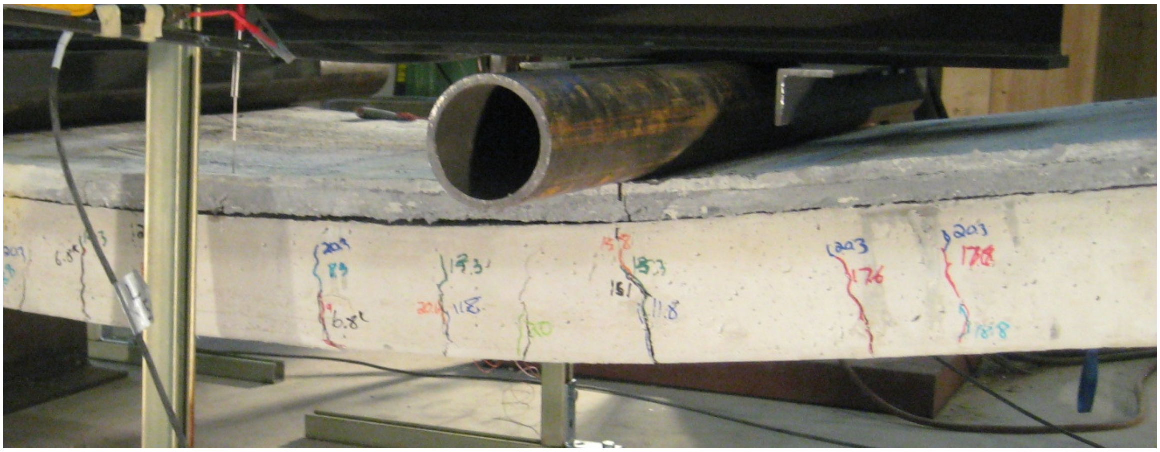

Figure 5.23: UHPC and NVC slab after buckling

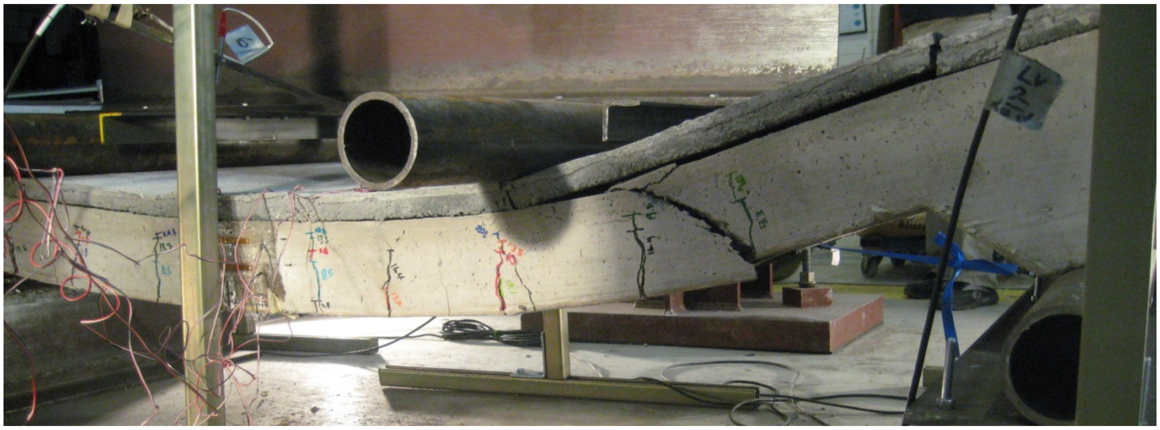

Figure 5.24: Shear failure in the NVC

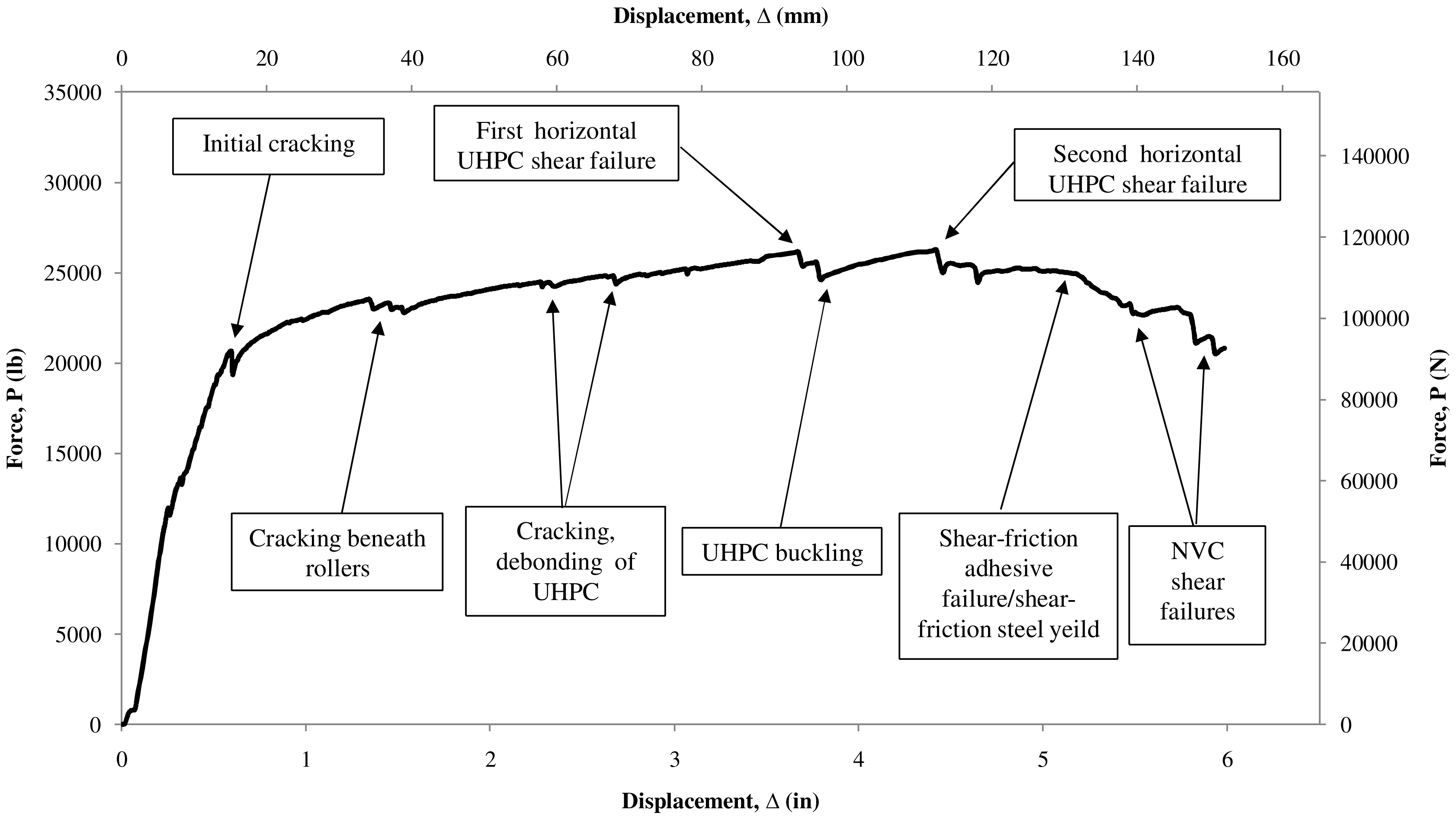

Figure 5.25: Annotated P-Δ curve for the strengthened slab

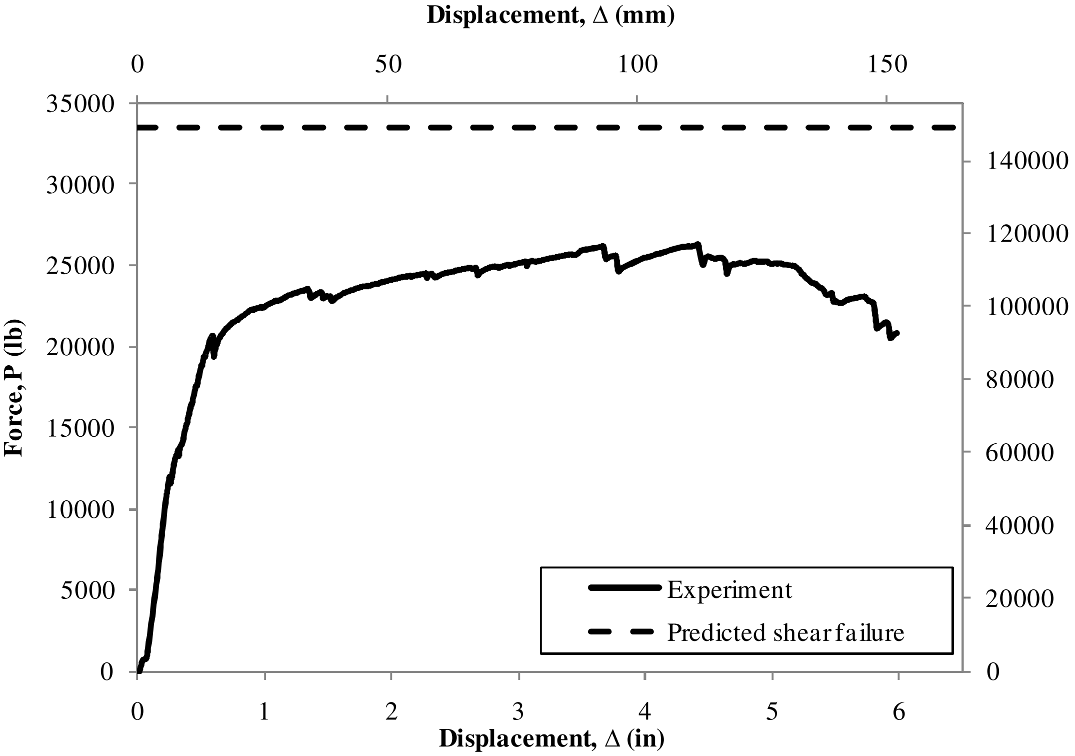

Figure 5.26: Experimental P-Δ curve of the control slab compared to the shear capacity of the NVC substrate

The stiffness of the strengthened slab can be determined using the procedure explained in Section 5.1.2, specifically using Equation 5.2. The slope of the initial portion of the P-Δ curve as shown in Figure 5.27 is found to be 64867 lb/in (11360 N/mm). This is the stiffness of the strengthened slab which is about three times that of the control slab.

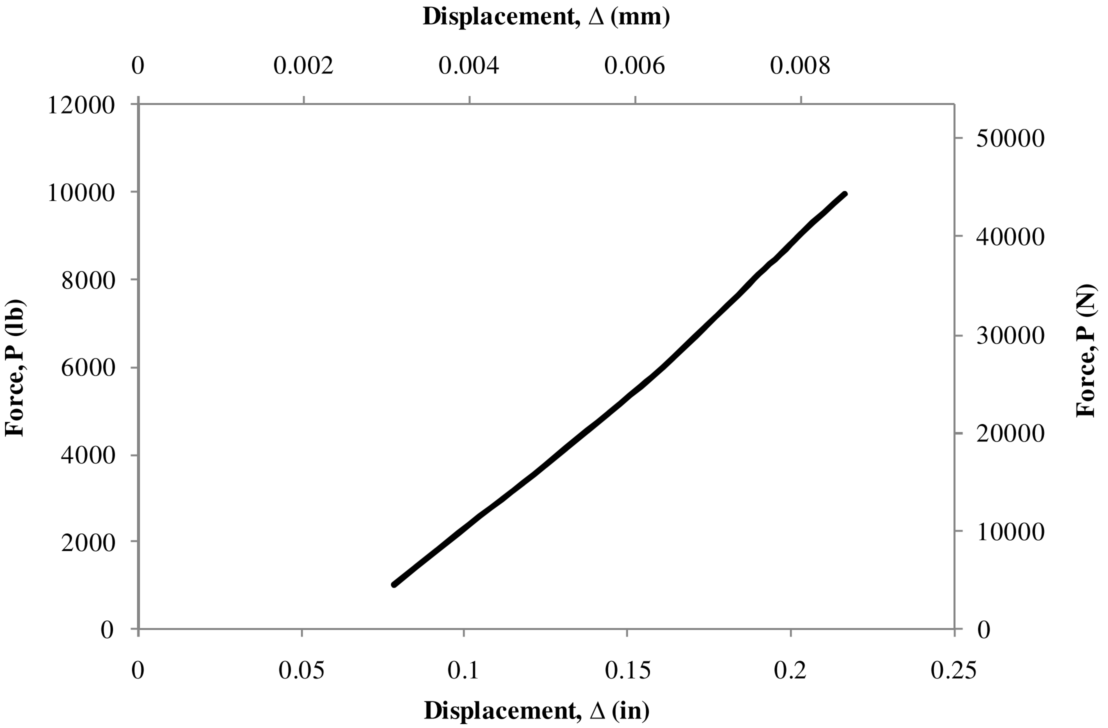

Figure 5.27: Stiffness of the strengthened slab

The ductility of the strengthened slab can be determined using the methods presented in Section 5.1.2, specifically using Equation 5.3. The toughness of the strengthened slab was found to be 137.33 kip·in (15516 kN·mm) which is nearly three times that of the control slab.

5.2.3 STRAIN DISTRIBUTIONS OF THE STRENGTHENED SLAB

The strain distributions for the strengthened slab can be calculated based on the strain gauge data acquired from the test. The main area of interest was the strain on the CFRP. The strain measurement on the CFRP was critical, as it would verify the system hypothesis that the CFRP sheets stayed in tension during the test and up to failure.

The points analyzed for strain distribution are shown in Figure 5.29, along with select distributions. Because of strain gauge delamination, not all sections were analyzed fully. The two strain gauges that remained active during the entire test were the gauge on top of the UHPC and on top of the CFRP. The assumed distance between the strain gauge on top of the CFRP and the strain gauge on top of the UHPC is taken as the height of the UHPC, which was 1.5” (38.1 mm). The corresponding strain distributions are shown in Figure 5.29 to Figure 5.32.

Because of the stiffness of the strengthened slab, the strain distribution until 14020 lb (62364 N) was very small. It can be observed that the neutral axis extended into the UHPC which caused the CFRP to be in tension. The neutral axis reached its maximum height in the UHPC right before the first horizontal UHPC shear failure occurred. After the first horizontal shear failure in the UHPC, the neutral axis lowered. Though it was lowered, the neutral axis was contained in the UHPC until the loading was stopped. This verifies the hypothesis earlier that the UHPC was the only portion of the strengthened slab in compression at its ultimate capacity and that the CFRP installed at the top of the slab would be in tension.

It can be observed that the strain at the top of the UHPC remained between -0.0011 and -0.0016 for the portion of the test where yielding occurred. This is markedly different than the strain in the CFRP which ranged from 0.0016 to 0.0002. This relatively constant strain in the UHPC in comparison to the decreasing amount of strain in the CFRP is due to debonding issues.

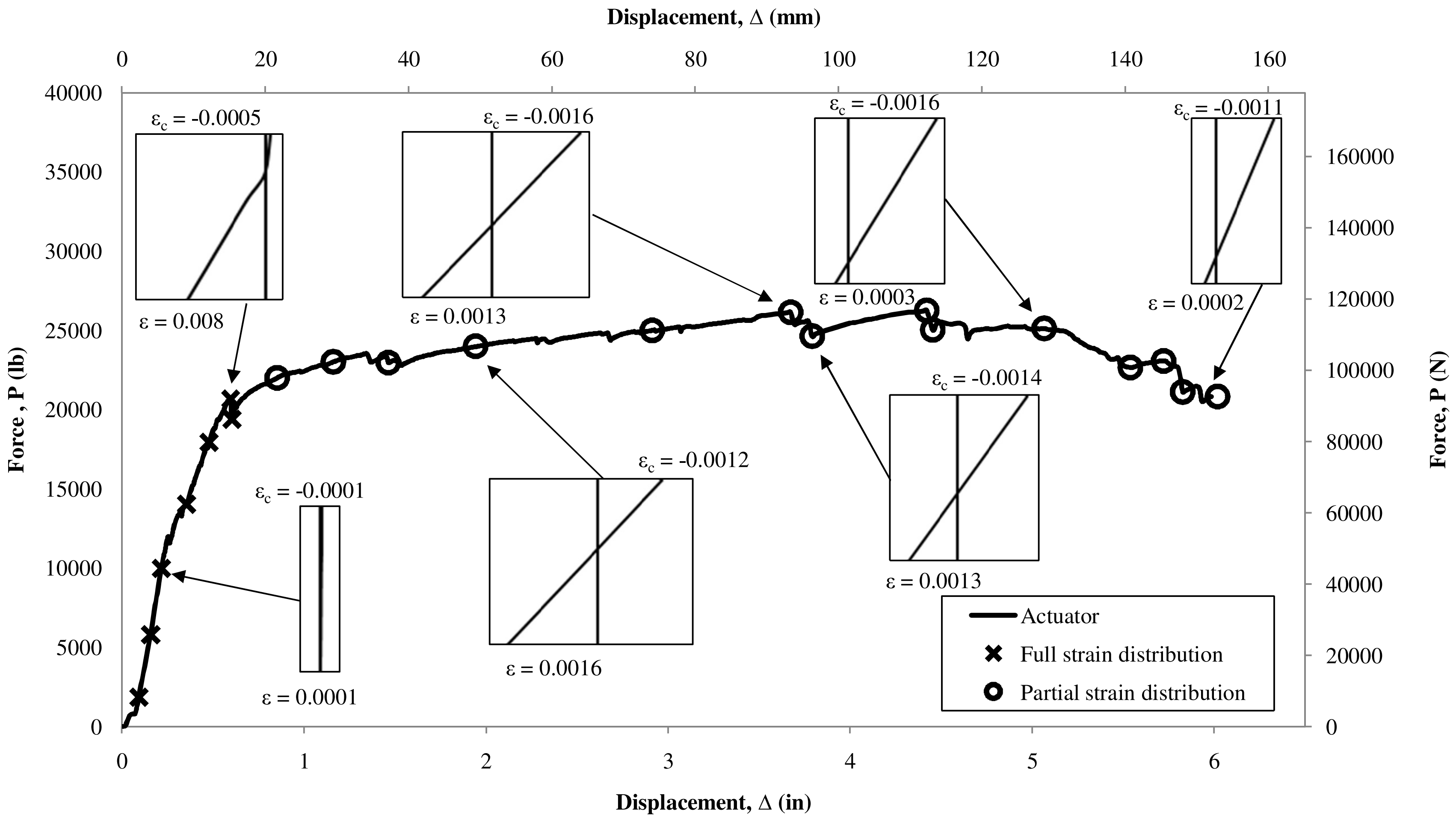

Figure 5.28: P-Δ curve for the strengthened slab with strain distributions

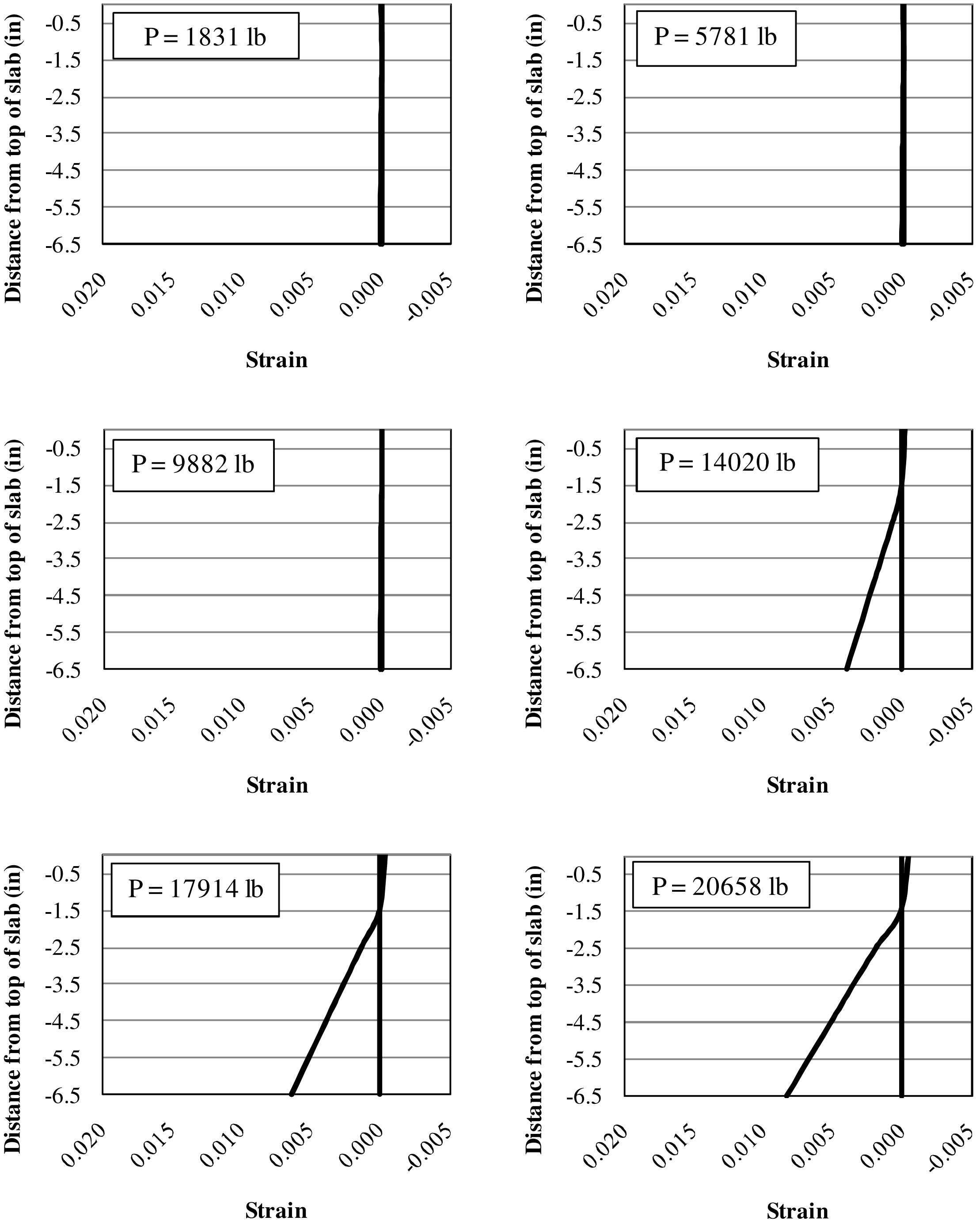

Figure 5.29: Strain distributions for the strengthened slab (1 of 4)

(1” = 25.4 mm, 1 lb = 4.45 N)

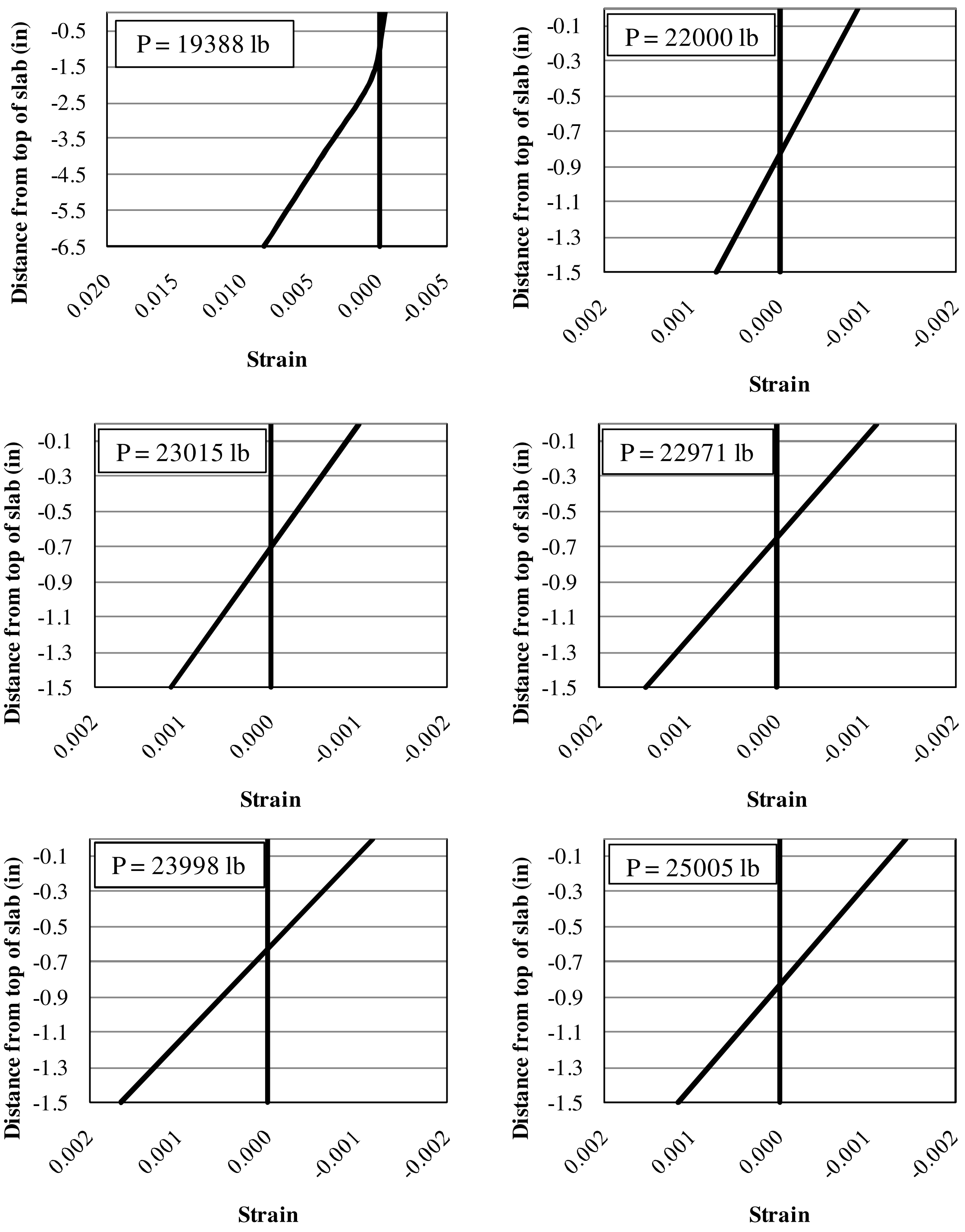

Figure 5.30: Strain distributions for the strengthened slab (2 of 4)

(1” = 25.4 mm, 1 lb = 4.45 N)

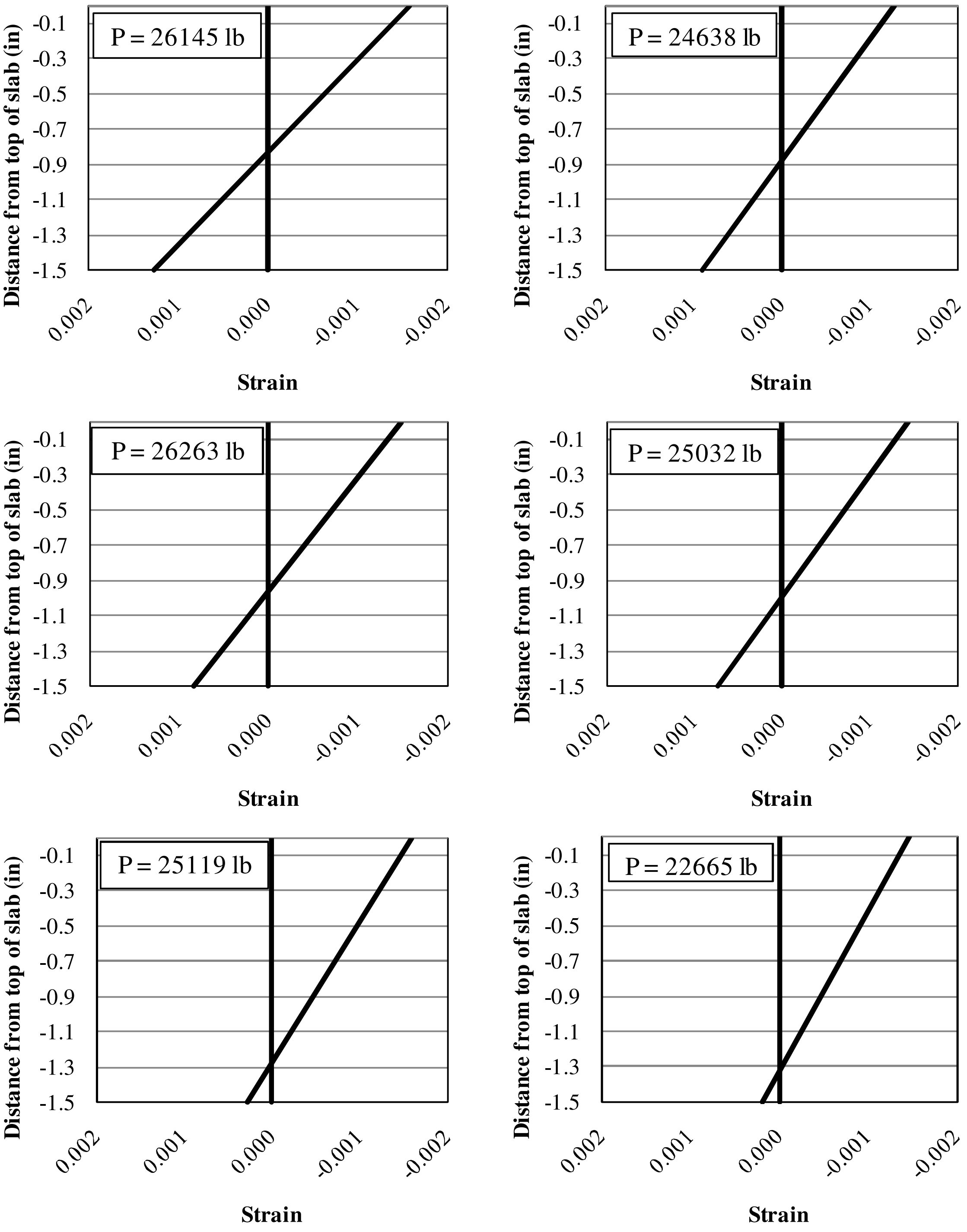

Figure 5.31: Strain distributions for the strengthened slab (3 of 4)

(1” = 25.4 mm, 1 lb = 4.45 N)

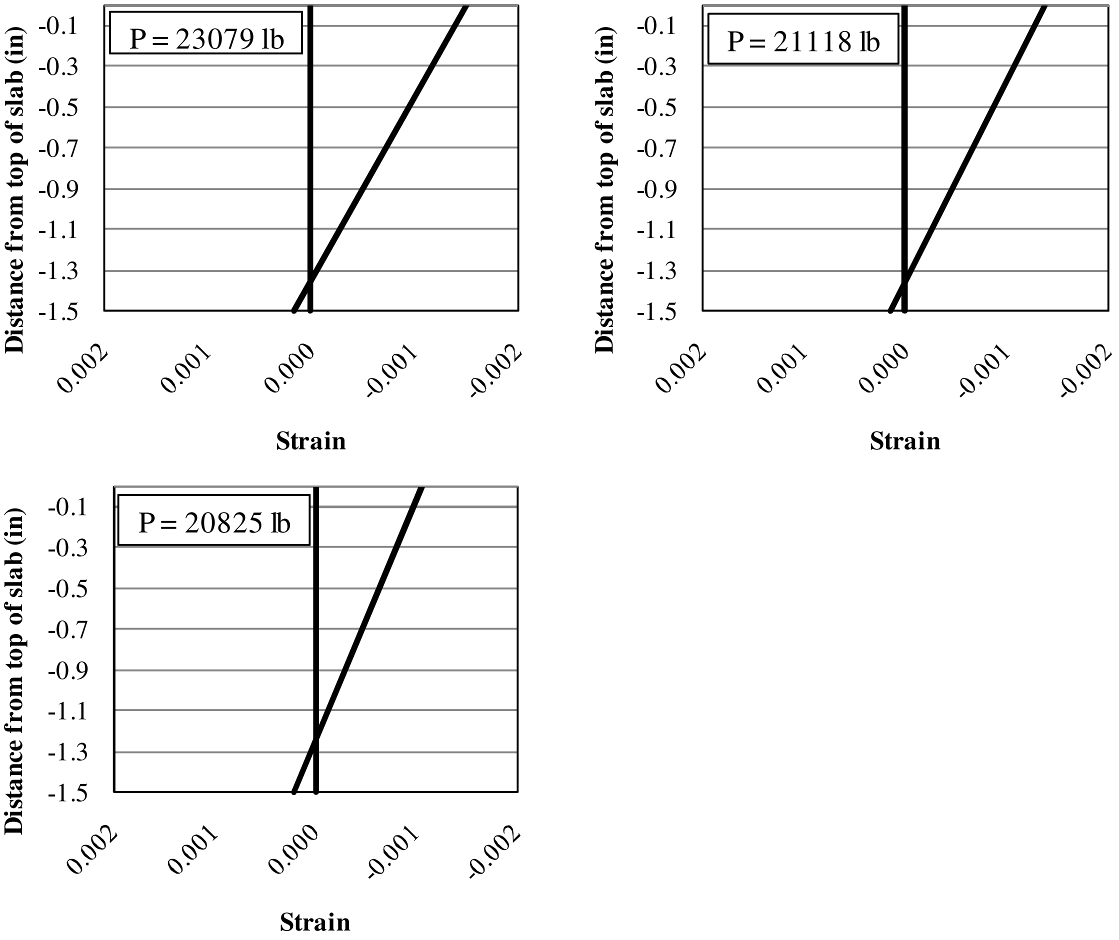

Figure 5.32: Strain distributions for the strengthened slab (4 of 4)

(1" = 25.4 mm, 1 lb = 4.45 N)

The strain gage data of the CFRP is shown Figure 5.33. It can be observed that as the load increases, the CFRP moved from being in slight compression to being fully in tension as the test progressed. This validates the main hypothesis of the suggested strengthening system. At the point when the UHPC began to debond from the NVC substrate and experience the other types of failure as depicted in Figure 5.26, the amount of tensile strain in the CFRP began to decrease. Nevertheless, the CFRP remained in tension during the remainder of the test.

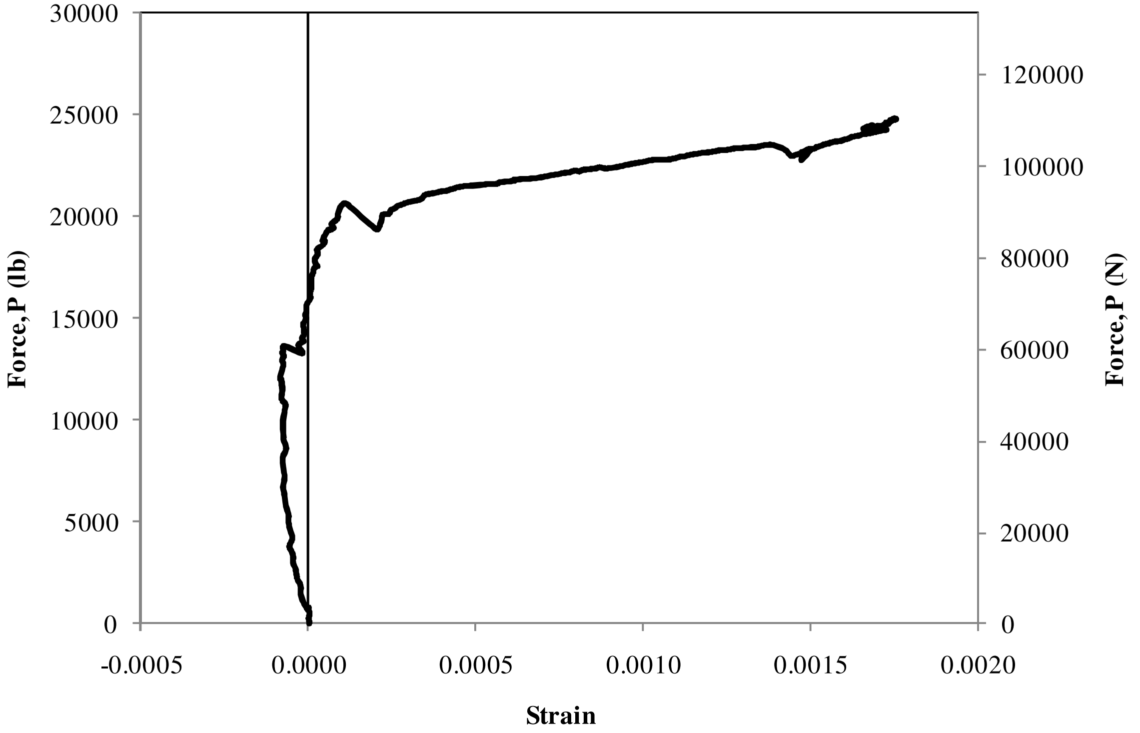

Figure 5.33: Strain gage data for the CFRP up to 24.8 kip (110.3 N)

5.2.4 MOMENT-CURVATURE OF THE STRENGTHENED SLAB

The moment curvature of the strengthened slab can be solved for using Equation 5.4 presented in Section 5.1.4. Using Equation 5.5 and Equation 5.6, I_g is found to be 823.875 in^4 (342922666 mm^4) which makes M_{cr} equal to 114075 lb·in (12889 kN·mm). The moment curvature for the strengthened slab is shown in Figure 5.34 along with the cracking moment.

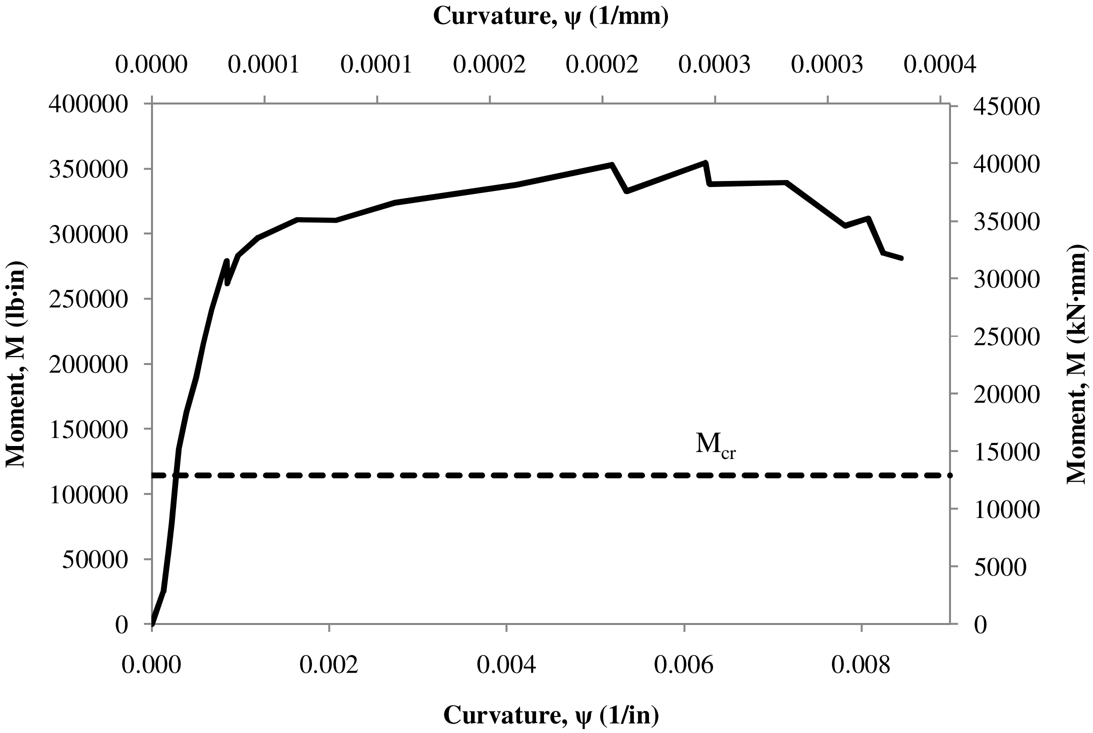

Figure 5.34: Moment-curvature of the strengthened slab

Using Equation 5.7, and using the maximum moment and the corresponding curvature, the ductility of the strengthened slab is found to be 4.3. If the maximum curvature is used with the corresponding moment, the ductility of the strengthened slab is found to be 4.7. In either case, the strengthened slab meets the criteria for classification as being ductile [49]. This is important because one of the major limitations of strengthening with CFRP is the decreased amount of ductility present due to the sudden failure present with pull-off [26].

5.3 COMPARISON

The strengthened slab showed more desirable mechanical properties than the control slab. A comparison of the properties of the two slabs is presented in Table 15. The P-Δ curves for the control slab and the strengthened slab are provided in Figure 5.35. It can be observed that the strengthened slab is stiffer in what would be considered the service loading of the structure. After the steel yields, the strengthened slab was able to take on increased loading in a similar manner to the control slab. The strengthened slab was capable of maintaining higher maximum load as well as displacing further than the control slab. The strengthened slab shows less ductility than the control slab, but is still considered ductile by CHBDC definitions [49].

Table 15: Mechanical property comparison of the control and strengthened slabs

Property	Units	Control Slab	Strengthened Slab	% Increase
Maximum Load	lb (N)	18625 (82848)	26263 (116824)	41
Maximum Displacement	in (mm)	3.65 (92.71)	4.42 (112.27)	21
Stiffness	lb/in (N/mm)	21839 (3825)	64867 (11360)	197
Toughness	kip·in (kN·mm)	51.41 (5808)	137.33 (15516)	167
Ductility	-	7.24	4.35, 4.67	(40)

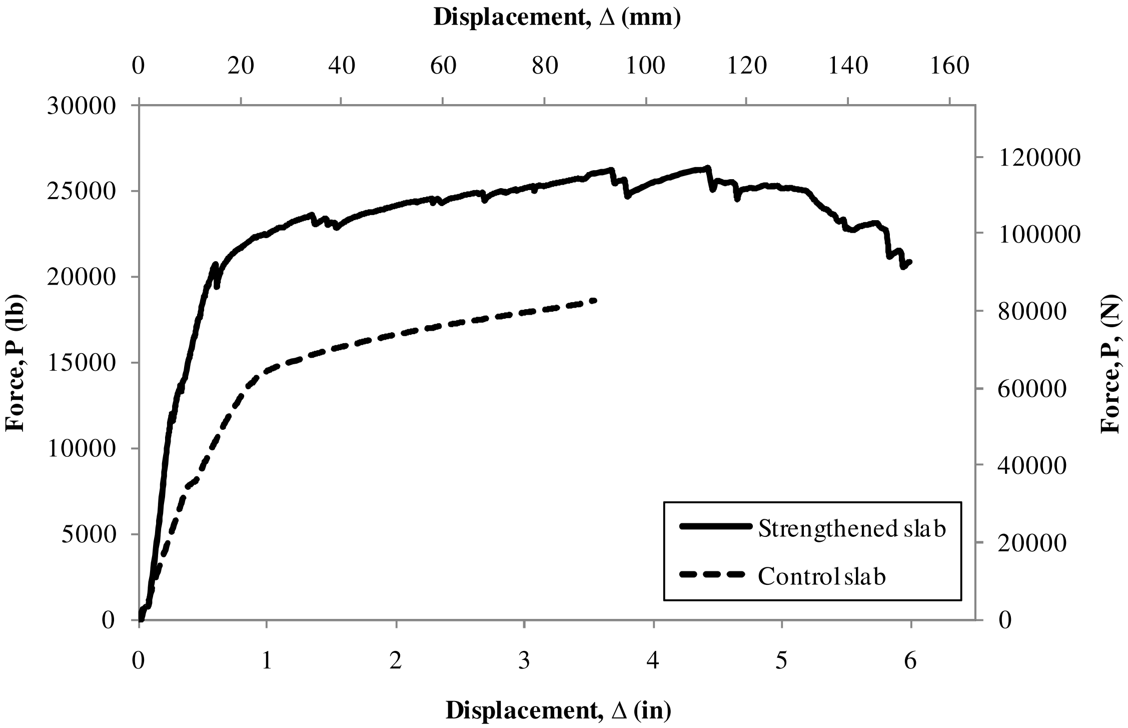

Figure 5.35: P-Δ curve comparing the control slab and the strengthened slab

The strengthened slab showed less cracking at lower loads than the control slab. Figure 5.1, which depicts the control slab, and Figure 5.13, which depicts the strengthened slab, show cracking present in the two slabs at similar loads. Figure 5.1 presents a load of 7 kips (31.1 kN) and Figure 5.13 presents a load of 10 kips (44.5 kN). It can be observed that the strengthened slab was more resilient to cracking.

The moment curvature of the control and strengthened slabs are compared in Figure 5.36. It can be observed that the curvatures for both slabs are the same until approximately 50000 lb·in (5649 kN·mm), where the strengthened slab shows a much higher flexural rigidity. The strengthened slab and control slab both change in flexural rigidity at approximately 0.001 1/in (0.00004 1/mm) where the flexural rigidity of both slabs become similar once more. The strengthened slab exhibits prolonged curvature when compared to the control slab.

Mψ is defined as the energy per unit depth. The two slabs can be compared by solving for the relatively ductility of the two slabs as given in Equation 5.8 and Equation 5.9. As in Section 5.2.4, Mψ is used for both the maximum moment and maximum curvature of the strengthened slab. The results for this comparison are observed in Table 16. In each case, the strengthened shows higher energy per unit depth. This shows that the strengthened slab is more ductile than the control slab if the same depth was maintained between the two specimens.

$$J_s = \frac{M_s \psi_{s\ \mathrm{strengthened}}}{M_s \psi_{s\ \mathrm{control}}} \tag{5.8}$$

$$J_u = \frac{M_u \psi_{u\ \mathrm{strengthened}}}{M_u \psi_{u\ \mathrm{control}}} \tag{5.9}$$

Table 16: Comparison of the relative energy per unit depth

J_s	3.3
J_u	2.1, 2.0

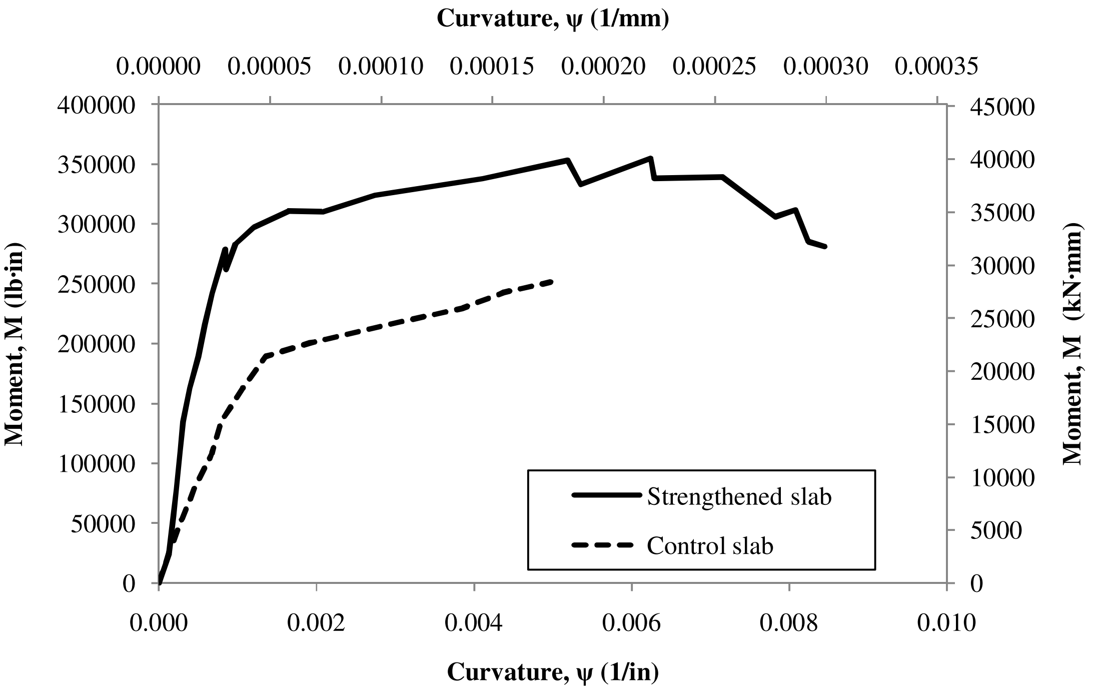

Figure 5.36: Moment-curvature comparison of the control and strengthened slabs

5.4 FINITE ELEMENT ANALYSIS

This section presents and compares the results obtained using the finite element models of the control and the strengthened slabs. In addition, the results are compared with tests that vary the geometry of the control slab and modify the material properties used in the strengthened slab.

5.4.1 CONTROL SLAB

The control slab was calibrated to the P-Δ curve acquired during testing of the control slab. The comparison between the FEA and experimental results for the P-Δ curve are presented in Figure 5.37. It can be observed that the FEA results were able to fit the experimental results fairly well. The difference in the initial stiffness in the FEA can be attributed to the lack of cracks in the model due to shrinkage [44]. Because the compressive capabilities of the FEA were not enabled, failure had to be defined in an alternative fashion. The slab was considered to have failed when the total mechanical strain in the longitudinal direction of the slab reached a value of -0.0035 across the entire width of the top of the slab. This crushing strain was chosen based on strain gage data. For the control slab, this failure occurred at 18049 lb (80286 N). This failure strain plot is shown in Figure 5.38. Without this failure criterion, the P-Δ curve of the control slab would continue to follow the experimental results. This difference in final displacement at failure can be attributed to the idealization of all of the constituents in the FE model.

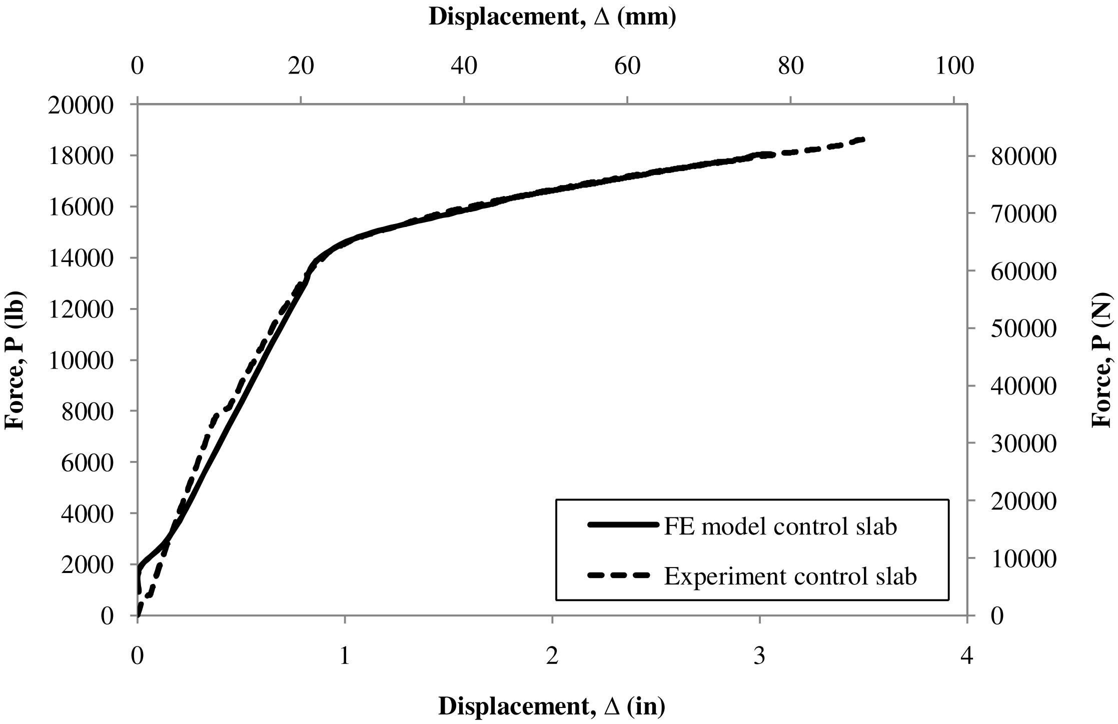

Figure 5.37: P-Δ comparison of the FEA and experimental results for the control slab

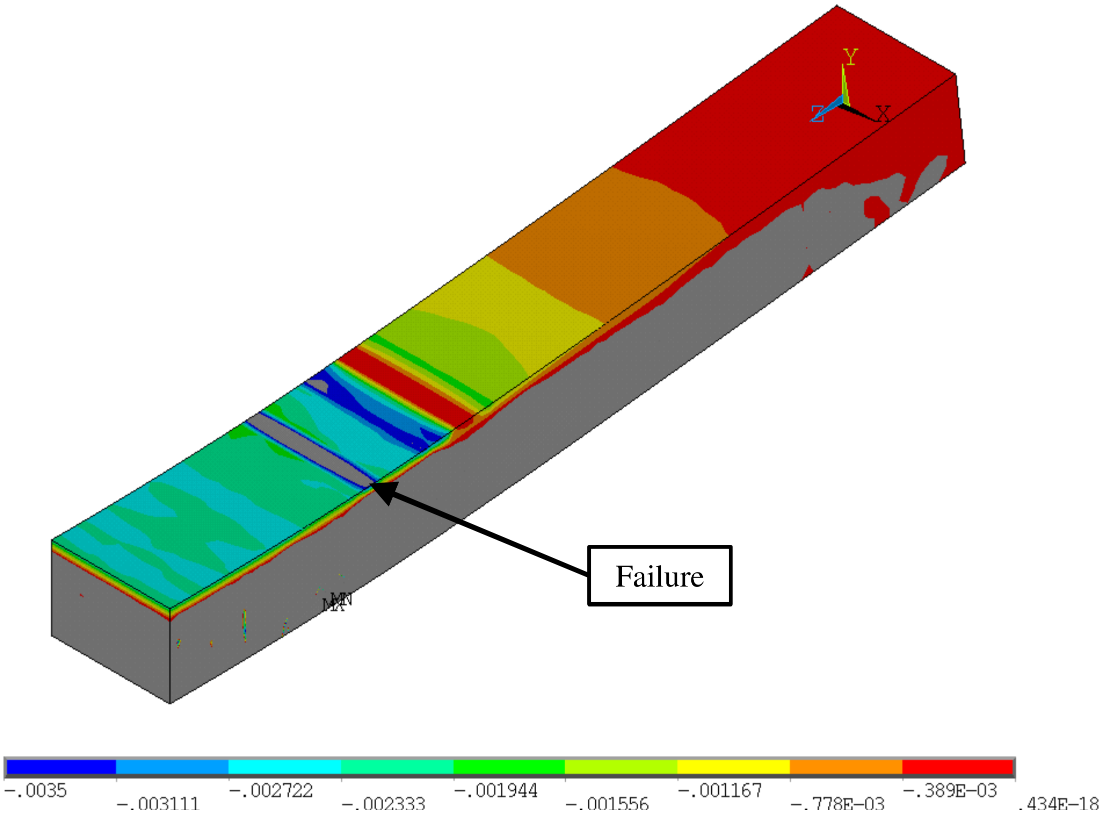

Figure 5.38: Compressive strain in the FE model in the NVC of the control slab at P = 17444 lb (77595 N)

The location of final failure is consistent with experimental results, as is shown in Figure 5.3 and Figure 5.4.

The FE model provides cracking and crushing plots for the concrete elements used in the analysis. Figure 5.39 through Figure 5.45 show the cracking of the control slab as the load increases.

The FE model predicted that the initial cracking occurs at 2784 lb (12384 N). This cracking was flexural and was isolated to the region between the rollers, as shown in

Figure 5.39. The initial cracking extends to approximately 1" below the top of the slab, which is consistent with strain gauge data.

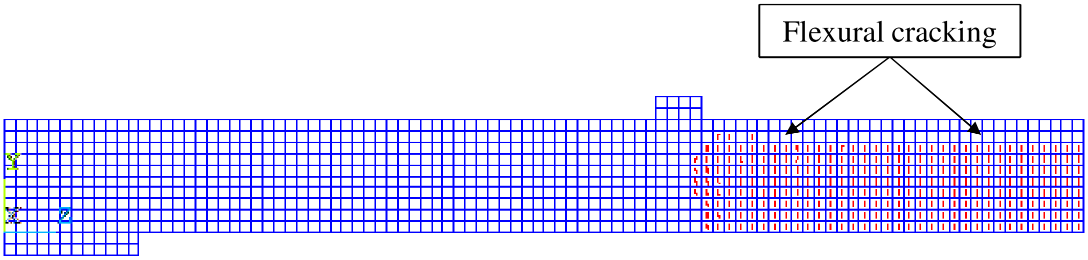

Figure 5.39: FE depiction of control slab cracking at P = 2784 lb (12384 N)

At an applied load of 5568 lb (24768 N), the flexural cracks extend to outside of the roller. In addition, flexural shear cracks that are directed towards the roller begin to appear, as is shown in Figure 5.40.

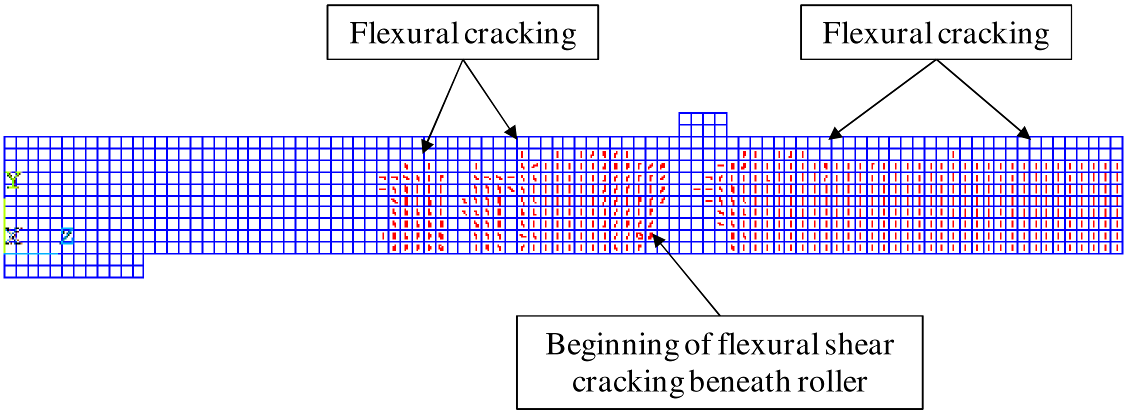

Figure 5.40: FE depiction of control slab cracking at P = 5568 lb (24768 N)

With increased loading to 10208 lb (45407 N), flexural cracking continues to appear in the slab and were transforming to flexural shear cracks near the support and outside the middle region. Horizontal cracking began to appear beneath the roller.

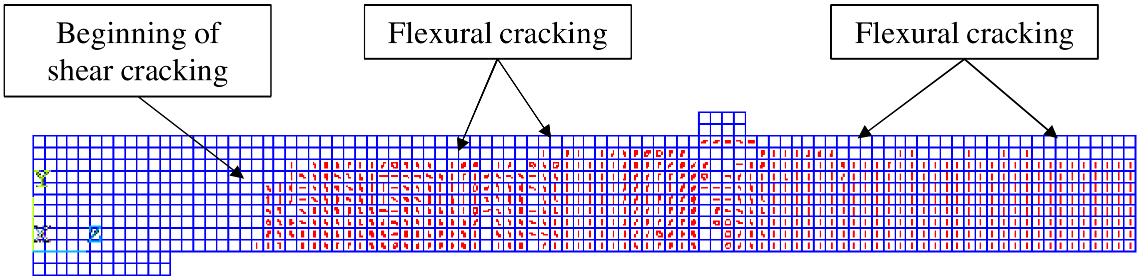

Figure 5.41: FE depiction of control slab cracking at P =10208 lb (45407 N)

The concrete plot shown in Figure 5.42 is very close to the steel yield point. It can be observed that, at this load, the neutral axis began to move closer to the top of the beam. Shear cracking was evident at this point but did not fully extend to the top of the slab. Beneath the roller, the concrete exhibited multiple types of cracking.

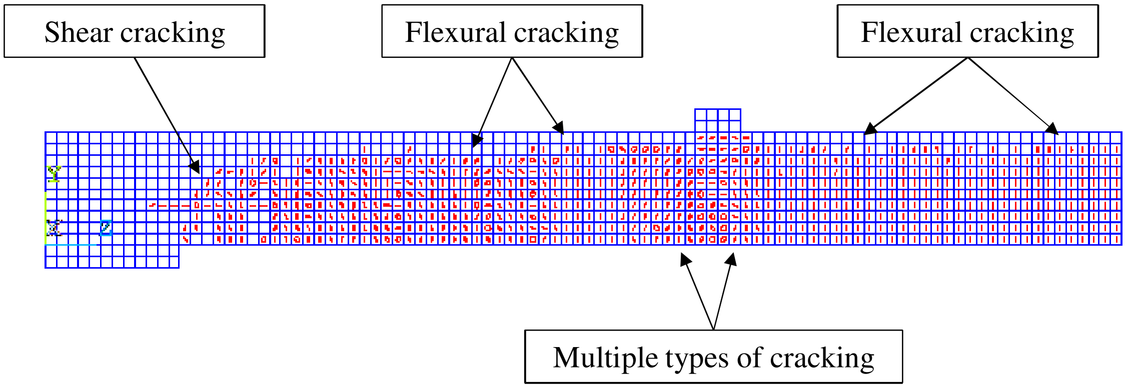

Figure 5.42: FE depiction of control slab cracking at P = 14848 lb (66047 N)

Figure 5.43 through Figure 5.45 depict FE model of the control slab as the steel yielded. Shear cracks continued to develop between the roller and the supports, though it was still not fully developed. These shear cracks appeared at the load of 16003 lb (71172 N), as can be observed in Figure 5.43 and remain relatively constant until failure.

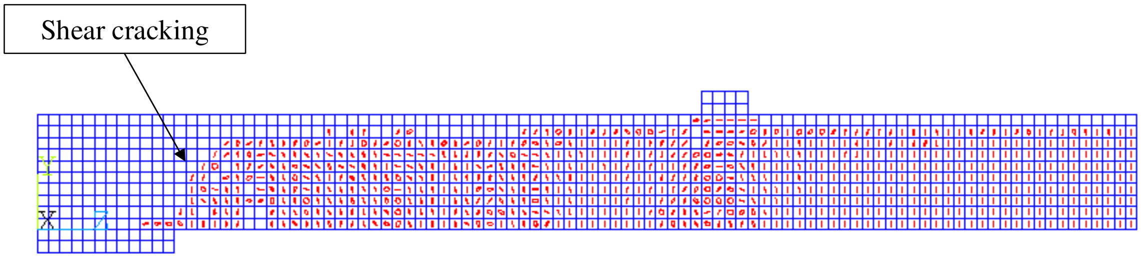

Figure 5.43: FE depiction of control slab cracking at P = 16003 lb (73396 N)

As the load increased, it can be observed that crushing on the top of the slab was very close to occurring. This near crushing continued to grow until crushing occurred at 18049 lb (80206 N). Figure 5.44 and Figure 5.45 show this extension of crushing along the top of the slab.

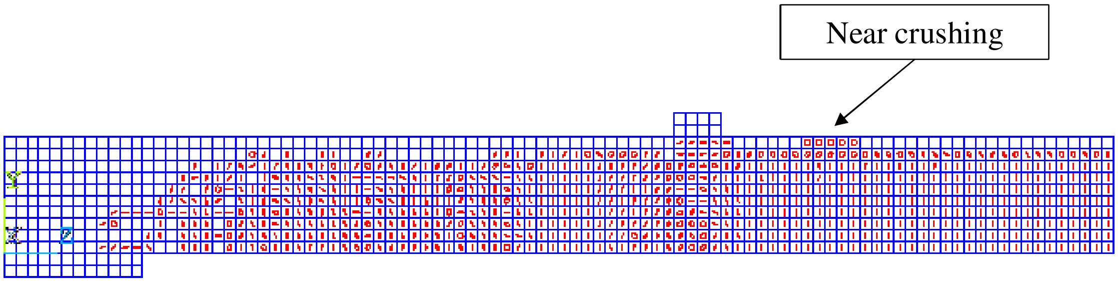

Figure 5.44: FE depiction of control slab cracking at P = 17006 lb (75646 N)

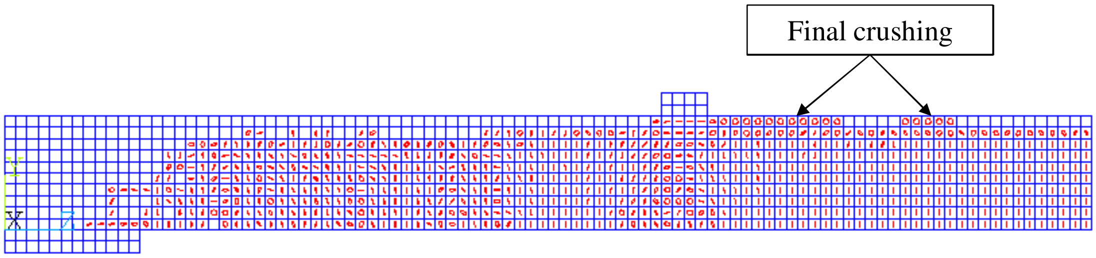

Figure 5.45: FE depiction of control slab cracking at P = 18049 lb (80206 N)

5.4.2 STRENGTHENED SLAB

The P-Δ curves of the experimental test and FE analysis are compared in Figure 5.46. The crushing strain of the UHPC was taken as 0.0041 as reported by Graybeal [10] and the ultimate tensile limits of the steel and CFRP have been taken from experimental and manufacturer data. The FE model was considered to fail if the crushing strain of the UHPC or the tensile strain limits of the steel and CFRP were surpassed. The final load applied to the strengthened slab was found to be 40841 lb (181670 N) at a displacement of 3.74" (95 mm). The strengthened slab failed in compression and its compressive strain plot is shown in Figure 5.47. The tensile strain in the CFRP is shown in Figure 5.48 and it can be observed that the CFRP is in tension, aside from the portion near the support. The maximum tensile strain did not reach the failure value reported in Table 12.

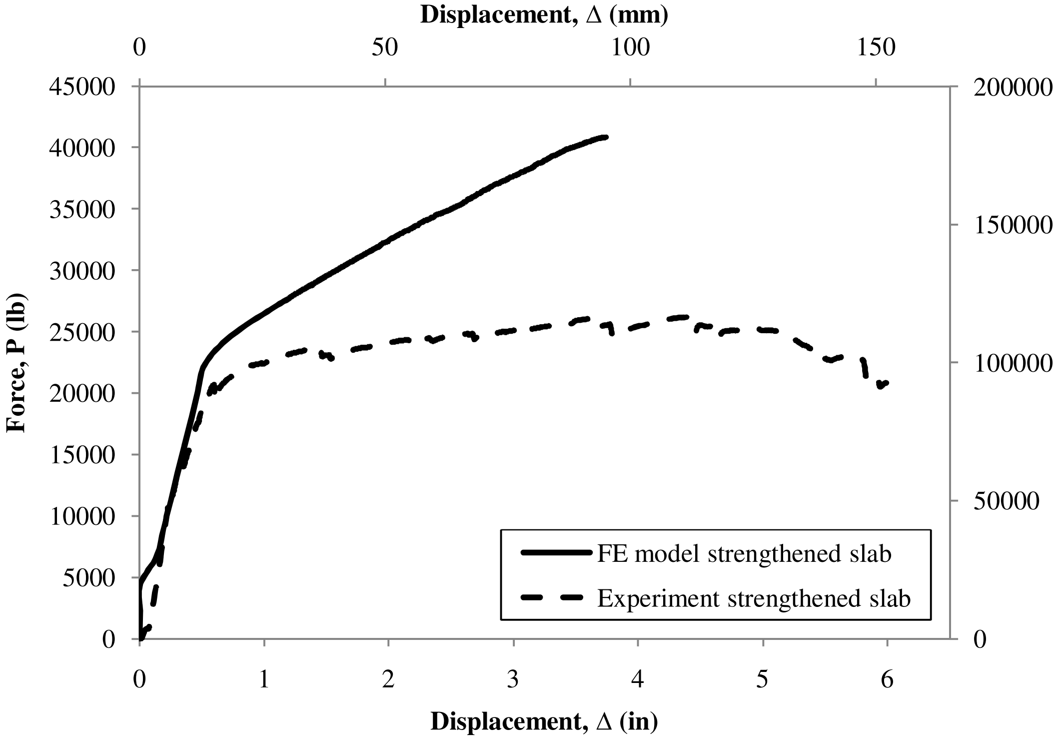

Figure 5.46: P-Δ of the FE and experimental results for the strengthened slab

The FE curve exhibited higher capacity than the experimental curve, which can be attributed to the perfect bond between all constituents used in the model. This curve shows the real capability of using this system of UHPC and CFRP. If perfect bond could be created between the different materials in the experimental setup, the P-Δ curve would follow the FE results. Debonding in the experimental strengthened slab caused the flexural capacity of the affected sections to drop to the flexural capacity of the control slab. The lower capacity in the experiment existed because the system no longer acted as a composite where debonding occurred.

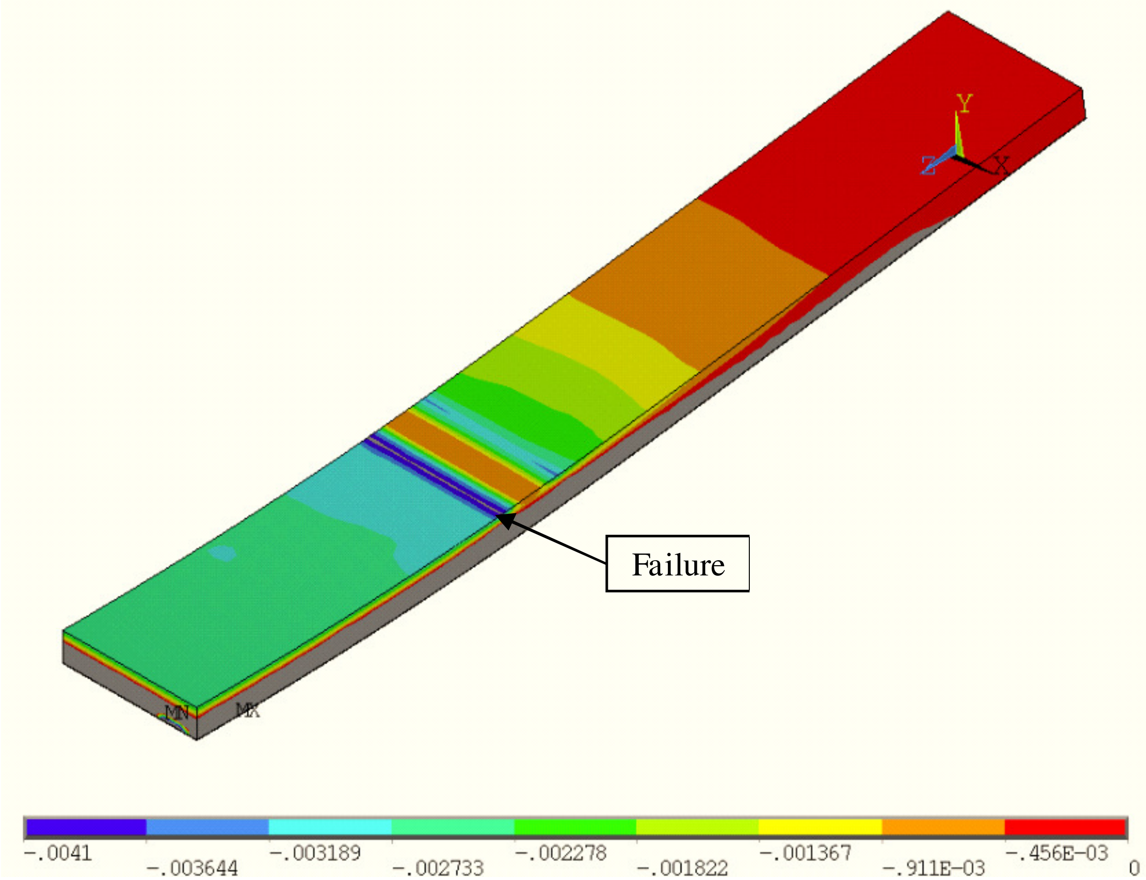

Figure 5.47: Compressive strain in the FE model in the UHPC of the strengthened slab at P = 40841 lb (181670 N)

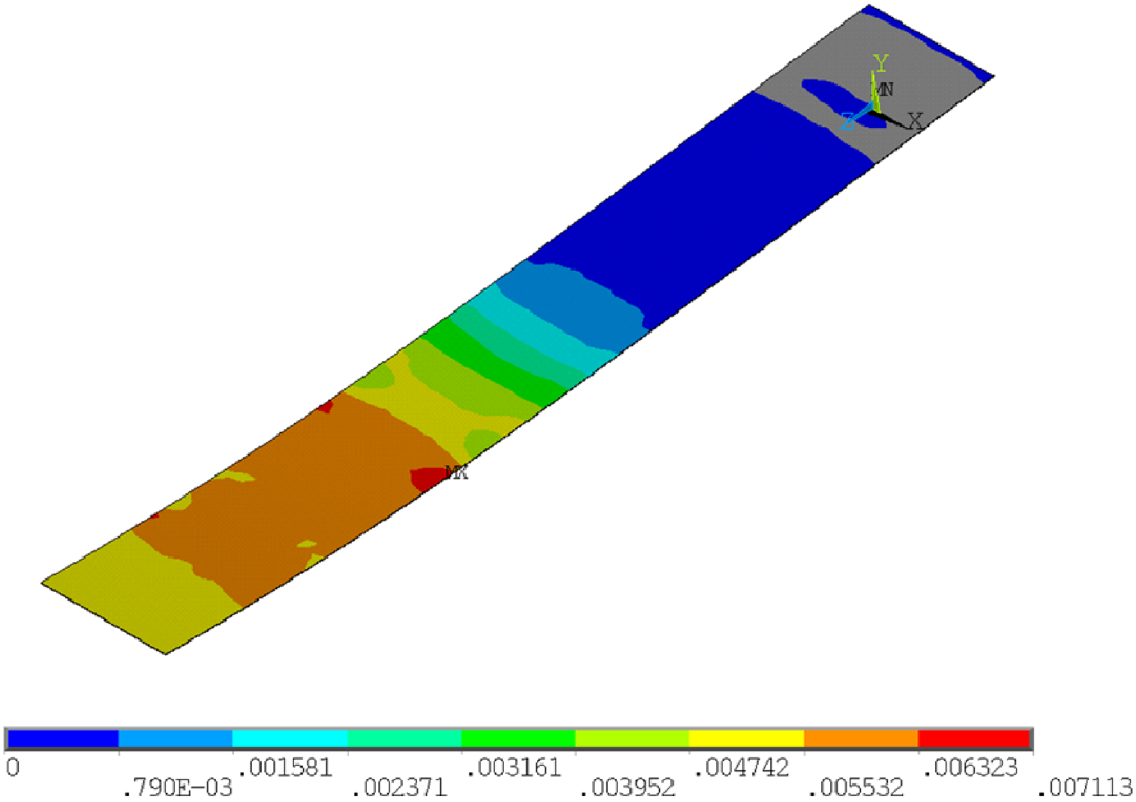

Figure 5.48: Tensile strain in the FE model in the CFRP of the strengthened slab at P = 40841 lb (181670 N)

Shear stresses across the top of the NVC substrate were the cause of debonding. Figure 5.49 shows the shear contours normalized to the maximum shear stress in the concrete defined as

Imperial: $$V_c = 2\sqrt{f'_c} \tag{5.10}$$

SI: $$V_c = \frac{\sqrt{f'_c}}{6} \tag{5.11}$$

It can be observed that the region of high shear exists with between the roller and the support, as was expected. This region is where the CFRP and UHPC overlay debonding occurred in the experiment.

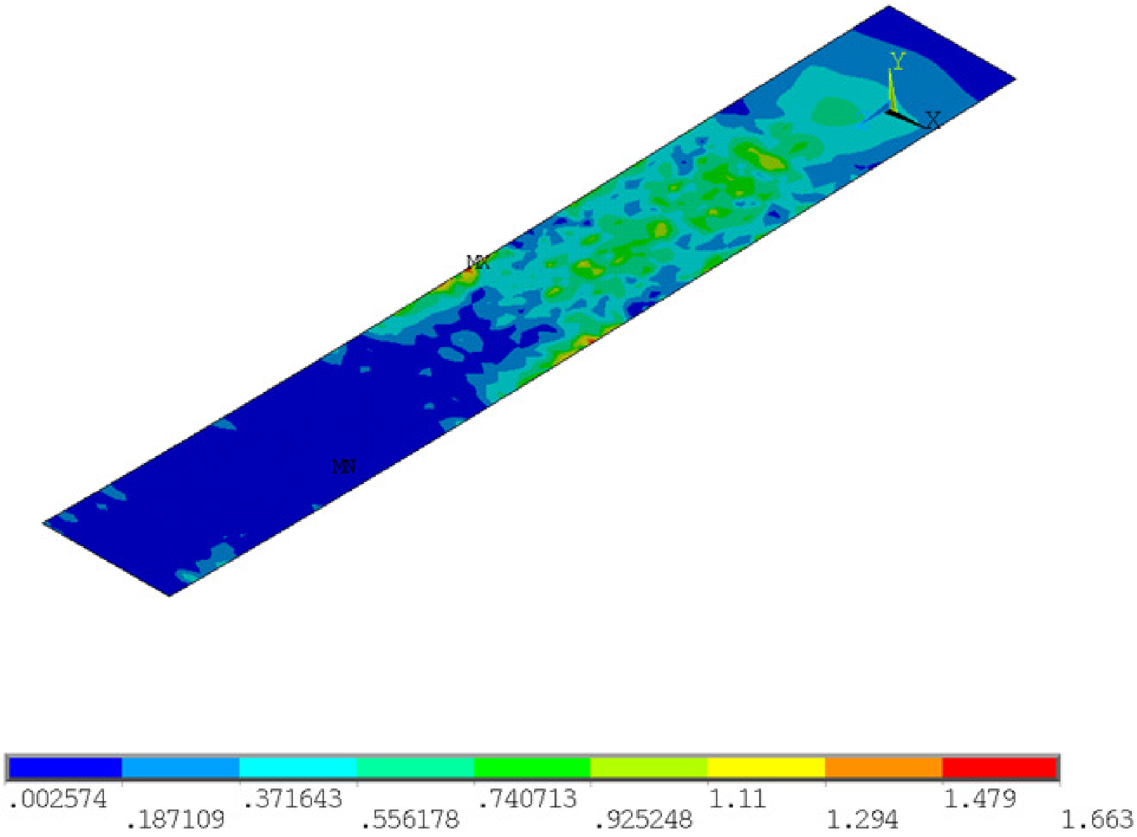

Figure 5.49: Normalized shear contours on top of the NVC substrate at P = 26880 lb (119568 N)

To accurately model the strengthened slab, debonding must be considered. The complexities in modeling the bond between the UHPC and CFRP as well as the bond between the CFRP and NVC substrate include work that is outside of the scope of this thesis. In order to create an FE model that accounts for this failure, cohesive zone elements must be used. It is recommended that interface elements with normal and shear traction capabilities be included. The shear stress interaction between the different materials will be able to account for debonding present in the experimental strengthened slab.

5.4.3 ALTERNATIVE MODELS

The first alternative model was a variation of the control slab with increased depth. The model was found to fail due to compression at a load of 27677 lb (123113 N) and a corresponding displacement of 2.0” (51.1 mm). The failure occurred at a different location than the original control model. The failure occurred right next to the roller as shown Figure 5.50, which is consistent with the failure of the FE model of the strengthened slab as shown in Figure 5.47. The P-Δ curve for this FEA is compared to the analytical P-Δ curve of the control slab in Figure 5.51. It can be observed that the change in load and stiffness are greatly increased over the control slab. These features can be directly attributed to the 50% increase in d used in Equation 3.8.

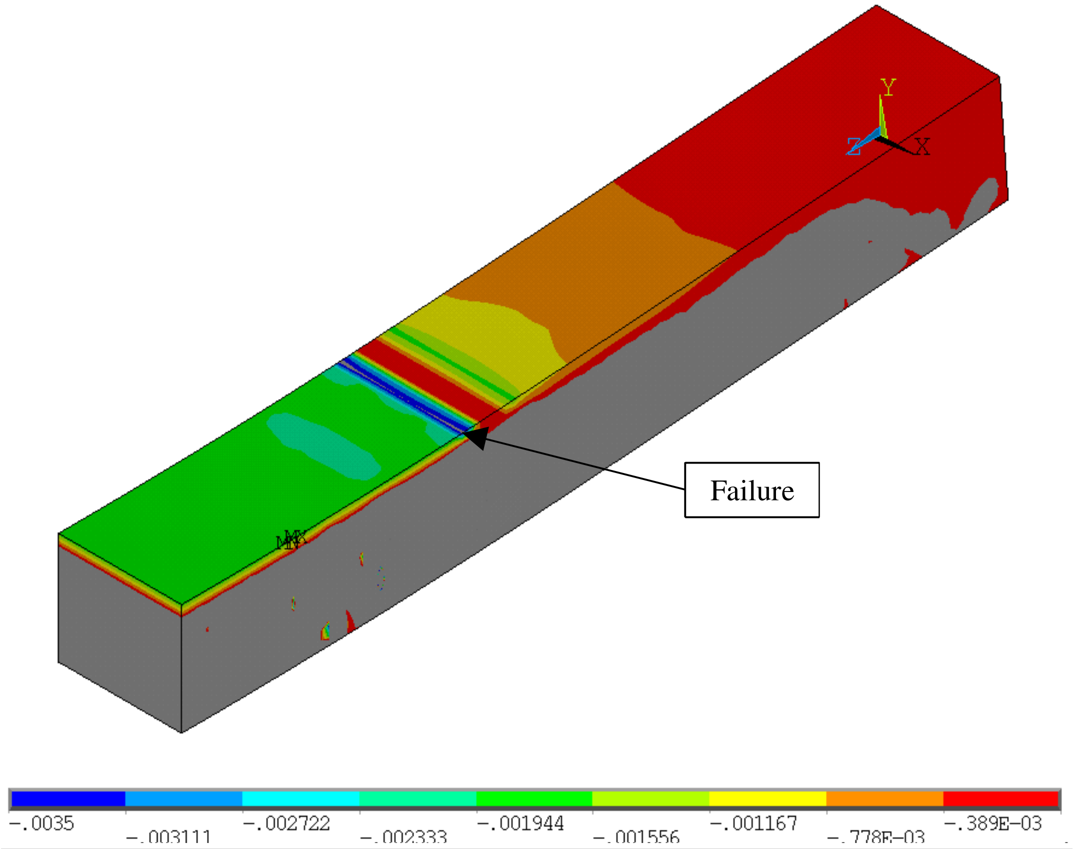

Figure 5.50: Compressive strain in the FE model of the control slab with increased depth at P = 27677 lb (123113 N)

The increased stiffness can be found by analyzing Equation 5.2. Δ for the four point bending test with the loading geometry can be defined as

$$\Delta = \frac{12028.5P}{EI} \tag{5.12}$$

substituting Equation 5.x into Equation 5.2 results in

$$k = \frac{EI}{12028.5} \tag{5.13}$$

Assuming the elastic modulus is near constant between the FE model control slab and the FE model control slab (6.5”, 165.1 mm), the stiffness is dependent on the moment of inertia. I_g for the control slab was found to be 375 in^4 (156086785 mm^4) in Section 5.1.4. Using Equation 5.6, I_g for the control slab (6.5”, 165.1 mm) is found to be 823.875 in^4 (342922.666 mm^4), or approximately 2.2 times greater than the original control slab.

The reduced deflection is also caused by the increased depth, as the reinforcing steel yielded at a lower displacement due to the increased stiffness. Because the strain hardening in the steel began at a lower deflection, the equilibrium causing compressive strain failure in the NVC occurred at a lower displacement.

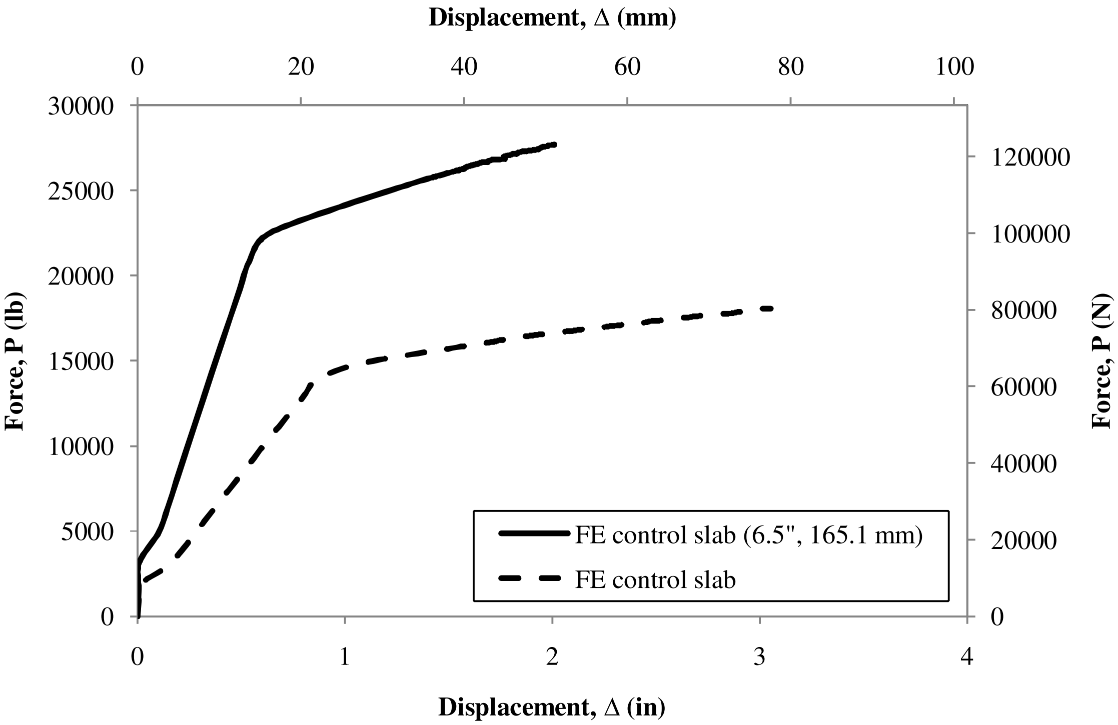

Figure 5.51: P-Δ of the alternative model with increased depth

The P-Δ curves of the FE model of control slab (6.5”, 165.1 mm) and FE model of the strengthened slab are compared in Figure 5.52. It can be observed that even with the same depth, the NVC slab is unable to match the capacity and displacement of the strengthened slab.

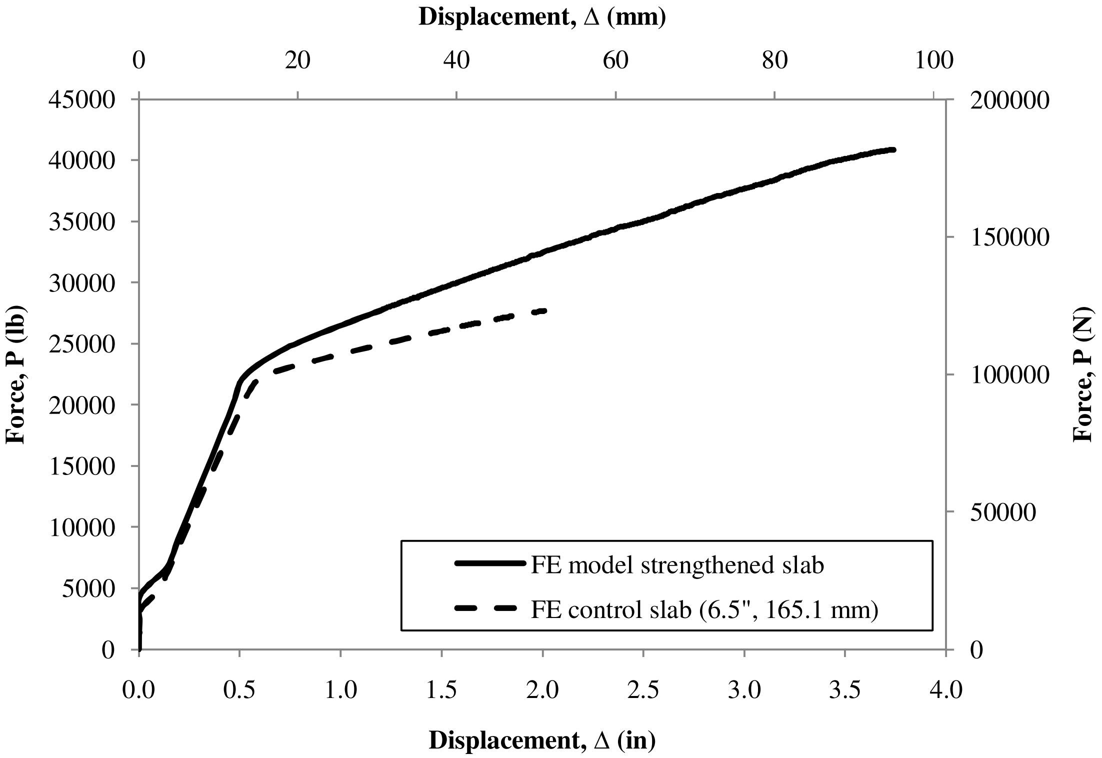

Figure 5.52: P-Δ comparison of the 6.5” (165.1 mm) NVC slab and strengthened slab

The parametric study was performed by replacing the UHPC with two different strengths of NVC. The UHPC was first replaced with the NVC used in the control slab with a characteristic compressive strength of 6750 psi (47 MPa). The second alternative model used HPC with a characteristic compressive strength of 14500 psi (100 MPa). The P-Δ curves for these models are compared with the P-Δ curve of the strengthened slab FE model in Figure 5.55. Using Equation 3.17 to Equation 3.19 and the assumptions used in Section 3.2.1, the maximum load expected using the 6750 psi (47 MPa) overlay was found to be 19.2 kip (85.6 kN) with a depth to the neutral axis of 1.1” (28.6 mm) and the maximum load expected using the 14500 psi (100 MPa) overlay was found to be 22.8 kip (101.5 kN) with a depth to the neutral axis of 0.83” (20.3 mm). In each case, the neutral axis was found to rise into the concrete overlay.

The failure in the two alternative models occurs in the constant moment region between the rollers. The failure in the FE model of the slab strengthened with 6750 psi (47 MPa) NVC is shown in Figure 5.53. This failure location is consistent with the FE model of the strengthened slab and the FE model of the control slab (6.5”, 165.1 mm). The failure in the slab strengthened with HPC occurred at the same location, as shown in Figure 5.54

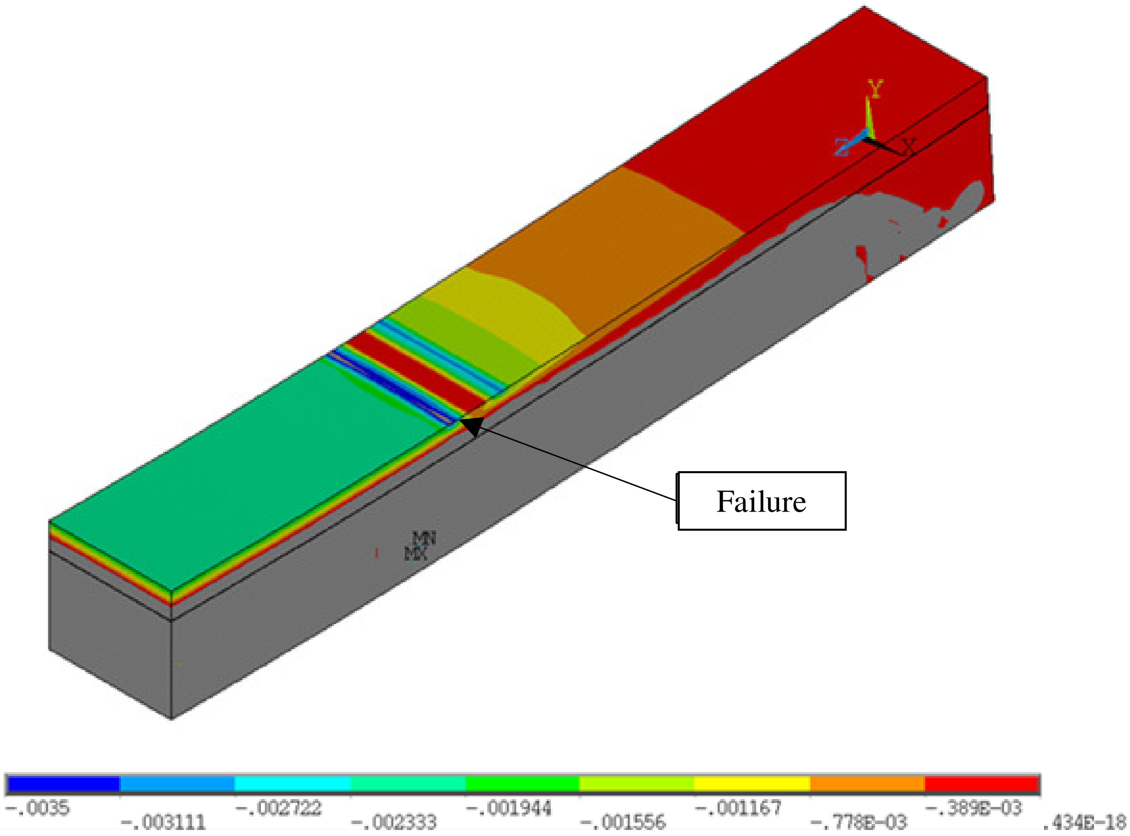

Figure 5.53: Compressive strain in the FE model of the 6750 psi (47 MPa) NVC in the strengthened slab

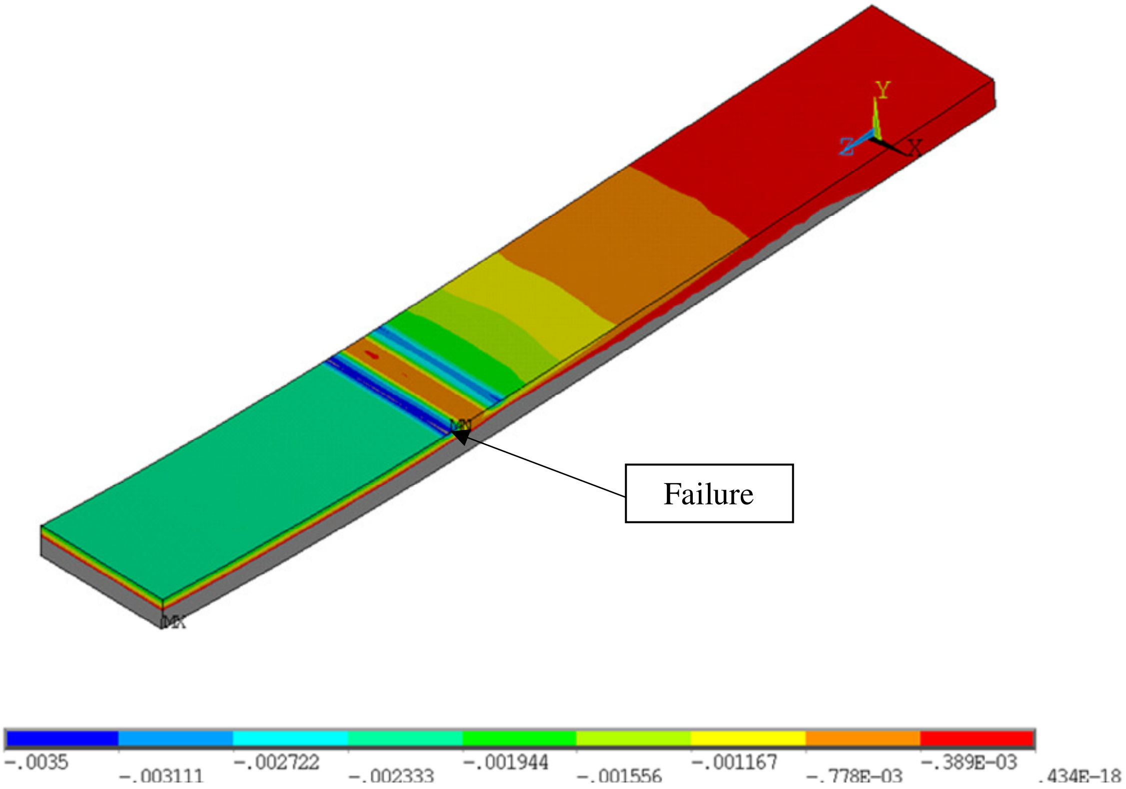

Figure 5.54: Compressive strain in the FE model of the 14500 psi (100 MPa) HPC in the strengthened slab

It can be observed that the FE model of the strengthened slab using an NVC overlay with a characteristic compressive strength of 6750 psi (47 MPa) featured lower flexural capacity and displacement than the alternative model that featured an NVC overlay with a characteristic compressive strength of 14500 psi (100 MPa). Both alternative models had less displacement at failure than the FE model of the strengthened slab.

The P-Δ curves of the FE model of the strengthened slab and the FE model of the strengthened slab with the 14500 psi (100 MPa) overlay are very similar. This is because of their high characteristic compressive strengths and the shape of the stress strain curves that each exhibit in flexure. The lower displacement and force from using the 14500 psi (100 MPa) NVC overlay is caused by the lower compressive strain capacity of the NVC in comparison to UHPC.

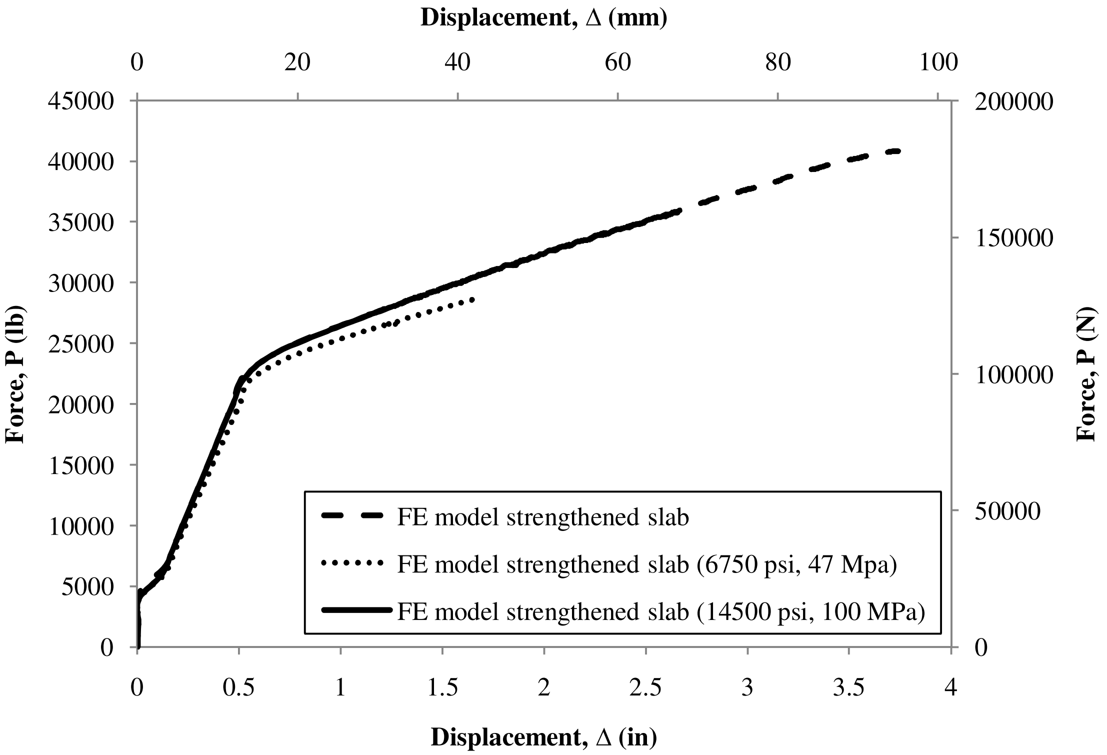

Figure 5.55: P-Δ curves for the FE model of the strengthened slab using different strengths of concrete overlays

CHAPTER 6 CONCLUSIONS AND RECOMMENDATIONS

The combination of UHPC and CFRP applied to the compressive side of an RC slab has been shown to be an effective method of strengthening. By using the compressive side of the slab, installation problems typically associated with strengthening were avoided. Installing a system on the top of a structural slab will allow for more control and consistency than installation on the underside. In practice, the UHPC would protect the CFRP from weathering and degradation and other environmental durability issues such as water and chloride permeation. UPHC also features high wear resistance due to its high compressive strength.

The experimental investigation proved the hypothesis that the UHPC would absorb all compressive stresses exerted onto the slab and the CFRP would act in tension during the ultimate limit state. In doing so, the maximum load, maximum displacement, stiffness, toughness, and relative ductility were all increased. It is apparent that this system can be used to strengthen existing RC slabs given a good bond mechanism is employed. However, the hypothesis of perfect bond between UHPC, FRP, and the existing concrete slab does not hold. Unless special bonding agents or methods are used, debonding will govern the capacity.

It was shown through experimental and FE modeling that the limited capacity of the strengthened slab was governed by debonding of the UHPC and CFRP to the NVC substrate at the locations of high shear stress. Through the experimental methods, it was also shown that having many different types of failure increased the toughness of the system substantially. The combination of UHPC and FRP created alternative load paths that allowed the strengthened slab to continue to act as a composite throughout the test and it was shown that this method did not result in brittle failure. The ductility of the proposed strengthening system is evident.

One area of interest is the theoretical capacity of a perfectly bonded strengthening system. If debonding were to not occur, the strengthened slab would have exhibited higher ultimate load capacity as well as strain at failure. Better bond between the UHPC-FRP system and the NVC substrate can possibly be achieved using precast elements where the interfaces can be further controlled using adhesives. Other options include using high performance concrete anchors or a high performance polymer concrete (PC).

The FE parametric study of different types of overlays showed that UHPC is the material of choice for strengthening with this system. This is because of the high compressive strengths and strains that the UHPC exhibits at failure. For this reason and because of the high bond capabilities, PC may be an acceptable material to use in this strengthening system.

The proposed system can be extrapolated to other structures and applications. In bridges, the same method can be employed. The surface of an existing bridge deck can be removed and prepared for bonding FRP composites and shear-reinforcing anchors can be installed. The UHPC can then be cast as a simple overlay that tapers to the normal substrate towards the abutments. Another option is to remove a portion of the deck and replace the created void with this strengthening system. In doing so, the UHPC overlay would be constrained in the longitudinal direction, which may eliminate the horizontal shear failure observed in the experimental tests. It has been shown through experimental and FE analysis that this system is effective without having to increase the depth of a structure.

The proposed system can also be extended to strengthen structures against blast and impact. The debonding that occurred can be seen as a positive feature in this application because it enabled enhanced ductility. It was apparent that the overlay was sacrificed before any significant damage occurred to the substrate. This system can thus be used on the outside of a structure as a protective system. Once damaged, the strengthening system can be replaced. In doing so, the use of precast UHPC panels can be attractive from the constructability point of view.

6.1 FUTURE WORK

To further investigate the capabilities of this system, more research is needed. It is recommended that the use of precast elements that make use of adhesives and anchors capable of carrying high shear be used.. This system's features may be easier to control, as adhesive is suggested to be applied between all elements.

Another area that should be investigated is that of blast and impact resistance of the system. Using FE modeling optimization, it is possible to design the most favorable combination of material characteristics and geometries. This investigation would show further implementations of this system.

CHAPTER 7 REFERENCES

1. U.S. Geological Survey, *Mineral Commodity Summaries 2011: U.S. Geological Survey*. 2011. p. 38-39.

2. Arduini, M., Nanni, A., Romagnolo, M., *Performance of One-Way Reinforced Concrete Slabs with Externally Bonded Fiber-Reinforced Polymer Strengthening.* ACI Structural Journal, 2004. **101**(2): p. 193-201.

3. Breña, S.F. and Steves, M.A., *Increasing the Flexural Capacity of an Existing Reinforced Concrete Bridge in Texas Using CFRP Composites*, in *ACI Fall 2003 Convention*. 2003, American Concrete Institute: Boston, Massachusetts.

4. Hutchinson, R., Tadros, G., Kroman, J., and Rizkalla, S., *Use of Externally Bonded FRP Systems for Rehabilitation of Bridges in Western Canada*, in *ACI Fall 2003 Convention*, S. Rizkalla and A. Nanni, Editors. 2003, American Concrete Institute: Boston, Massachusetts. p. 239-248.

5. Basler, M., White, D., and Desroches, M., *Bridge Strengthening with Advanced Composite Systems*, in *ACI Fall 2003 Convention*, S. Rizkalla and A. Nanni, Editors. 2003, American Concrete Institute: Boston, Massachusetts. p. 263-278.

6. Parretti, R., Nanni, A., Cox, J., Jones, C., and Mayo, R., *Flexural Strengthening of Impacted PC Girder with FRP Composites*, in *ACI Fall 2003 Convention*, S. Rizkalla and A. Nanni, Editors. 2003, American Concrete Institute: Boston, Massachusetts. p. 249-262.

7. Portland Cement Association. *What is Ultra High Performance Concrete?* 2011 [cited 2011 03/26/2011]; Available from: http://www.cement.org /bridges/br_UHPC.asp.

8. Schmidt, M. and Fehling, E., *Ultra-High-Performance Concrete: Research, Development and Application in Europe*, in *Seventh International Symposium on the Utilization of High-Strength/High-Performance Concrete*. 2004, ACI: Washington, D.C. p. 51-78.

9. Acker, P., *Why Does Ultrahigh-Performance Concrete (UHPC) Exhibit Such Low Shrinkage and Such Low Creep?*, in *SP-220: Autogenous Deformation of Concrete*, O.M. Jenson, D.P. Bentz, and P. Lura, Editors. 2004, American Concrete Institute.

10. Graybeal, B.A., *Characterization of the Behavior of Ultra-High Performance Concrete*, in *Civil and Environmental Engineering*. 2005, University of Maryland, College Park: College Park. p. 360.

11. Graybeal, B.A., United States. Federal Highway Administration. Office of Infrastructure Research and Development., Turner-Fairbank Highway Research Center., and Performance Systems International (Reston Va.), *Material property characterization of ultra-high performance concrete*. 2006, Federal Highway Administration, Office of Research, Development and Technology: McLean, Va.

12. Reda, M.M., Shrive, N.G., and Gillott, J.E., *Microstructural investigation of innovative UHPC.* Cement and Concrete Research, 1999. **29**(3): p. 323-329.

13. Bhanja, S. and Sengupta, B., *Optimum Silica Fume Content and Its Mode of Action on Concrete.* ACI Materials Journal, 2003. **100**(5): p. 407-412.

14. Plank, J., Schröfl, C., and Gruber, M., *Use of Supplemental Agent to Improve Flowability of Ultra-High-Performance Concrete*, in *ACI International Conference on Superplasticizers and Other Chemical Admixtures*. 2009, American Concrete Institute: Seville, Spain.

15. Shrive, N.G., *Compression testing and cracking of plain concrete.* Magazine of Concrete Research, 1983. **35**(122): p. 13.

16. Markeset, G., *Ultra High Performance Concrete is Ideal for Protective Structures.* ACI Materials Journal, 2002. **207**(8): p. 125-138.

17. Hsu, T.T.C., Slate, F.O., Sturman, G.M., and Winter, G., *Microcracking of Plain Concrete and the Shape of the Stress-Strain Curve.* Journal of the American Concrete Institute, 1963. **60**(2): p. 16.

18. Bornemann, R. and Schmidt, M., *Ultra High Performance Concrete (UHPC) - mix design and application.* Betonwerk und Fertigteil-Technik/Concrete Precasting Plant and Technology, 2002. **68**(2): p. 10-12.

19. Williams, E.M., Graham, S.S., Akers, S.A., Reed, P.A., and Rushing, T.S., *Mechanical properties of a baseline UHPC with and without steel fibers*, in *Computational Methods and Experiments in Materials Characterisation IV*, A.A. Mammoli and C.A. Brebbia, Editors. 2009. p. 93-104.

20. Graybeal, B.A., *Compressive Behavior of Ultra-High-Performance Fiber-Reinforced Concrete.* ACI Materials Journal, 2007. **104**(2): p. 146-152.

21. Schieβl, P., Mazanec, O., and Lowke, D., *SCC and UHPC - Effect of Mixing Technology on Fresh Concrete Properties*, in *Advances in Construction Materials 2007*, C.U. Grosse, Editor. 2007, Springer Berlin Heidelberg. p. 513-522.

22. ACI Committee 318, *Building Code Requirements for Structural Concrete (ACI 318-08) and Commentary (318R-08)*. 2005, American Concrete Institute: Farmington Hills, Michigan. p. 430.

23. Ricciotti, R., *The Footbridge of Peace*. 2001, Seoul: Editions Jean-Michel Place.

24. Bierwagen, B.M.a.D. *Ultra High Performance Concrete Highway Bridge*. in *2005 Mid-Continent Transportation Research Symposium*. 2006. Ames, Iowa: Iowa State University.

25. Parsekian, G.A., Brown, N.G.S.T.G., Kroman, J., Perry, P.J.S.V.H., and Boucher, A., *Tailor Made Concrete Structures*, ed. W. Stoelhorst. 2008, London: Taylor & Francis Group.

26. ACI Committee 440, *Guide for the Design and Construction of Externally Bonded FRP Systems for Strengthening Concrete Structures*. 2002, American Concrete Institute. p. 45.

27. Rüsch, H., *Researchers Toward a General Flexural Theory for Structural Concrete.* Comite Europeen du Beton, 1960. **57**(1): p. 1-28.

28. Mahfouz, I. and Rizk, T., *Field Applications of FRP Strengthening in Egypt*, in *ACI Fall 2003 Convention*, S. Rizkalla and A. Nanni, Editors. 2003, American Concrete Institute: Boston, Massachusetts. p. 279-290.

29. American Concrete Institute, *ACI 318-08: Building Code Requirements for Structural Concrete and Commentary*. 2008, American Concrete Institute. p. 456.

30. Todeschini, C.E., Bianchini, A.C., and Kesler, C.E., *Behavior of Concrete Columns Reinforced with High Strength Steels.* ACI Journal, Proceedings, 1964. **61**(6): p. 16.

31. Malvar, L.J. and Lenke, L.R., *Efficiency of Fly Ash in Mitigating Alkali-Silica Reaction Based on Chemical Composition.* ACI Materials Journal, 2006. **103**(5): p. 319-326.

32. ASTM International, *ASTM C39 / C39M - 10 Standard Test Method for Compressive Strength of Cylindrical Concrete Specimens*. 2010, ASTM International: West Conshohocken, PA. p. 7.

33. ASTM International, *ASTM C496 / C496M - 04e1 Standard Test Method for Splitting Tensile Strength of Cylindrical Concrete Specimens*. 2004, ASTM International: West Conshohocken, PA. p. 5.

34. Vishay Precision Group, *Instruction Bulletin B-129-8*, in *Surface Preparation for Strain Gage Bonding*. 2010, Micro-Measurements. p. 7.

35. Vishay Precision Group, *Application Note TT-611*, in *Strain Gage Installation for Concrete Structures*. 2010, Micro-Measurements. p. 4.

36. Vishay Micro-Measurements, *Tech Note TN-502*, in *Optimizing Strain Gage Excitation Levels*. 2005, Vishay Micro-Measurements. p. 8.

37. ASTM International, *ASTM C469 / C469M - 10 Standard Test Method for Static Modulus of Elasticity and Poisson's Ratio of Concrete in Compression*. 2010, ASTM International: West Conshohocken, PA. p. 5.

38. ASTM International, *ASTM E8 / E8M - 09 Standard Test Methods for Tension Testing of Metallic Materials*. 2009, ASTM International: West Conshohocken, PA. p. 27.

39. ANSYS Inc., *ANSYS*. 2009: Canonsburg.

40. Wolanski, A.J., *Flexural Behavior of Reinforced and Prestressed Concrete Beams Using Finite Element Analysis*. 2004, Marquette University: Milwaukee. p. 87.

41. Bangash, M.Y.H., *Concrete and Concrete Structures: Numerical Modeling and Applications*. 1989, Elsevier Science Publishers Ltd.: London.

42. Huyse, L., Hemmaty, Y., and Vandewalle, L. *Finite Element Modeling of Fiber Reinforced Concrete Beams*. in *ANSYS Conference*. 1994. Pittsburgh, Pennsylvania.

43. Zhang, Q., *Finite Element Application to Slab-column Connections Reinforced with Glass Fibre-Reinforced Polymers*. 2004, Memorial University of Newfoundland. p. 52.

44. Kachlakev, D.I., Miller, T., Yim, S., Chansawat, K., and Potisuk, T., *Finite Element Modeling of Reinforced Concrete Structures Strengthened With FRP Laminates*. 2001, Oregon Department of Transportation.

45. Hemmaty, Y. *Modelling of the Shear Force Transferred Between Cracks in Reinforced and Fibre Reinforced Concrete Structures*. in *ANSYS Conference*. 1998. Pittsburgh, Pennsylvania.

46. William, K.J. and Wanke, E.D. *Constitutive Model for the Triaxial Behavior of Concrete*. in *International Association for Bridge and Structural Engineering*. 1975. Bergamo, Italy: ISMES.

47. Choi, B.S., Oh, B.H., and Scanlon, A., *Probabilistic assessment of ACI 318 minimum thickness requirements for one-way members.* Aci Structural Journal, 2002. **99**(3): p. 344-351.

48. Chen, J.F. and Teng, J.G., *Anchorage strength models for FRP and steel plates bonded to concrete.* Journal of Structural Engineering, 2001. **127**(7): p. 784-791.

49. Canadian Standards Association, *CAN/CSA-S6-06 - Canadian Highway Bridge Design Code (CHBDC)*. 2006: CAN/CSA. 800.